

A Framework for Quantification and Physical Modeling of Cell Mixing Applied to Oscillator Synchronization in Vertebrate Somitogenesis

Koichiro Uriu^{1,2*}, Rajasekaran Bhavna^{3,4}, Andrew C. Oates^{5,6} and Luis G. Morelli^{7,8,9}

¹ Graduate School of Natural Science and Technology, Kanazawa University, Kanazawa, Japan

² Theoretical Biology Laboratory, RIKEN, Wako, Japan

³ Max Planck Institute of Molecular Cell Biology and Genetics, Dresden, Germany

⁴ Max Planck Institute for the Physics of Complex Systems, Dresden, Germany

⁵ The Francis Crick Institute, London, United Kingdom

⁶ Department of Cell and Developmental Biology, University College London, United Kingdom

⁷ Instituto de Investigación en Biomedicina de Buenos Aires (IBioBA) – CONICET – Partner Institute of the Max Planck Society, Buenos Aires, Argentina

⁸ Department of Systemic Cell Biology, Max Planck Institute for Molecular Physiology, Dortmund, Germany

⁹ Departamento de Física, FCEyN, UBA, Buenos Aires, Argentina

* Corresponding author

E-mail: uriu@staff.kanazawa-u.ac.jp (KU)

Key words: coupled oscillators, zebrafish, somitogenesis, cell mixing, imaging synchronization

Summary statement

We develop a framework to quantify and model cell mixing independent of a choice of reference frames and apply this to study oscillator synchronization in the zebrafish segmentation clock.

Abstract

In development and disease, cells move as they exchange signals. One example is found in vertebrate development, where the timing of segment formation is set by a “segmentation clock” in which oscillating gene expression is synchronized across a population of cells by Delta-Notch signaling. Delta-Notch signaling requires local cell-cell contact, but in the zebrafish embryonic tailbud oscillating cells move rapidly, exchanging neighbors. Previous theoretical studies proposed that this relative movement or cell mixing might alter signaling and thereby enhance synchronization. However, it remains unclear whether the mixing timescale in the tissue is in the right range for this effect, because a framework to reliably measure the mixing timescale and compare it with signaling timescale is lacking. Here, we develop such a framework using a quantitative description of cell mixing without the need for an external reference frame, and constructing a physical model of cell movement based on the data. Numerical simulations show that mixing with experimentally observed statistics enhances synchronization of coupled phase oscillators, suggesting that mixing in the tailbud is fast enough to affect the coherence of rhythmic gene expression. Our approach will find general application to analyzing the relative movements of communicating cells during development and disease.

Introduction

Tissue organization in animal embryos involves relative cell movement. The importance of cell movement in development has been emphasized, for example in gastrulation, tissue elongation, and neural development (Friedl and Gilmour, 2009; Rorth, 2009; Tada and Heisenberg, 2012). While on the move, cells communicate via mechanical and biochemical signaling and this can be local, for example when mediated by membrane-anchored proteins. Many developmental processes involve cell movement and local intercellular signaling simultaneously, which means that the relative durations, or timescales, of these processes may play a role in successful communication. Cells modify their internal states due to received signals and the time taken for this determines a signaling timescale. Movement that causes relative positional changes between cells is referred to as relative cell movement or cell mixing, and the time taken to exchange neighbors sets a mixing timescale. When the mixing timescale is similar to -or faster than- the local signaling timescale, cells can exchange neighbors and start new local interactions before completing the internal state change due to previous signaling events, and thus movement can affect the flow of information across a tissue (Uriu et al., 2014). However, little attention has been paid to the relation between the timescales of these two processes and how cell mixing affects local intercellular interactions and the resulting tissue organization.

In this paper, we develop a framework to analyze and model cell mixing quantitatively using zebrafish somitogenesis as a model system, and apply the framework to determine the impact of cell mixing on synchronization of genetic oscillators. In somitogenesis, multi-cellular tissue blocks termed somites bud off rhythmically from the anterior end of the unsegmented tissue, which consists of the presomitic mesoderm (PSM) and more posteriorly, the tailbud. The timing of somite formation is controlled by genes showing oscillatory waves of expression in PSM and tailbud (Soroldoni et al., 2014). In zebrafish, these genes include *her1*, *her7* and *deltaC* (Krol et al., 2011). Oscillatory expression is thought to be caused by delayed negative feedback regulation of *her1* and *her7* (Lewis, 2003; Schroter et al., 2012). These cells have been considered and modeled as a population of noisy autonomous oscillators (Webb et al., 2016) that can interact with neighboring cells through Delta-Notch signaling (Horikawa et al., 2006; Jiang et al., 2000; Riedel-Kruse et al., 2007). Blocking Notch signaling, either using mutants or a drug that blocks the activation of the Notch receptor (DAPT), revealed that synchronized oscillation of gene expression is necessary to make normal somites (Delaune et al., 2012; Liao et al., 2016; Mara et al., 2007; Ozbudak and

Lewis, 2008; Riedel-Kruse et al., 2007). Delta-Notch signaling also maintains synchronization between PSM cells in mouse embryos (Okubo et al., 2012; Shimojo et al., 2016) and tissue cultures (Tsiarlis and Aulehla, 2016). The collective rhythm arising from Delta-Notch interaction across the PSM is the temporal signal of a “segmentation clock” (Liao et al., 2016; Oates et al., 2012; Pourquie, 2011; Shimojo and Kageyama, 2016). In posterior PSM and tailbud, oscillation phase is spatially uniform, synchronized across the cell population.

Cells carrying the genetic oscillators move around, exchanging neighbors in posterior PSM and tailbud (Benazeraf et al., 2010; Delfini et al., 2005; Dray et al., 2013; Kulesa and Fraser, 2002; Lawton et al., 2013; Mara et al., 2007). Previous experiments focused on the role of cell movement in axis elongation using time-lapse imaging in zebrafish (Dray et al., 2013; Lawton et al., 2013; Mara et al., 2007; Steventon et al., 2016), and chick (Benazeraf et al., 2010; Delfini et al., 2005). Cells in PSM and tailbud extend protrusions (Benazeraf et al., 2010; Manning and Kimelman, 2015), and are thought to possess intrinsic motility. These studies also revealed signaling molecules driving cell movement in posterior PSM and tailbud of chick. Fgf forms a spatial gradient across the PSM with highest concentration in the tailbud (Dubrulle and Pourquie, 2004), and activates cell movement (Benazeraf et al., 2010; Delfini et al., 2005). Cells in anterior PSM show reduced cell movements due to low levels of Fgf signaling and epithelialization (Delfini et al., 2005). Combined, these experimental observations raise the question of how cell mixing in posterior PSM and tailbud influences synchronization of genetic oscillators.

Previous theoretical studies suggested that cell mixing in the tailbud could promote synchronization across a population of genetic oscillators (Uriu et al., 2012; Uriu and Morelli, 2014; Uriu et al., 2010). Movement of oscillators can effectively extend their interaction range (Fujiwara et al., 2011; Peruani et al., 2010; Uriu, 2016; Uriu et al., 2013). However, an enhancement of synchronization is only possible if the timescale of cell mixing is faster than the timescale of cell signaling. These previous theoretical studies assumed such faster cell mixing and analyzed its effect on synchronization of oscillators. While the timescale of cell signaling has been estimated from experiments where synchronization is perturbed by blocking Notch with DAPT (Herrgen et al., 2010; Riedel-Kruse et al., 2007), the timescale of cell mixing has not been measured. Previous studies of cell movement provided measurements of velocity and mean squared displacement (MSD) of single cells (Benazeraf et al., 2010; Lawton et al., 2013), but how often cells exchange neighbors has not yet been

quantified. For this, knowledge of the cells' velocity is not sufficient; rather the relative motion of cells is required. Furthermore, direct comparison between mixing and signaling timescales is not trivial because complex cell movement patterns in the zebrafish tailbud (Lawton et al. 2013) may prevent characterization of cell mixing with a single timescale (Uriu and Morelli 2017). Hence, a method to deal with these challenges rigorously and systematically needs to be developed.

Here we propose a framework motivated by the question of whether cell mixing in the zebrafish PSM is fast enough to affect synchronization of genetic oscillators. This starts with quantifying cell mixing across zebrafish PSM and tailbud using embryonic time-lapse images at single cell resolution. To characterize cell mixing we compute spatial derivatives of cell velocities and mean squared difference of displacement vectors (MSDD) (Uriu and Morelli, 2014) from cell-tracking data. This removes any global tissue motions in the imaging reference frame and yields the relative motion of cell-pairs. Then, we fit a physical model of cell movement and reproduce the cell mixing observed across the tissue. Finally, we simulate synchronization dynamics of coupled phase oscillators in the presence of reproduced cell mixing and show that the reproduced cell mixing enhances synchronization. Thus, the proposed approach gives a general and systematic framework to quantitatively analyze cell mixing in development. Its application suggests that cell mixing in zebrafish tailbud is indeed fast enough to affect synchronization dynamics of the segmentation clock.

Results

Single cell tracking

Cell movement can be estimated using the position of each cell's nucleus as a reference point. The nuclei of cells in tailbud, PSM and posterior somites in zebrafish embryos ($n = 4$) were imaged with high temporal resolution for an interval corresponding to the formation of one somite, starting at the 15-17 somite stage (ss) from a lateral orientation by confocal microscopy using a setup for multiple-embryo time-lapse recording (Fig. 1A and Movie 1) (Bhavna et al., 2016). To detect the position of each nucleus, we used the gradient vector diffusion algorithm proposed by Li et al (Li et al., 2007). For cell tracking, we adopted an algorithm based on nearest neighbor linking of objects between two successive time frames t and $t+1$ (Fig. 1B) (Sbalzarini and Koumoutsakos, 2005).

Validation of cell tracks

Embryos in this study were transgenic chimeras in which cells carrying both mCherry and GFP-tagged Histones as nuclear labels were transplanted at blastula stage to stage-matched host embryos carrying only GFP-Histone. The sparsely distributed mCherry nuclear signal was an internal ground-truth data set (Bhavna et al., 2016) to allow validation of our nuclear detection and cell-tracking algorithms (Supporting Text) (Bhavna et al., 2016). Parameters in the gradient vector diffusion algorithm were determined by calibration using synthetic images with similar nuclear density and image signal-to-noise ratios to our embryonic data. To quantify accuracy we defined sensitivity as the fraction of objects correctly detected by the algorithm to the total number of objects in a synthetic image, and precision as the fraction of correctly detected objects to the total number of detected objects (Supporting Text). The sensitivity of the algorithm with optimized parameter set was ~90% and precision was ~95% in synthetic images with relevant object densities (Fig. S1A). Sensitivity of the algorithm in transplanted embryos ranged between 0.96 and 0.98 (Fig. S1B). The fraction of cells with incorrect trajectories was low (0-2%, Fig. S1C,D). Although the tracking algorithm occasionally missed cells at some time point, resulting in a trajectory shorter than the recording's length (Fig. S1E), this does not lead to incorrect calculations of cell displacements in later analysis, which arise primarily from incorrect linking.

Cell mixing

A key property of cell movement that affects synchronization is local rearrangement, which will result in the mixing of neighboring oscillators (Uriu and Morelli, 2014). From cell trajectories it is straightforward to compute cell velocity. However, velocity computed in the lab reference frame includes contributions of spontaneous cell movement and also global tissue motion: embryos can move on the microscope stage, and the body axis deforms and elongates as a result of normal development. Consequently, velocity vectors in the lab reference frame do not reveal relative positional changes of cells. Below, we introduce two different methods to quantify cell mixing, namely the directional derivative of velocity vectors and the MSDD.

Directional derivative of velocity vectors. Local cell rearrangement may be quantified by the velocity difference of neighboring cells. A large velocity difference indicates that neighboring cells move in different directions resulting in relative positional changes. We

compute the difference of velocity vectors for a pair of neighboring cells i and j at position \mathbf{x}_i and \mathbf{x}_j as

$$D\mathbf{v}(\mathbf{x}_i)[\delta_{ij}] = \frac{\mathbf{v}(\mathbf{x}_j) - \mathbf{v}(\mathbf{x}_i)}{|\mathbf{x}_j - \mathbf{x}_i|} = \frac{\mathbf{v}(\mathbf{x}_i + \delta_{ij}) - \mathbf{v}(\mathbf{x}_i)}{|\delta_{ij}|}, \quad (1)$$

where $\delta_{ij} = \mathbf{x}_j - \mathbf{x}_i$. Eqn 1 approximates the spatial derivative of velocity vectors along vector δ_{ij} . We refer to $D\mathbf{v}(\mathbf{x}_i)[\delta_{ij}]$ as the directional derivative. To determine the magnitude of local velocity variations at cell position \mathbf{x}_i , we compute the average of directional derivative modulus over neighboring cells

$$D_v(\mathbf{x}_i) = \frac{1}{n_i} \sum_{j \in \{|\delta_{ij}| \leq \delta\}} |D\mathbf{v}(\mathbf{x}_i)[\delta_{ij}]|, \quad (2)$$

where n_i is the total number of neighboring cells satisfying $|\delta_{ij}| \leq \delta$ and summation is over all neighboring cells j . By subtracting two neighboring cells' velocities, the components of velocity drifts due to embryonic movement and tissue deformations are cancelled out, and only components due to relative movement remain. Thus, D_v is a proxy for the magnitude of cell mixing.

Fig. 1C shows the spatial profile of D_v along the PSM of a 17ss embryo. Based on the cell diameter estimated from the embryonic images (Fig. S2A, Supporting Text), we set $\delta = 16 \mu\text{m}$ in Eqn 2. The spatial gradient of D_v is highest at the posterior and progressively decreases in the anterior direction. Greater local velocity variations are observed in most cells in the tailbud, indicative of cell mixing, whereas few cells in anterior PSM have high values of D_v . These higher values may be local fluctuations of velocity vectors due to cell intercalations or extrusions. In addition, relatively higher D_v can be observed in cells in the connecting tissue between embryo and yolk because of this tissue's local deformation. We observed a similar spatial profile of D_v over time in the embryo (Fig. S3A-C). Spatial profiles of D_v among different embryos were quantitatively similar (Fig. S3D-F). Thus, the average directional derivative modulus indicates the presence of high cell mixing in the tailbud. We also quantified local velocity variations using strain rate tensor along the axis (Supporting Text) and obtained qualitatively similar spatial profiles of the magnitude of mixing (Fig. S4).

Mean squared difference of displacement vectors (MSDD). The directional derivatives contain information about short timescales of cell movement. To explore long time signatures of the movement pattern and reveal whether the cells' motion is relevant for synchronization, we introduced MSDD (Gerlich and Ellenberg, 2003; Uriu and Morelli, 2014). Using nuclear positions \mathbf{x}_i obtained by the tracking algorithm, MSDD $m(t)$ was defined as:

$$m(t) = \frac{1}{n_t} \sum_{i,j} \left| \left\{ \mathbf{x}_i(t + t_0^{(ij)}) - \mathbf{x}_i(t_0^{(ij)}) \right\} - \left\{ \mathbf{x}_j(t + t_0^{(ij)}) - \mathbf{x}_j(t_0^{(ij)}) \right\} \right|^2, \quad (3)$$

where $t_0^{(ij)}$ is the time when cells i and j , for the first time, satisfy $|\mathbf{x}_i(t_0^{(ij)}) - \mathbf{x}_j(t_0^{(ij)})| \leq r$ in the imaging period and n_t is the total number of pairs with the value t . Note, the value of $t_0^{(ij)}$ can be different for each pair of cells i and j . We set the distance threshold for averaging $r = 16 \mu\text{m}$, which is close to measured cell size (Fig. S2A). This restricts cell pairs to initial neighbors, avoiding the contribution of spatially heterogeneous tissue motions. The relation between MSDD and MSD is described in (Uriu and Morelli, 2017).

Fig. 2 shows time evolution of MSDD in three selected regions of a 17ss embryo. We set a three-dimensional box in a local region (Fig. 2A) and used cells within the box to compute MSDD defined in Eqn 3 (Materials and Methods). MSDD increased more rapidly in the posterior region than in the anterior, which indicated that relative cell movement was faster in the posterior than the anterior (Fig. 2B). This is consistent with analysis of directional derivative of velocity vectors (Fig. 1, Fig. S3) and strain rate tensor (Fig. S4) described above. We observed two regimes in MSDD curves. If cell movement was a random walk, we expect a linear increase of MSDD over time (Uriu and Morelli, 2017). For cells in the tailbud, MSDD increased almost linearly $m(t) \propto t$ at shorter time ($t < 3 \text{ min}$) while at longer time ($t > 3 \text{ min}$) it increased as a power law of t , $m(t) \propto t^{1.5}$. This exponent indicates that cell movement in zebrafish tailbud is not a simple random walk, in contrast to reported movements in chick embryos (Benazeraf et al., 2010). Note that this two-phase behavior of MSDD cannot be explained by a persistent random walk model because its MSDD should behave as $m(t) \propto t^2$ at shorter time (Gardiner, 2009). To confirm this behavior, we applied a second, recently proposed segmentation algorithm (Bhavna et al., 2016) and obtained similar results (Fig. S5).

In regions more anterior to the tailbud, we observed a similar tendency of the MSDD, but values of exponents decreased to less than one, indicating sub-diffusive cellular motions (Fig. 2B). We obtained quantitatively consistent MSDD among the other three embryos at similar developmental stages (Fig. S6).

Power law behaviors of MSDD described above preclude computation of a single timescale of cell mixing such as the diffusion constant of cells. This makes it difficult to directly compare the timescale of cell mixing and that of the phase dynamics of genetic oscillators (Uriu et al., 2013). To overcome this difficulty, we developed a physical model of cell

movement to reproduce the observed mixing in zebrafish embryos. Since cell tracking was performed using nuclear positions, we hypothesized that linear increase of MSDD at shorter time reflects motion of nucleus within cytoplasm, while power law increase at longer time indicates persistent cell movement constrained by neighboring cells. We tested this hypothesis by fitting the physical model to the MSDD data obtained from embryonic images.

Modeling cell movement

We chose a description of cell movement in PSM and tailbud allowing for direct comparison between timescales of cell mixing and oscillator phase dynamics. Because nuclei can move within cytoplasm and MSDD was computed with nuclear positions, the model describes movement of both cells and nuclei. Cells were described as spheres of diameter d_c in a confined three-dimensional space representing a local region somewhere in PSM or tailbud (Fig. 3A). The number of cells N in the model was set to fit cell density observed in embryos (Fig. S7, Supporting Text). We did not consider cell proliferation and apoptosis in the model. A similar description of a cell population was previously used to study synchronization dynamics (Tiedemann et al., 2012; Tiedemann et al., 2007; Tiedemann et al., 2014). However, this previous model did not consider cell movement.

We assumed that cells are self-propelled particles experiencing physical contact forces between them. We wrote the over-damped equation of motion for the cell center $\mathbf{x}_i(t)$ ($i = 1, 2, \dots, N$) (Uriu and Morelli, 2014):

$$\frac{d\mathbf{x}_i(t)}{dt} = v_0 \mathbf{n}_i(t) + \mu \sum_{\substack{j=1 \\ j \neq i}}^N \mathbf{F}(\mathbf{x}_i, \mathbf{x}_j) + \mathbf{F}_b(\mathbf{x}_i). \quad (4)$$

The first term describes spontaneous movement of cells. Without forces, cells move in direction \mathbf{n}_i at speed v_0 . This direction of spontaneous motion \mathbf{n}_i is a vector performing random walk on a unit sphere. Note that a cell moving at the instantaneous velocity $d\mathbf{x}_i/dt = v_0 \mathbf{n}_i$ possesses a finite persistence of direction of motions, as reported previously (Lawton et al., 2013; Manning and Kimelman, 2015). The second term describes volume exclusion forces between neighboring cells with a strength given by μ . Two cells at a distance closer than cell diameter d_c repel each other (Fig. 3A). The third term is the confinement force exerted by the domain boundaries.

Since we tracked cell nuclei in embryonic imaging data, we explicitly model nuclear motion inside a cell to consider its contribution to MSDD (Fig. 3A). Each nucleus is represented as a

sphere of radius r_n . We assumed that movement of the cell nucleus was random with a diffusion constant D_n , and confined to the cytoplasmic region within the cell diameter. See Supporting Text for implementation of the model.

Fig. 3B and Movie 2 show a simulation of the physical model. Note, we plotted only a subset of total cells in the simulation in Fig. 3B and Movie 2 for better visibility. The simulation had the same cell density as the actual tailbud (Fig. S7). We found that nuclear diffusive motions in the cytoplasm explained the linear increase of MSDD at shorter time (Fig. 3C). The nucleus did not move when the nuclear diffusion constant D_n was small. In such cases, instead of $m_s(t) \propto t$, MSDD at shorter time increased as $m_s(t) \propto t^2$ capturing short-time persistence of cell body motions (Fig. 3C). Thus, our physical model suggests that linear increase of MSDD at early times is caused by nuclear motion within a cell. In anterior PSM, the exponent of MSDD was less than one (Fig. 2B). This observation implies that both cell and nuclear movement become slower as cells leave the posterior PSM. In simulations in Fig. 3C, the power law increase in MSDD at longer time is due to the presence of a crossover between directed cellular motions at a shorter timescale and random motions at a longer timescale.

Fitting the physical model to embryonic MSDD data

To fit this physical model to experimentally obtained MSDD data in Fig. 2B, we adopted Approximated Bayesian Computation based on Markov chain Monte Carlo (ABC MCMC; Supporting Text) (Csillery et al., 2010; Sunnaker et al., 2013). ABC has previously been used to fit mathematical models to experimental data (Cohen et al., 2014; Marjoram et al., 2003). We computed MSDD in simulations using nuclear position for each cell. We defined the distance d_s between MSDD in simulation and experiment (Supporting Text). If d_s is small for a given parameter set, the simulation explains the experimental data well. ABC MCMC allows parameters in the model to be sampled from a conditional probability distribution $P(\mathcal{G} \mid d_s \leq \varepsilon)$, where ε represents a tolerance for fitting and \mathcal{G} represents the parameter set in the physical model.

We obtained values of cell density ρ , cell diameter d_c , and nuclear radius r_n by direct measurement from embryonic images (Figs. S2, S7; Supporting Text). The model includes six additional free parameters determined by ABC MCMC (Fig. S8A, B). We first focused on the tailbud. For illustration, we show that choosing a parameter set yielding a small value of d_s allowed the model to capture the features of the MSDD curve obtained by cell tracking in

embryos (Figs. 2B, S6; Tables S1, S2). Moreover, the fitted model could also reproduce the population average of directional derivative modulus observed in the tailbud (Fig. 3D), which was not used in ABC MCMC fitting. Using the fitted model we estimated single-cell speed and velocity auto-correlation in the tailbud (Fig. S9).

To check the model's consistency, we asked if the same model could reproduce the MSDD curves observed in anterior PSM. Given that the magnitude of cell mixing forms a spatial gradient across the PSM (Figs. 1,2) (Benazeraf et al., 2010; Delfini et al., 2005), we tuned the value of v_0 while matching the observed cellular density and fitted MSDD in anterior regions with all other parameters fixed at their values from the tailbud (Fig. 2B). The fitting became more difficult in anterior regions than in posterior, perhaps because the diffusion constant of the nucleus may also change along the PSM as cells become non-mobile in anterior regions. However, overall, the physical model could reproduce the MSDD observed in experiments in different regions of the PSM well with changes only to v_0 and the measured density (Fig. 2B). We also confirmed that the physical model with similar parameter values could reproduce MSDD in the other three imaged embryos (Fig. S6).

Synchronization of coupled mobile phase oscillators

Applying the physical model we investigated whether the observed tailbud cell mixing would be fast enough to affect segmentation clock synchronization. We simulated a coupled phase oscillator model to follow the dynamics of synchronization. Each oscillator resides on a cell in the physical model Eqn 4, which allows us to reproduce the experimentally observed cell mixing (reproduced mixing). Following previous studies (Kuramoto, 1984; Morelli et al., 2009; Riedel-Kruse et al., 2007; Uriu and Morelli, 2014), we introduced a population of phase oscillators θ_i ($i = 1, 2, \dots, N$) with autonomous frequency ω_i . The autonomous frequency obeys a normal distribution $\omega_i \sim N(\omega_0, \sigma_\omega)$, where ω_0 is mean and σ_ω is standard deviation of the distribution. We approximated the value of ω_0 from the somitogenesis period at our imaging temperature (40 min at 23°C) (Schroter et al., 2008). We assumed that cells signal to those cells touching them, that is when the distance between them is less than the cell diameter $|\mathbf{x}_j(t) - \mathbf{x}_i(t)| \leq d_c$. The equation for phase oscillators reads:

$$\frac{d\theta_i(t)}{dt} = \omega_i + \frac{\kappa}{n_i} \sum_{|\mathbf{x}_j - \mathbf{x}_i| \leq d_c} \sin(\theta_j(t) - \theta_i(t)) + \sqrt{2D_\theta} \zeta_{\theta i}(t), \quad (5)$$

where κ is coupling strength between oscillators, n_i is the number of contacting cells for cell i , D_θ is phase noise strength and $\zeta_{\theta i}$ is white Gaussian noise with $\langle \zeta_{\theta i}(t) \rangle = 0$ and $\langle \zeta_{\theta i}(t) \zeta_{\theta j}(t') \rangle = \delta_{ij} \delta(t - t')$. We adopted an open boundary condition in simulations of phase oscillators.

The key parameter in the coupled phase oscillator model is coupling strength κ , setting the timescale of change in phase due to interactions, $1/\kappa$. If the timescale of cell mixing is slower than $1/\kappa$, synchronization dynamics is almost the same as for non-mobile cells (Uriu et al., 2013). To examine how the effect of the observed mixing depends on coupling strength, we changed its value within a plausible range from $\kappa = 0.01 \text{ min}^{-1}$ to 0.11 min^{-1} , consistent with experimental estimates (Herrgen et al., 2010; Riedel-Kruse et al., 2007). Single-cell level observations of relatively slow resynchronization after cell divisions (Delaune et al., 2012) also support the above choice of the upper bound of the coupling strength.

To explore the effect of cell mixing, we compared synchronization dynamics of oscillators in the presence of reproduced mixing for the tailbud to that of non-mobile oscillators. To quantify the degree of phase synchronization in simulations, we introduced the Kuramoto phase order parameter (Kuramoto, 1984):

$$Z(t) = \frac{1}{N} \left| \sum_{j=1}^N e^{i\theta_j(t)} \right|, \quad (6)$$

where $i = \sqrt{-1}$. When oscillators are synchronized, the value of the order parameter is almost one, whereas when they are not, its value is close to zero.

During normal somitogenesis, the oscillators of the segmentation clock must maintain their phase synchronization in the presence of noise (Horikawa et al., 2006; Jiang et al., 2000; Riedel-Kruse et al., 2007). We first confirmed that the reproduced mixing could enhance robustness of the synchronized state against phase noise (Figs. S10A-C and S11).

We next asked how cell mixing affects dynamics towards the synchronized state. We simulated time evolution of Z from random phases at initial time, which represents the situation where the oscillators have been desynchronized by some external perturbation, for example a DAPT “wash-out” experiment (Liao et al., 2016; Riedel-Kruse et al., 2007). In the presence of DAPT, cells lose coupling and their phases desynchronize due to noise (Riedel-Kruse et al., 2007). After DAPT is washed out Delta-Notch signaling works again and cells rebuild coherent oscillations from random phases. Fig. 4A and Movies 3 and 4 show the spatial phase profiles developed from random initial phases in simulations. For illustration we set $\kappa = 0.07 \text{ min}^{-1}$, a value within the estimated range for the coupling strength (Herrgen et al., 2010; Riedel-Kruse et al., 2007). Non-mobile cells (top row Fig. 4A; Movie 3) first formed local phase

synchronization, which persisted and prevented the system from attaining global synchronization. Mobile cells also first formed local synchronization, but could then relax these local phase patterns and reach global synchronization quicker (bottom row Fig 4A; Movie 4).

The phase order parameter Z increased faster with reproduced mixing than without mixing (Fig. 4B), suggesting that observed cell mixing in tailbud could affect synchronization of coupled genetic oscillators *in vivo*. At short timescale ($< \sim 100$ min) the values of Z were almost the same between these two cases. During this period, oscillators quickly developed spatial phase patterns by local interactions. However, at around $t = 300$ min, we observed a difference in Z between these two cases. Although different parameter sets in the model for cell movement could reproduce MSDD data in tailbud (Fig. S8), we confirmed that time evolution of Z was comparable for similar MSDD time series (Fig. S8F). Thus, the specific values of parameters in the physical model are not critical, but the rate of MSDD increase determines synchronization dynamics of mobile coupled oscillators. We also confirmed that cell mixing in the tailbud of the other three imaged embryos enhanced synchronization (Fig. S12). For low coupling strength ($\kappa = 0.03 \text{ min}^{-1}$), the effect of mixing could be seen more clearly when simulations were started from random initial phases (Fig. S10D). Even for the largest tested coupling strength ($\kappa = 0.11 \text{ min}^{-1}$), we observed improvement by the reproduced mixing (Fig. S10F). Thus, within the estimated range of the coupling strength, observed cell mixing enhanced synchronization of oscillators.

In previous experimental studies, recovery of synchronization was quantified by the time taken for a normal somite to form after DAPT wash-out (Liao et al., 2016; Riedel-Kruse et al., 2007). This recovery time represents the time taken for the phase order parameter to surpass a certain threshold value Z_c : normal somites form when $Z \geq Z_c$. Using the simulated time series shown in Fig. 4B, we computed the first passage time τ of a given value of Z (Fig. 4C). The difference of first passage time between non-mobile and mobile oscillators became larger as Z increased. The time taken to reach Z_c can be measured in units of the 40-minute cycle of the clock, which represents the number of defective segments. The observed differences in the number of segment defects are displayed in Fig. 4C inset. For example, for $Z_c \sim 0.7$, without movement the embryo will make ~ 8 more defective segments than with reproduced mixing. Hence, the physical model predicts that recovery time of correct somite boundary formation would be strongly influenced by cell mixing.

Taken together, these results suggest that there is a biologically plausible range of coupling strength where the reproduced cell mixing significantly promotes synchronization of coupled phase oscillators. Thus, our quantification of mixing in the developing zebrafish embryo combined with theoretical modeling supports the hypothesis that cell mixing in the tailbud may promote synchronization of the segmentation clock.

Discussion

Previous studies on cell movement in development have often focused on the role of relative cell movement in perturbing patterns established by signaling systems. Examples include effects of cell divisions and intercalations on tissue boundary formation in *Drosophila* wing disc and vertebrate hindbrain (Dahmann et al., 2011). In these and similar cases, cell mixing decreases the reliability of the pattern, and mechanisms have been discovered that restrict mixing at the boundary. In contrast, local cell-sorting can correct an initial spatially noisy specification of cell types to a sharp boundary (Xiong et al., 2013). In the segmentation clock, the synchronization of noisy neighboring oscillators is a key step in the generation of a coherent pattern that leads to reliable somite boundaries at the anterior end of the PSM (Delaune et al., 2012; Jiang et al., 2000; Riedel-Kruse et al., 2007). How mixing of cells in PSM and tailbud affects this patterning system is not yet understood.

Here, we developed a framework to analyze and model cell mixing in embryonic tissues, and used a quantitative model to investigate whether the observed mixing in the zebrafish tailbud could affect synchronization of genetic oscillators. We computed directional derivatives of velocity vectors and MSDD to quantify cell mixing across PSM and tailbud (Figs. 1 and 2). Then, we fitted a physical model of cell movement to experimental data and reproduced this cell mixing in simulations (Figs. 2 and 3). Finally, by simulating a coupled phase oscillator model (Fig. 4) with previously estimated coupling parameter values, we showed that the reproduced mixing was fast enough to promote synchronization.

Setting a reference frame for cell movement is key to quantification, otherwise global tissue movements influence analysis. Previous studies quantified cell movement in PSM and tailbud to examine its influence on axis elongation (Benazeraf et al., 2010; Dray et al., 2013; Lawton et al., 2013). Setting a reference frame for cellular motions is key to quantification, otherwise global tissue movements influence analysis. These previous studies used extracellular matrix or position of the anterior PSM to set the reference frame. The average position of tracked cells has also been used as a local reference frame when cell movements are confined within

a smaller region of the tissue. Alternatively, image registration algorithms may remove cell displacements caused by embryonic motions. In this study we take a simpler and more direct approach that focuses on relative motions and does not rely on a choice of reference frame by adopting the spatial derivative of velocity vectors and the difference of displacement vectors, the MSDD.

We observed two different regimes of MSDD in 15-17ss embryos imaged at 23°C. At shorter times MSDD increased almost linearly over time. We explained these shorter time behaviors by nuclear motions (Fig. 3C). Indeed, diffusive nuclear motions in the cytoplasm have been observed in mesenchymal cells migrating on a two-dimensional substrate (Liu et al., 2015). At longer times MSDD increased as a power law with an exponent larger than one. We explained this power law increase by persistent cell movement (Figs. 3 and S9). A previous study using zebrafish embryos at 10ss growing at 18°C showed that MSD for single cells in the tailbud increases as a power law of time and that the exponents are larger than one (Lawton et al., 2013). MSDDs from this data set determined with our methods also showed power law exponents greater than one (Fig. S13), and were similar to those for 15-17ss embryos imaged in the present study. Thus, both previous and present studies indicate that cell movement is not a simple random walk in zebrafish posterior PSM. Furthermore, the similar rate of MSDD increase observed in those 10ss embryos (Fig. S13) suggests that cell mixing at this earlier developmental stage would also influence synchronization of oscillators.

Previous theoretical studies examined the effect of cell mixing on synchronization of genetic oscillators in the tailbud with an assumption that cell mixing timescale is faster than signaling timescale defined by the inverse coupling strength $1/\kappa$ (Uriu et al., 2012; Uriu and Morelli, 2014; Uriu et al., 2010). This critical assumption, however, has not been tested experimentally. In general, complex cell movement patterns in developing tissues would exclude the characterization of cell mixing with a single timescale, as shown in Fig. 3 (Uriu and Morelli, 2017). The framework proposed here can predict the impact of observed cell mixing on signaling even when cell mixing and signaling includes multiple timescales. Current and previous modeling (Uriu and Morelli, 2014) indicate that a main determinant of synchronization dynamics is the rate of MSDD increase (Fig. S8). This is an increasing function of the ratio v_0/μ in Eq. (4) and its estimated values are within the range of 0.16-0.3 (Table S1). Although these obtained values are smaller than those assumed in a previous study (Uriu and Morelli, 2014), the observed mixing does enhance synchronization in this

range (Figs. 4, S12). Collective behaviors of mobile interacting agents are relevant to not only biology but also physics (Fujiwara et al., 2011; Levis et al., 2017; Peruani et al., 2010) and technology (Wang et al., 2009). Determining whether the mobility of agents is faster than the timescale of interactions is an important step to analyze such systems as well.

A striking feature of the data is the gradient of cell mixing, highest in tailbud and lowest in anterior PSM, as previously noted (Benazeraf et al., 2010; Lawton et al., 2013). One implication of our findings is that there may exist a threshold in the PSM at which cell mixing is no longer beneficial for synchronization (Fig. 5). Oscillations in PSM are organized as waves of gene expression that sweep from posterior to anterior. A wave slows as it moves anteriorly and stops where the next somite boundary will form (Aulehla et al., 2008; Soroldoni et al., 2014). Accordingly, the wavelength of the gene expression stripes becomes shorter in the anterior PSM, approaching that of the somite length. If cells moved faster than gene expression waves, stripe boundaries would be blurred. Thus, slow cell mixing observed in the anterior is consistent with the formation of sharp somite boundaries. In contrast, the effective interaction range (Uriu et al., 2013) introduced by fast cell mixing in the tailbud is smaller than the large wavelength spanning this region (Soroldoni et al., 2014) and smaller than tailbud size (Fig. S14; Supporting Text). Robust synchronization by cell mixing in the tailbud (Figs. S10 and S11) is important because cells leave the tailbud carrying their local phase order and emerge into the PSM, where a failure in synchronization causes local defects in the gene expression stripes, resulting in defective segment boundary formation.

A second implication is that the mixing of cells may itself influence the wave pattern. Synchronized cells leave the tailbud and enter the PSM where they participate in formation of gene expression stripes with sharp boundaries, as described above. Notably, for some intermediate region of the PSM, cell mixing would be still fast enough to affect synchronization while the wavelength of gene expression pattern is shortening. Because coupling between oscillators influences the wavelength of gene expression stripes (Ares et al., 2012; Jörg et al., 2015; Murray et al., 2011) and cell mixing extends the range of coupling (Fujiwara et al., 2011; Peruani et al., 2010; Uriu et al., 2013), cell mixing may therefore influence the wavelength of gene expression patterns in this intermediate PSM region. An extended theory that describes the entire PSM and incorporates cell mixing data along the axis will reveal to what extent cell mixing affects the wavelength. Direct experimental tests of these predictions will require means of locally controlling the mixing of cells in the tissue.

Our current analysis suggests that cell mixing in the tailbud is fast enough to influence the dynamics of coupled genetic oscillators in the segmentation clock. A key experiment for testing the theory in living embryos would be to inhibit cell movement with drugs or mutants. A previous study on axial elongation used a drug called blebbistatin to inhibit myosin and block cell movement (Benazeraf et al., 2010). Using the framework we developed in this paper, one could ask whether impaired cell movement in experimentally treated embryos is enough to slow synchronization dynamics. Previous estimates of the synchronization state (phase order parameter) in the embryo have relied on morphological proxies such as the correct formation of segment boundaries (Riedel-Kruse et al., 2007), which can be modeled by first passage time (Fig. 4C). However, it remains unclear what is the value of the synchronization state that determines the formation of a normal or defective segment boundary. Recently-developed live reporters for oscillatory proteins (Delaune et al., 2012; Soroldoni et al., 2014), which should allow direct measurement of the synchronization state and dynamics are therefore key to testing the theory.

In summary, our study provides a rigorous and systematic framework to investigate cell mixing in one embryological context where the timescale of cell mixing can be faster than that of intercellular signaling. Relative cell movement may also influence intercellular signaling in other contexts (Uriu et al., 2014), for example in collective migration or gastrulation, or in cultured cell populations with Delta-Notch signaling (Matsuda et al., 2015; Tsiairis and Aulehla, 2016). In addition, for cells under signaling gradients, the relative timescales between mixing and cell type specification by signaling would be important for patterning (Xiong et al., 2013). The ratio of timescales between mixing and signaling determines the impact of mixing (Uriu et al., 2013). In general, quantification of the mixing timescale from imaging data will be simpler than the signaling timescale. Approaches to quantify the influence of cell movement on signaling such as those presented here will be important to understand other similar processes in development and disease.

Materials and Methods

Imaging setup. Time-lapse imaging data was from (Bhavna et al., 2016).

Cell-tracking algorithm and validation. The gradient vector diffusion algorithm (Li et al., 2007) was used for detecting positions of cell nuclei. Parameter values are listed in Table S4. For cell tracking, the algorithm proposed in (Sbalzarini and Koumoutsakos, 2005) was used

(Supporting Text). Validation of these two algorithms was done following (Bhavna et al., 2016) using synthetic images and three images of chimeric embryos (Supporting Text). In addition, a recently proposed nuclear segmentation algorithm (Bhavna et al., 2016) was applied to the imaging data to test whether it gave similar MSDD time series (Fig. S5).

Cell density measurement. The number of cell nuclei in a three dimensional box ($42 \times 42 \times 20 \mu\text{m}^3$; Fig. S7) was counted and divided by the box's volume. The box was located $20 \mu\text{m}$ away from epithelial tissues to fill the entire region of the box with mesenchymal cells.

Velocity vector in lab reference frame. Velocity vectors for calculation of directional derivative and strain rate tensor were defined as:

$$\mathbf{v}_i(t) = \{\mathbf{x}_i(t + \Delta t) - \mathbf{x}_i(t)\} / \Delta t, \quad (7)$$

where $\mathbf{x}_i(t)$ is the position of cell i at time t obtained by the tracking algorithm. Δt was set = 5 (min) to avoid seeing only the fluctuation of a cell nucleus. The same definition of velocity was used in simulations of cell movement.

Voronoi tessellation. A three dimensional Voronoi tessellation algorithm in Matlab R2014b "delaunayn" was applied to nuclear position data to determine neighbor relations among cells. Distances between Voronoi neighbors were calculated by a Matlab custom code.

Measurement of nucleus size. The long axis of a nucleus was visually determined in a x - y plane of image stacks. For this, each x - y plane containing the nucleus was visually scanned in z direction. When the size of the nucleus reached maximum, the length of its long axis was measured in that plane with the line tool from Fiji.

Fitting by ABC MCMC. The algorithm proposed in (Marjoram et al., 2003) was used. Parameters values are listed in Table S5 (Supporting Text). Custom code for ABC MCMC was written in C language.

Strain rate tensor. To construct a continuum velocity vector field $\mathbf{v}(t, \mathbf{x})$ in a three-dimensional space from the data for cell velocity vectors $\mathbf{v}_i(t, \mathbf{x}_i)$, the smoothed particle hydrodynamics (SPH) approach was used. Strain rate tensor was then computed using the continuum velocity vector field (Supporting Text).

Mean squared difference of displacement vectors. Boxes of size $48 \times 48 \times z \text{ } \mu\text{m}^3$ ($z = 47$ for 15ss, 61 for 16ss and 42 for two 17ss embryos) were set in PSM and tailbud (Fig. 2A) and cells within each box during imaging period were used for computation of MSDD using Eqn 3.

Numerical integration of differential equations. The stochastic differential equations 4 and 5 were solved with the Euler-Maruyama method with time step $\Delta t = 0.01$. Custom code was written in C language.

Acknowledgments

We thank Sundar Naganathan for helpful comments on the manuscript. We thank Scott Holley for providing us with raw experimental data from (Lawton et al., 2013).

Competing interests

The authors declare no competing or financial interests.

Author contributions

Conceived the study: K.U., R.B., A.C.O., and L.G.M. Developed methodologies: K.U. and L.G.M. Performed simulations: K.U. Analyzed the data: K.U., R.B., A.C.O., and L.G.M. Wrote the manuscript: K.U., R.B., A.C.O., and L.G.M.

Funding

This work was supported by JSPS KAKENHI [26840085] to K.U.; RIKEN iTHES Project to K.U.; Kanazawa University Discovery Initiative program to K.U.; FY2014 Researcher Exchange Program between JSPS and CONICET to K.U. and L.G.M.; Max Planck Society through the Max Planck Institute of Molecular Cell Biology and Genetics to R.B. and A.C.O.; European Research Council under the European Communities 7th Framework Programme [FP7/20072013]/[ERC grant 207634] to R.B. and A.C.O.; The Francis Crick Institute, which receives its core funding from Cancer Research UK, the UK Medical Research Council, and the Wellcome Trust to A.C.O.; The Wellcome Trust [WT098025MA] to A.C.O.; The Medical Research Council [MC_UP_1202/3] to A.C.O.; PICT 2012 1954 to L.G.M.; PICT 2013 1301 to L.G.M.; and FOCM-Mercosur (COF 03/11) to L.G.M.

References

- Annala, T., Lihavainen, E., Marques, I. J., Williams, D. R., Yli-Harja, O. and Ribeiro, A.** (2013). ZebIAT, an image analysis tool for registering zebrafish embryos and quantifying cancer metastasis. *BMC Bioinformatics* **14 Suppl 10**, S5.
- Ares, S., Morelli, L. G., Jorg, D. J., Oates, A. C. and Julicher, F.** (2012). Collective modes of coupled phase oscillators with delayed coupling. *Phys. Rev. Lett.* **108**, 204101.
- Aulehla, A., Wiegraebe, W., Baubet, V., Wahl, M. B., Deng, C., Taketo, M., Lewandoski, M. and Pourquie, O.** (2008). A beta-catenin gradient links the clock and wavefront systems in mouse embryo segmentation. *Nat. Cell Biol.* **10**, 186-193.
- Benazeraf, B., Francois, P., Baker, R. E., Denans, N., Little, C. D. and Pourquie, O.** (2010). A random cell motility gradient downstream of FGF controls elongation of an amniote embryo. *Nature* **466**, 248-252.
- Bhavna, R., Uriu, K., Valentin, G., Tinevez, J. Y. and Oates, A. C.** (2016). Object Segmentation and Ground Truth in 3D Embryonic Imaging. *PLoS One* **11**, e0150853.
- Cohen, M., Page, K. M., Perez-Carrasco, R., Barnes, C. P. and Briscoe, J.** (2014). A theoretical framework for the regulation of Shh morphogen-controlled gene expression. *Development* **141**, 3868-3878.
- Csillery, K., Blum, M. G., Gaggiotti, O. E. and Francois, O.** (2010). Approximate Bayesian Computation (ABC) in practice. *Trends Ecol. Evol.* **25**, 410-418.
- Dahmann, C., Oates, A. C. and Brand, M.** (2011). Boundary formation and maintenance in tissue development. *Nat. Rev. Genet.* **12**, 43-55.
- Delaune, E. A., Francois, P., Shih, N. P. and Amacher, S. L.** (2012). Single-cell-resolution imaging of the impact of Notch signaling and mitosis on segmentation clock dynamics. *Dev. Cell* **23**, 995-1005.
- Delfini, M. C., Dubrulle, J., Malapert, P., Chal, J. and Pourquie, O.** (2005). Control of the segmentation process by graded MAPK/ERK activation in the chick embryo. *Proc Natl Acad Sci U S A* **102**, 11343-11348.
- Dray, N., Lawton, A., Nandi, A., Julich, D., Emonet, T. and Holley, S. A.** (2013). Cell-fibronectin interactions propel vertebrate trunk elongation via tissue mechanics. *Curr. Biol.* **23**, 1335-1341.
- Dubrulle, J. and Pourquie, O.** (2004). fgf8 mRNA decay establishes a gradient that couples axial elongation to patterning in the vertebrate embryo. *Nature* **427**, 419-422.
- Friedl, P. and Gilmour, D.** (2009). Collective cell migration in morphogenesis, regeneration and cancer. *Nat. Rev. Mol. Cell Biol.* **10**, 445-457.

- Fujiwara, N., Kurths, J. and Diaz-Guilera, A.** (2011). Synchronization in networks of mobile oscillators. *Phys Rev E Stat Nonlin Soft Matter Phys* **83**, 025101.
- Gardiner, C.** (2009). *Stochastic Methods: A handbook for the natural and social sciences* (4th edn). Heidelberg: Springer-Verlag.
- Gerlich, D. and Ellenberg, J.** (2003). 4D imaging to assay complex dynamics in live specimens. *Nat. Cell Biol. Suppl*, S14-19.
- Herrgen, L., Ares, S., Morelli, L. G., Schroter, C., Julicher, F. and Oates, A. C.** (2010). Intercellular coupling regulates the period of the segmentation clock. *Curr. Biol.* **20**, 1244-1253.
- Horikawa, K., Ishimatsu, K., Yoshimoto, E., Kondo, S. and Takeda, H.** (2006). Noise-resistant and synchronized oscillation of the segmentation clock. *Nature* **441**, 719-723.
- Jiang, Y. J., Aerne, B. L., Smithers, L., Haddon, C., Ish-Horowicz, D. and Lewis, J.** (2000). Notch signalling and the synchronization of the somite segmentation clock. *Nature* **408**, 475-479.
- Jörg, D. J., Morelli, L. G., Soroldoni, D., Oates, A. C. and Jülicher, F.** (2015). Continuum theory of gene expression waves during vertebrate segmentation. *New Journal of Physics* **17**, 093042.
- Krol, A. J., Roellig, D., Dequeant, M. L., Tassy, O., Glynn, E., Hattem, G., Mushegian, A., Oates, A. C. and Pourquie, O.** (2011). Evolutionary plasticity of segmentation clock networks. *Development* **138**, 2783-2792.
- Kulesa, P. M. and Fraser, S. E.** (2002). Cell dynamics during somite boundary formation revealed by time-lapse analysis. *Science* **298**, 991-995.
- Kuramoto, Y.** (1984). *Chemical oscillations, waves, and turbulence*. Berlin: Springer-Verlag.
- Lawton, A. K., Nandi, A., Stulberg, M. J., Dray, N., Sneddon, M. W., Pontius, W., Emonet, T. and Holley, S. A.** (2013). Regulated tissue fluidity steers zebrafish body elongation. *Development* **140**, 573-582.
- Levis, D., Pagonabarraga, I. and Díaz-Guilera, A.** (2017). Synchronization in dynamical networks of locally coupled self-propelled oscillators. *Phys Rev X* **7**, 011028.
- Lewis, J.** (2003). Autoinhibition with transcriptional delay: a simple mechanism for the zebrafish somitogenesis oscillator. *Curr. Biol.* **13**, 1398-1408.
- Li, G., Liu, T., Nie, J., Guo, L., Malicki, J., Mara, A., Holley, S. A., Xia, W. and Wong, S. T.** (2007). Detection of blob objects in microscopic zebrafish images based on gradient vector diffusion. *Cytometry. Part A : the journal of the International Society for Analytical Cytology* **71**, 835-845.

- Liao, B. K., Jorg, D. J. and Oates, A. C.** (2016). Faster embryonic segmentation through elevated Delta-Notch signalling. *Nat Commun* **7**, 11861.
- Liu, Y. J., Le Berre, M., Lautenschlaeger, F., Maiuri, P., Callan-Jones, A., Heuze, M., Takaki, T., Voituriez, R. and Piel, M.** (2015). Confinement and low adhesion induce fast amoeboid migration of slow mesenchymal cells. *Cell* **160**, 659-672.
- Manning, A. J. and Kimelman, D.** (2015). Tbx16 and Msgn1 are required to establish directional cell migration of zebrafish mesodermal progenitors. *Dev. Biol.* **406**, 172-185.
- Mara, A., Schroeder, J., Chalouni, C. and Holley, S. A.** (2007). Priming, initiation and synchronization of the segmentation clock by deltaD and deltaC. *Nat. Cell Biol.* **9**, 523-530.
- Marjoram, P., Molitor, J., Plagnol, V. and Tavaré, S.** (2003). Markov chain Monte Carlo without likelihoods. *Proc Natl Acad Sci U S A* **100**, 15324-15328.
- Matsuda, M., Koga, M., Woltjen, K., Nishida, E. and Ebisuya, M.** (2015). Synthetic lateral inhibition governs cell-type bifurcation with robust ratios. *Nat Commun* **6**, 6195.
- Morelli, L. G., Ares, S., Herrgen, L., Schroter, C., Julicher, F. and Oates, A. C.** (2009). Delayed coupling theory of vertebrate segmentation. *HFSP J* **3**, 55-66.
- Murray, P. J., Maini, P. K. and Baker, R. E.** (2011). The clock and wavefront model revisited. *J. Theor. Biol.* **283**, 227-238.
- Oates, A. C., Morelli, L. G. and Ares, S.** (2012). Patterning embryos with oscillations: structure, function and dynamics of the vertebrate segmentation clock. *Development* **139**, 625-639.
- Okubo, Y., Sugawara, T., Abe-Koduka, N., Kanno, J., Kimura, A. and Saga, Y.** (2012). Lfng regulates the synchronized oscillation of the mouse segmentation clock via trans-repression of Notch signalling. *Nat Commun* **3**, 1141.
- Ozbudak, E. M. and Lewis, J.** (2008). Notch signalling synchronizes the zebrafish segmentation clock but is not needed to create somite boundaries. *PLoS Genet.* **4**, e15.
- Peruani, F., Nicola, E. M. and Morelli, L. G.** (2010). Mobility induces global synchronization of oscillators in periodic extended systems. *New Journal of Physics* **12**, 093029.
- Pourquie, O.** (2011). Vertebrate segmentation: from cyclic gene networks to scoliosis. *Cell* **145**, 650-663.
- Qu, L., Long, F. and Peng, H.** (2015). 3-D Registration of Biological Images and Models: Registration of microscopic images and its uses in segmentation and annotation. *IEEE*

- Riedel-Kruse, I. H., Muller, C. and Oates, A. C.** (2007). Synchrony dynamics during initiation, failure, and rescue of the segmentation clock. *Science* **317**, 1911-1915.
- Rorth, P.** (2009). Collective cell migration. *Annu. Rev. Cell. Dev. Biol.* **25**, 407-429.
- Sbalzarini, I. F. and Koumoutsakos, P.** (2005). Feature point tracking and trajectory analysis for video imaging in cell biology. *Journal of structural biology* **151**, 182-195.
- Schroter, C., Ares, S., Morelli, L. G., Isakova, A., Hens, K., Soroldoni, D., Gajewski, M., Julicher, F., Maerkl, S. J., Deplancke, B., et al.** (2012). Topology and dynamics of the zebrafish segmentation clock core circuit. *PLoS Biol.* **10**, e1001364.
- Schroter, C., Herrgen, L., Cardona, A., Brouhard, G. J., Feldman, B. and Oates, A. C.** (2008). Dynamics of zebrafish somitogenesis. *Dev. Dyn.* **237**, 545-553.
- Shimojo, H., Isomura, A., Ohtsuka, T., Kori, H., Miyachi, H. and Kageyama, R.** (2016). Oscillatory control of Delta-like1 in cell interactions regulates dynamic gene expression and tissue morphogenesis. *Genes Dev.* **30**, 102-116.
- Shimojo, H. and Kageyama, R.** (2016). Oscillatory control of Delta-like1 in somitogenesis and neurogenesis: A unified model for different oscillatory dynamics. *Semin. Cell Dev. Biol.*
- Soroldoni, D., Jorg, D. J., Morelli, L. G., Richmond, D. L., Schindelin, J., Julicher, F. and Oates, A. C.** (2014). Genetic oscillations. A Doppler effect in embryonic pattern formation. *Science* **345**, 222-225.
- Steventon, B., Duarte, F., Lagadec, R., Mazan, S., Nicolas, J. F. and Hirsinger, E.** (2016). Species-specific contribution of volumetric growth and tissue convergence to posterior body elongation in vertebrates. *Development* **143**, 1732-1741.
- Sunnaker, M., Busetto, A. G., Numminen, E., Corander, J., Foll, M. and Dessimoz, C.** (2013). Approximate Bayesian computation. *PLoS Comput Biol* **9**, e1002803.
- Tada, M. and Heisenberg, C. P.** (2012). Convergent extension: using collective cell migration and cell intercalation to shape embryos. *Development* **139**, 3897-3904.
- Tiedemann, H. B., Schneltzer, E., Zeiser, S., Hoesel, B., Beckers, J., Przemeck, G. K. and de Angelis, M. H.** (2012). From dynamic expression patterns to boundary formation in the presomitic mesoderm. *PLoS Comput Biol* **8**, e1002586.
- Tiedemann, H. B., Schneltzer, E., Zeiser, S., Rubio-Aliaga, I., Wurst, W., Beckers, J., Przemeck, G. K. and Hrabe de Angelis, M.** (2007). Cell-based simulation of dynamic expression patterns in the presomitic mesoderm. *J. Theor. Biol.* **248**, 120-129.
- Tiedemann, H. B., Schneltzer, E., Zeiser, S., Wurst, W., Beckers, J., Przemeck, G. K. and**

- Hrabe de Angelis, M.** (2014). Fast synchronization of ultradian oscillators controlled by delta-notch signaling with cis-inhibition. *PLoS Comput Biol* **10**, e1003843.
- Tsaiiris, C. D. and Aulehla, A.** (2016). Self-Organization of Embryonic Genetic Oscillators into Spatiotemporal Wave Patterns. *Cell* **164**, 656-667.
- Uriu, K.** (2016). Genetic oscillators in development. *Dev. Growth Differ.* **58**, 16-30.
- Uriu, K., Ares, S., Oates, A. C. and Morelli, L. G.** (2012). Optimal cellular mobility for synchronization arising from the gradual recovery of intercellular interactions. *Phys Biol* **9**, 036006.
- Uriu, K., Ares, S., Oates, A. C. and Morelli, L. G.** (2013). Dynamics of mobile coupled phase oscillators. *Physical Review E* **87**, 032911.
- Uriu, K. and Morelli, L. G.** (2014). Collective cell movement promotes synchronization of coupled genetic oscillators. *Biophys. J.* **107**, 514-526.
- Uriu, K. and Morelli, L. G.** (2017). Determining the impact of cell mixing on signaling during development. *Dev. Growth Differ.*, in press.
- Uriu, K., Morelli, L. G. and Oates, A. C.** (2014). Interplay between intercellular signaling and cell movement in development. *Semin. Cell Dev. Biol.* **35**, 66-72.
- Uriu, K., Morishita, Y. and Iwasa, Y.** (2010). Random cell movement promotes synchronization of the segmentation clock. *Proc Natl Acad Sci U S A* **107**, 4979-4984.
- Wang, P., Gonzalez, M. C., Hidalgo, C. A. and Barabasi, A. L.** (2009). Understanding the spreading patterns of mobile phone viruses. *Science* **324**, 1071-1076.
- Webb, A. B., Lengyel, I. M., Jorg, D. J., Valentin, G., Julicher, F., Morelli, L. G. and Oates, A. C.** (2016). Persistence, period and precision of autonomous cellular oscillators from the zebrafish segmentation clock. *Elife* **5**.
- Xiong, F., Tentner, A. R., Huang, P., Gelas, A., Mosaliganti, K. R., Souhait, L., Rannou, N., Swinburne, I. A., Obholzer, N. D., Cowgill, P. D., et al.** (2013). Specified neural progenitors sort to form sharp domains after noisy Shh signaling. *Cell* **153**, 550-561.

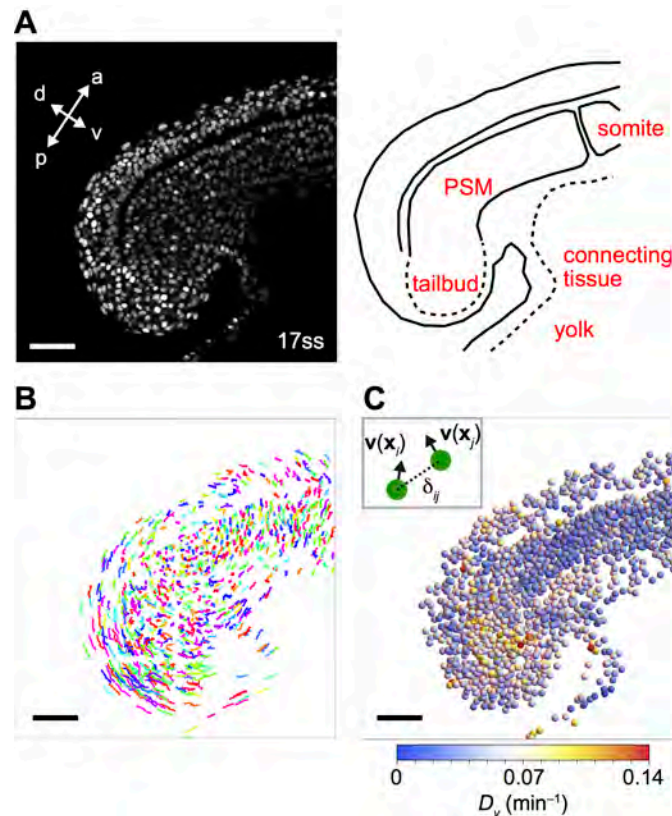


Fig 1. Quantification of cell mixing by the average directional derivative modulus of cell velocity vectors. (A) Left: Snapshot of a 17 somite stage (ss) embryo, nuclei labeled with Histone *h2AflV-gfp*. a: anterior, p: posterior, d: dorsal and v: ventral. Right: schematic picture of PSM and tailbud. See also Movie 1. (B) Cell trajectories for embryo shown in (A) obtained by nuclear detection and tracking algorithms. Trajectories from time frame 1 to 20 (16.7 min) plotted in three dimensional space. Each trajectory is assigned a color randomly. (C) Spatial profile of average directional derivative modulus of cell velocity vectors D_v for 17 ss embryo shown in (A). Spheres represent positions of cells. Radius of spheres was chosen for better visibility. Scale bars = 50 μm , (A)-(C).

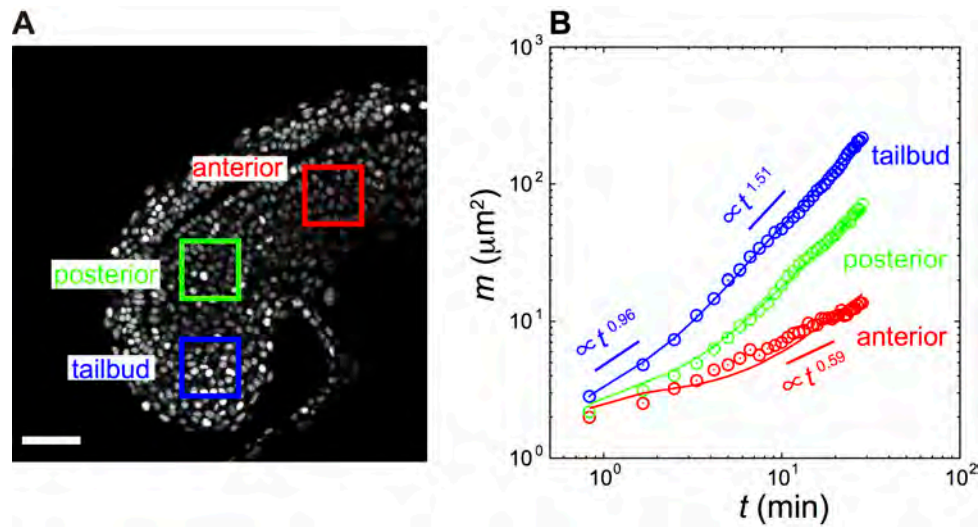


Fig 2. Quantification of cell mixing by the mean squared difference of displacement vectors (MSDD). (A) Snapshot of 17 ss embryo. Colored boxes indicate regions for which MSDD was calculated in (B). (B) MSDD computed from Eqn 3 at each region of PSM and tailbud as a function of time. Circles represent experimental data. Lines are fit by the physical model of cell movement to experimental data. Tables S1 and S2 give parameter values in the physical model. Scale bar = 50 μm in (A).

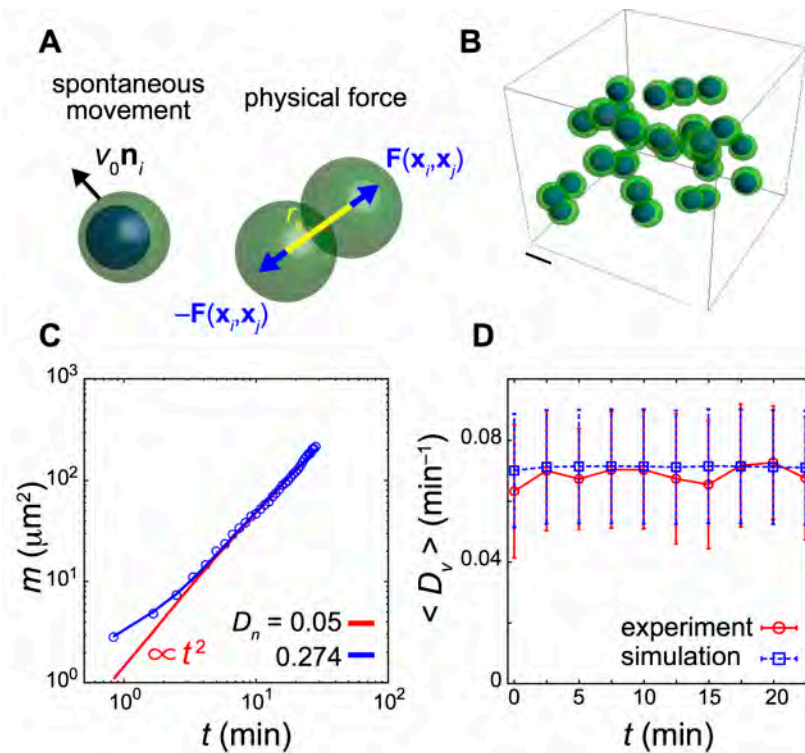


Fig 3. Physical model for cell movement. (A) Left: Cell in a three dimensional space is represented as a sphere (green). Blue sphere inside indicates cell nucleus. The unit vector \mathbf{n}_i represents polarity for spontaneous cell movement. Right: Repulsive physical forces between two neighboring cells. (B) Snapshot of a simulation. 30/346 cells are plotted. Scale bar = 10 μm . See Movie 2. (C) MSDD as a function of time. Lines indicate simulation results for different values of nuclear diffusion constant D_n . Circles indicate experimental data for tailbud cells in Fig. 2B. (D) Time series of population average of directional derivative modulus D_v for embryonic tailbud region (red circles; experiment) and for simulations of the fitted physical model (blue squares; simulation). Embryonic data in Figs. 1C and S3 were used to compute population average of D_v . Error bars indicate standard deviations.

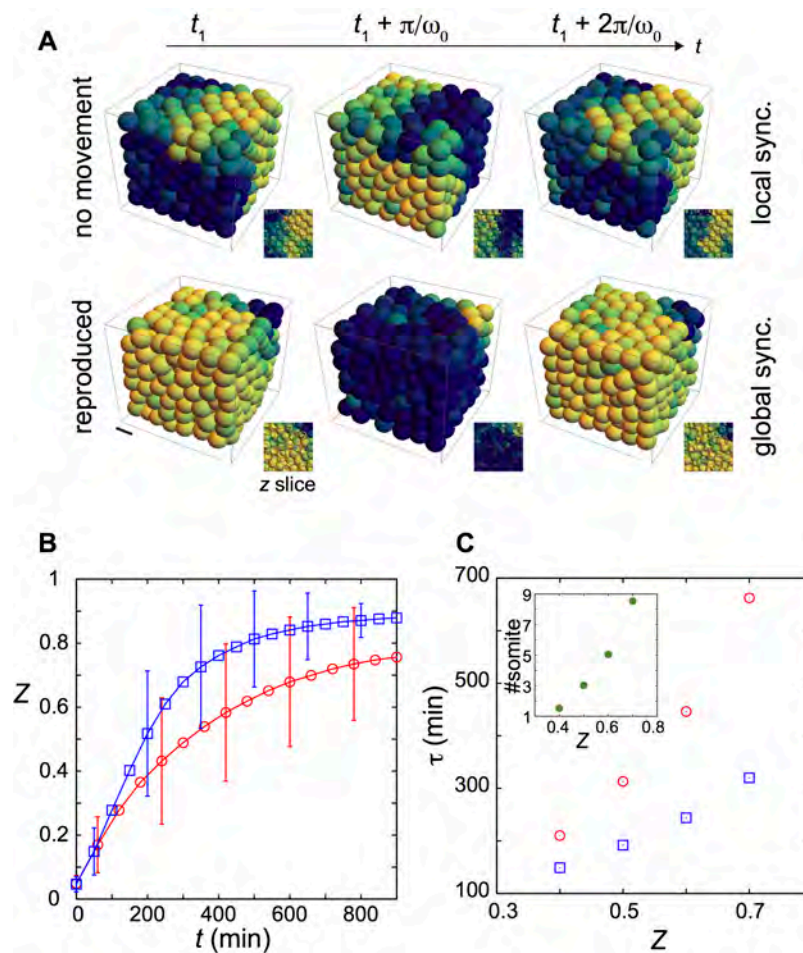


Fig 4. Synchronization promoted by the reproduced cell mixing. (A) Snapshots of spatial phase profiles emerging from random initial conditions in the phase oscillator model. The top row shows results without mixing ($v_0 = 0.14$), bottom row those with reproduced mixing ($v_0 = 1.39$) from tailbud in Fig. 2B. Snapshots during one oscillation cycle ($2\pi/\omega_0 = 40$ min) are shown, $t_1 = 213$ min. Color code indicates phase of oscillation. Scale bar = 10 μm . See Movies 3, 4. (B) Time evolution of phase order parameter Z from random initial phases in presence of reproduced mixing as in (A) (blue) and absence of mixing (red). (C) First passage time τ (vertical axis) of a given value of phase order parameter (horizontal axis) for data in (B). Inset: differences of first passage times $\Delta\tau$ divided by segmentation clock period (40 min; vertical axis, #somite) as a function of the phase order parameter Z . Error bars in (B) indicate standard deviations of Z over 200 realizations of simulations. $\kappa = 0.07 \text{ min}^{-1}$. All other parameter values in Eqns 4 and 5 listed in Tables S1-S3.

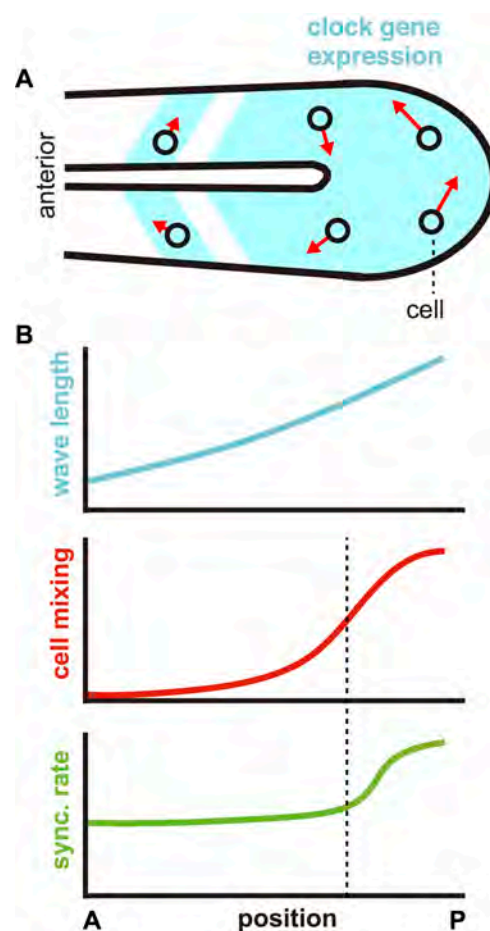


Fig 5. Robust somite boundary formation by cell mixing gradient. (A) Expression pattern of a segmentation clock gene in PSM and tailbud. The red arrows indicate cell velocity vectors and their lengths represent velocity modulus. (B) Spatial gradients of (top) wavelength of a gene expression pattern, (middle) cell mixing and (bottom) predicted synchronization (sync.) rate along the anterior-posterior axis of the PSM. Vertical broken line indicates the position where cell mixing can no longer affect synchronization of genetic oscillators. A: anterior. P: posterior

Supplementary Information

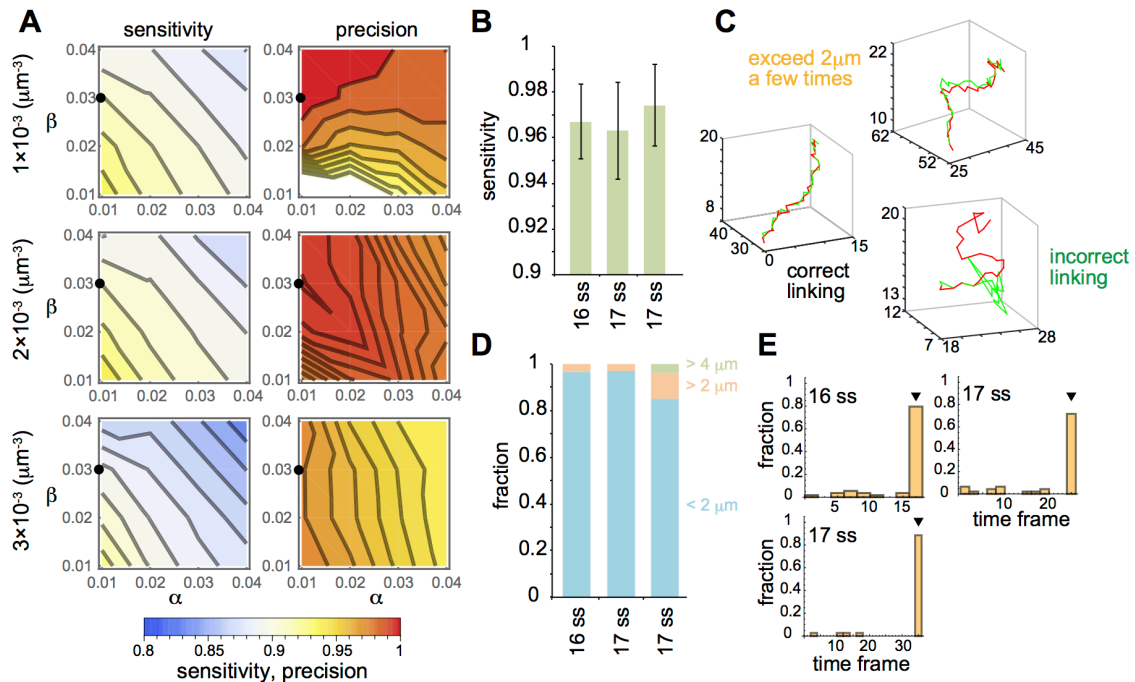


Figure S1 Validation of the tracking algorithm with synthetic images and three chimeric embryos. (A) Dependence of sensitivity and precision on the parameters α and β in the gradient vector diffusion algorithm for three different object densities. The filled circles represent the set of α and β used in the main text. (B) Sensitivity of the gradient vector diffusion algorithm in the three transplanted embryos. Averages and standard deviations over 10 time frames are shown. ss: somite stage. (C) Examples of cell trajectories. Each trajectory obtained in the dense (GFP) channel is classified into three categories depending on the distance from the corresponding trajectory in the sparse (mCherry) channel. The red lines represent cell trajectories in the sparse channel and the green lines represent the corresponding trajectories in the dense channel. (D) Fraction of three categories shown in (C). (E) Histograms of the trajectory length. Correctly linked trajectories ($< 2 \mu\text{m}$) were used in the histograms. Arrowheads indicate the last time frame of the time lapse movie. Values of parameters in the gradient vector diffusion algorithm are listed in Table S4.

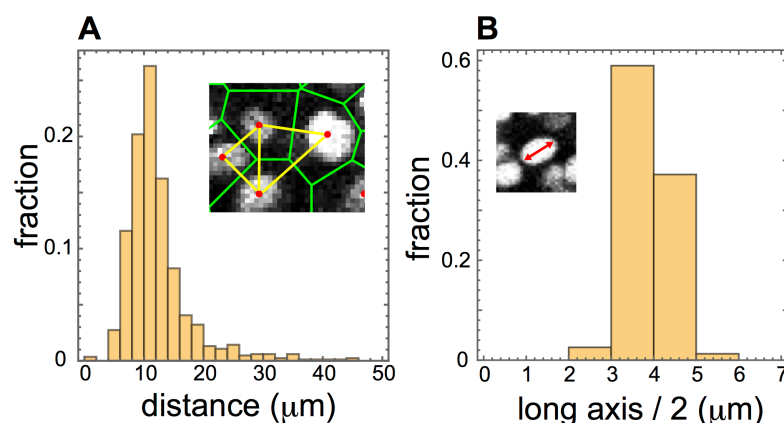


Figure S2 Estimation of cell size and quantification of nucleus size. (A) Histogram of the distances between two neighboring cells (yellow lines) for a 17 somite stage embryo. To determine neighboring relations the three-dimensional Voronoi tessellation (green lines) was used for the nuclear positions. Assuming that cells are close-packed, this procedure gives a good estimate for cell size. See supporting text for details. (B) Histogram of the half of the long axis of nucleus in the posterior PSM. Data from the four embryos was gathered to make the histogram.

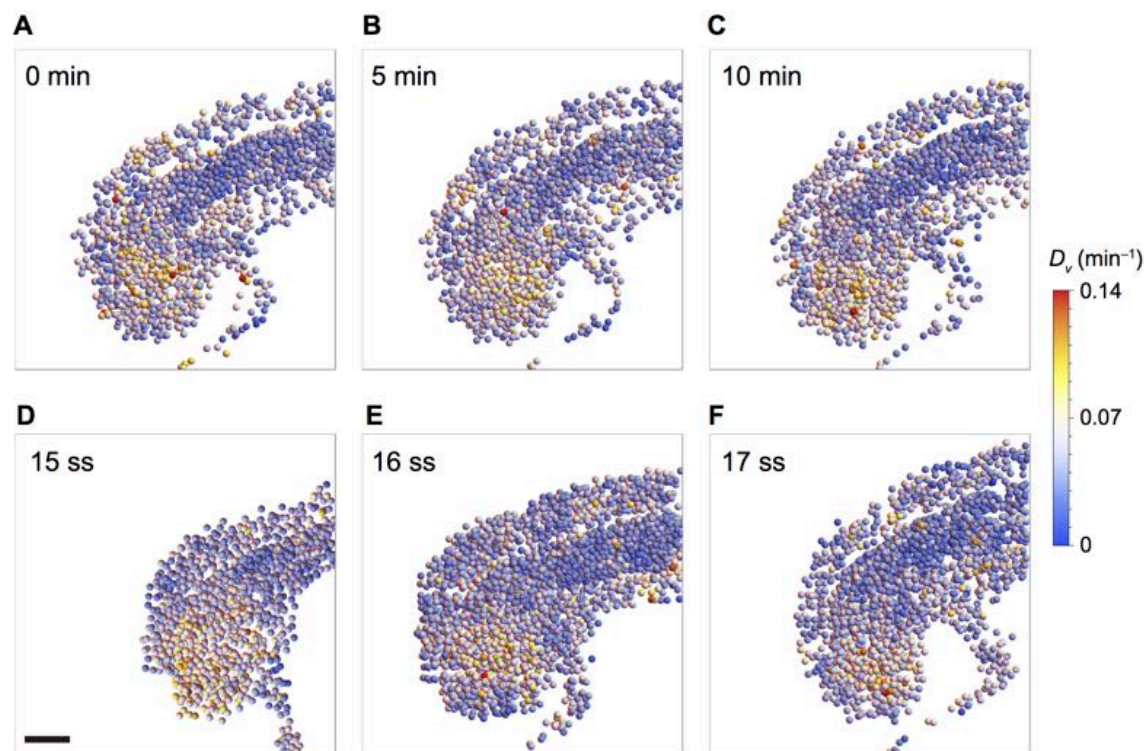


Figure S3 Average directional derivative modulus D_v for the 15-17 somite stage embryos. (A)-(C) Time series of D_v for the 17 somite stage (ss) embryo shown in Fig. 1 in the main text. (D)-(F) Spatial profiles of D_v for (D) 15 ss, (E) 16 ss and (F) 17 ss embryos. Scale bar = 50 μm.

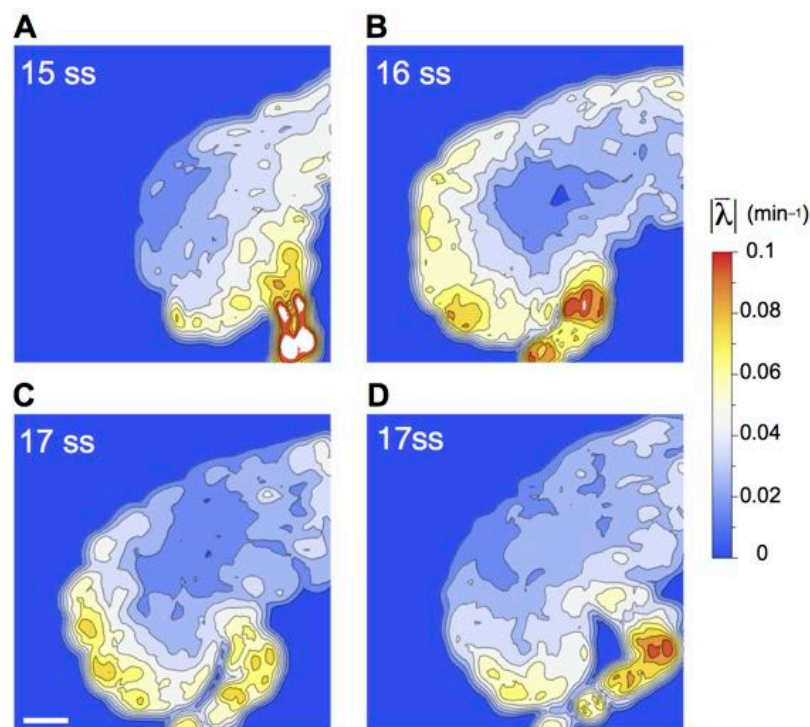


Figure S4 Quantification of cell mixing by the strain rate tensor. (A)-(D) Spatial profiles of the norm of eigenvalues $|\lambda|$ for (A) a 15 somite stage (ss), (B) a 16 ss, and (C), (D) 17 ss embryos. The maximum z -projection for the norm was applied. Eigenvalues of the strain rate tensor at each spatial position were computed after interpolating velocity vectors with the smoothed particle hydrodynamics (SPH). $h = 15 \mu\text{m}$ in the SPH. See supporting text for details. Scale bar = $50 \mu\text{m}$.

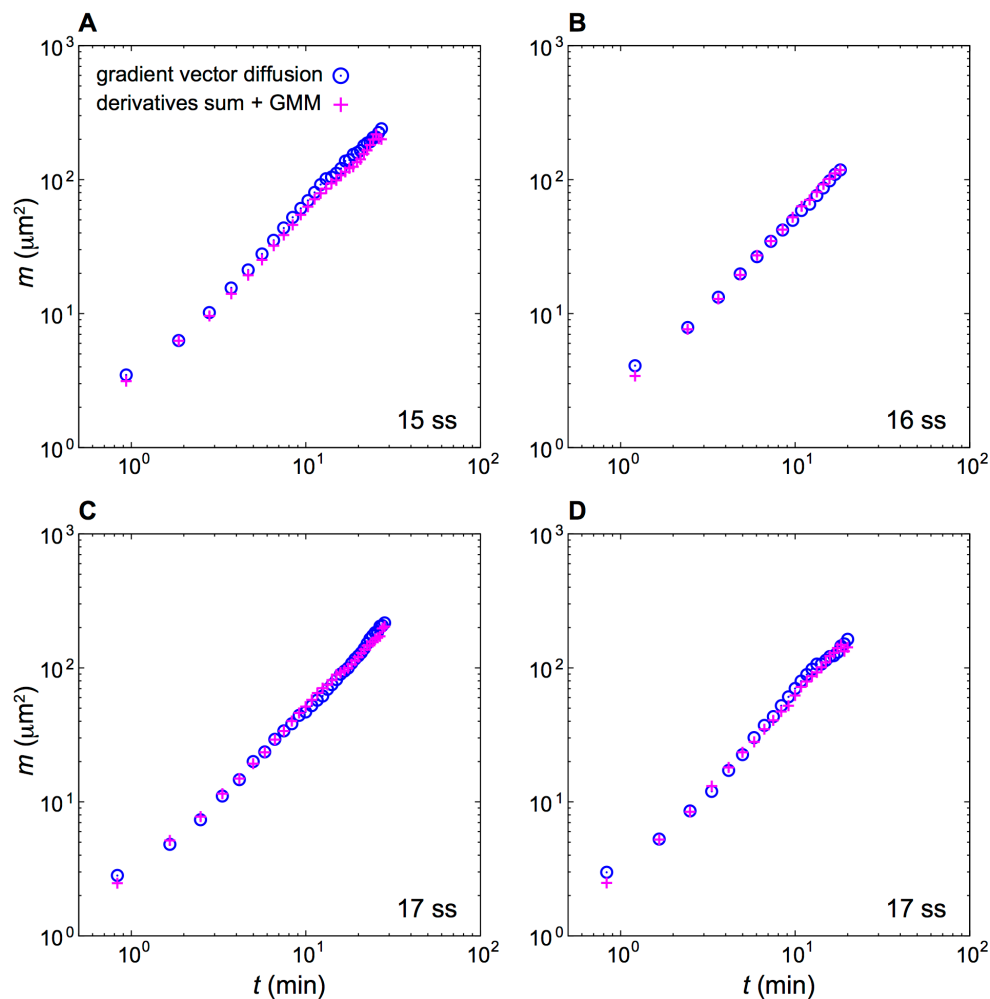


Figure S5 Comparison of the mean squared difference of displacement vectors (MSDD) obtained by two different nuclear detection algorithms. (A)-(D) MSDD for the tailbuds of (A) the 15 somite stage (ss), (B) 16 ss, and (C), (D) 17 ss embryos. Results obtained by the gradient vector diffusion algorithm (circles; main text) and by the derivatives sum (DS) nuclear segmentation algorithm (crosses; Bhavna et al., 2016) are shown for comparison. The DS algorithm is based on (Bhavna et al., 2016). Before applying the DS algorithm, the Gaussian noise filter and the isotropic nonlinear diffusion filter were used for noise reduction. Values of parameters in the DS algorithm were $\alpha = \beta = \gamma = \delta = 1$ and $\varepsilon = 2$. Gaussian Mixture Model was used as a post-processing method. The nearest neighbor linking algorithm was used after detecting the nuclear positions by these two nuclear detection algorithms.

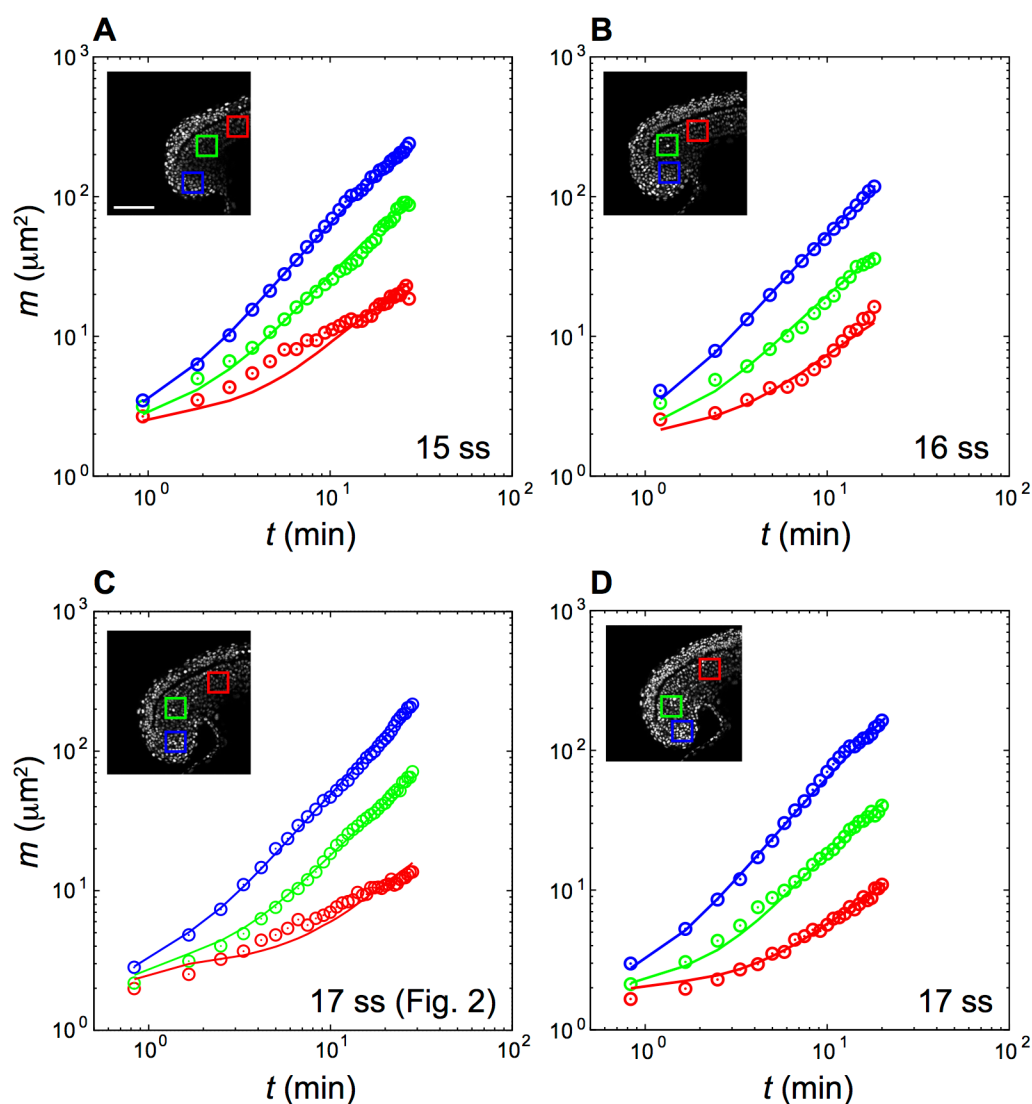


Figure S6 Quantification of cell mixing in the 15-17 somite stage zebrafish embryos by the mean squared difference of displacement vectors (MSDD). (A)-(D) Time evolution of the MSDDs for (A) 15 somite stage (ss), (B) 16 ss and (C),(D) 17 ss embryos. Circles represent experimental data. Lines are fitting by the physical model of cell movement to the experimental data. The colored boxes in the inset images indicate the regions for which the MSDD was calculated. The color code of the MSDD matches that of the boxes. The values of parameters in the model are listed in Tables S1 and S2. Scale bar = 100 μm in (A).

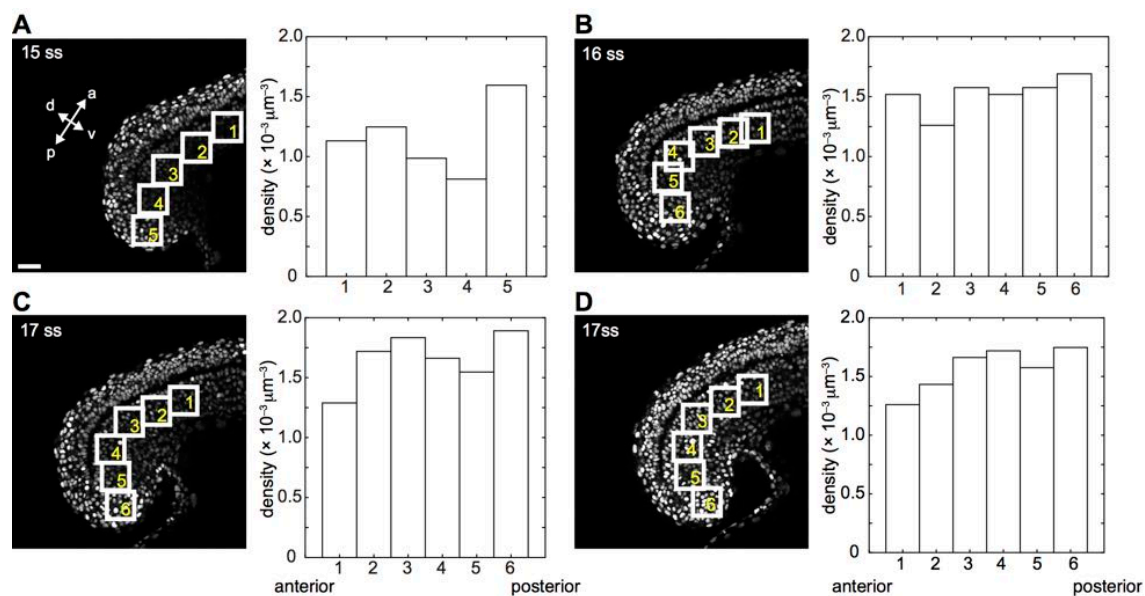


Figure S7 Nuclear density across the tailbud and PSM for the four embryos. (A)-(D) Snapshot image (left) and nuclear density (right) for (A) 15 somite stage (ss), (B) 16 ss and (C), (D) 17 ss embryos. Numbers in the six (five in (A)) white boxes correspond to those in the right bar charts. 1 (anterior most) to 6 (tailbud). Scale bar = 50 μm in (A).

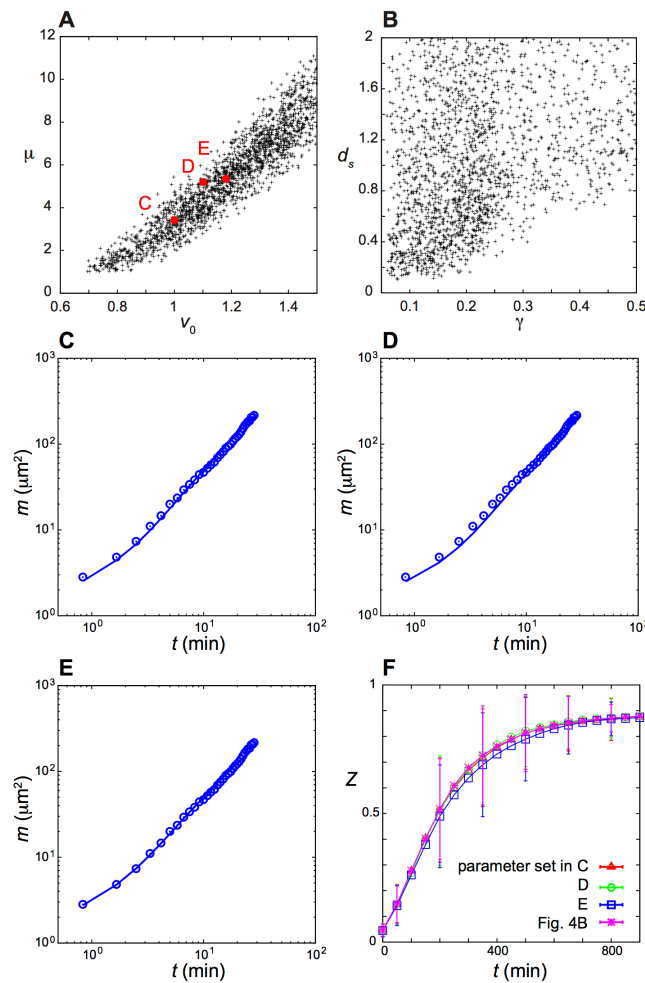


Figure S8 Different parameter sets that reproduced observed cell mixing in the tailbud. (A) Scatter plot of the values of the self-propulsion speed v_0 and the coefficient of repulsive force μ obtained by ABC MCMC sampling. The MSDD data for the tailbud of the 17 somite stage (ss) embryo shown in Fig. 2 were used in the ABC MCMC sampling. Three red points indicate the values used in (C)-(E). (B) Distance d_s in the ABC MCMC as a function of the length scale of nuclear confinement force γ in the physical model. A smaller value of d_s means a better fitting to the data. (C)-(E) Time evolution of the MSDD for the tailbud of the 17 ss embryo. Circles represent experimental data and the same data are plotted in (C)-(E). Lines are fitting by the physical model with three different parameter sets. These parameter sets are listed in Table S1 and the values of their v_0 and μ are plotted in (A) as the red circles. (F) Time evolution of the phase order parameter Z in the presence of reproduced cell mixing shown in the panels (C)-(E) and in Fig. 2 of the main text.

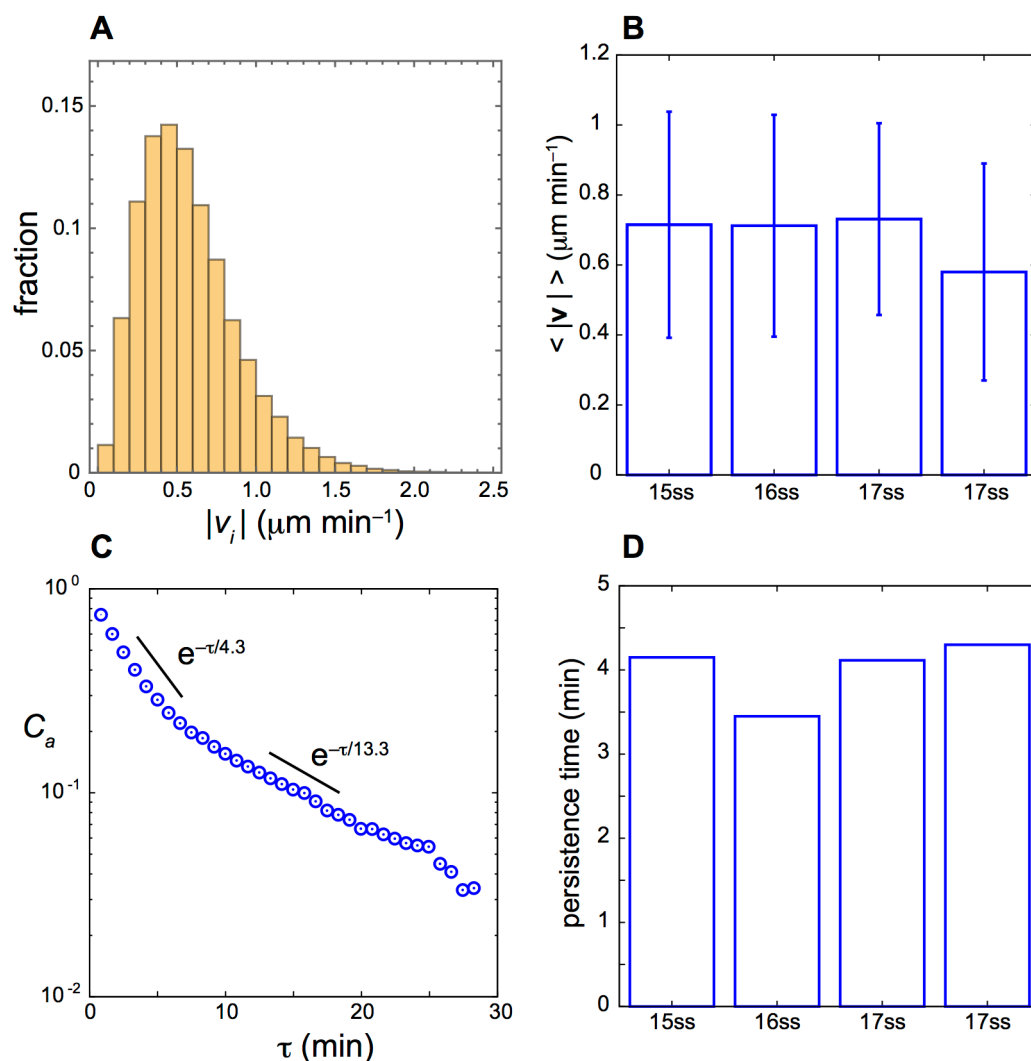


Figure S9 Estimation of cell velocity modulus and velocity auto-correlation in the embryonic tailbud from the fitted physical model. (A) Histogram of velocity modulus in a simulation of the physical model. (B) Average velocity modulus obtained by simulations of the fitted models for the tailbud of the four embryos. Error bars represent the standard deviations of the velocity modulus distribution in simulations. ss: somite stage. (C) Velocity auto-correlation for a single cell in the fitted model as a function of time τ . (D) Persistence time of velocity auto-correlation at a short timescale obtained by the fitted models for the tailbud of the four embryos. The values of parameters in the model are the ones that reproduced the mean squared difference of displacement vectors in the tailbuds of these embryos.

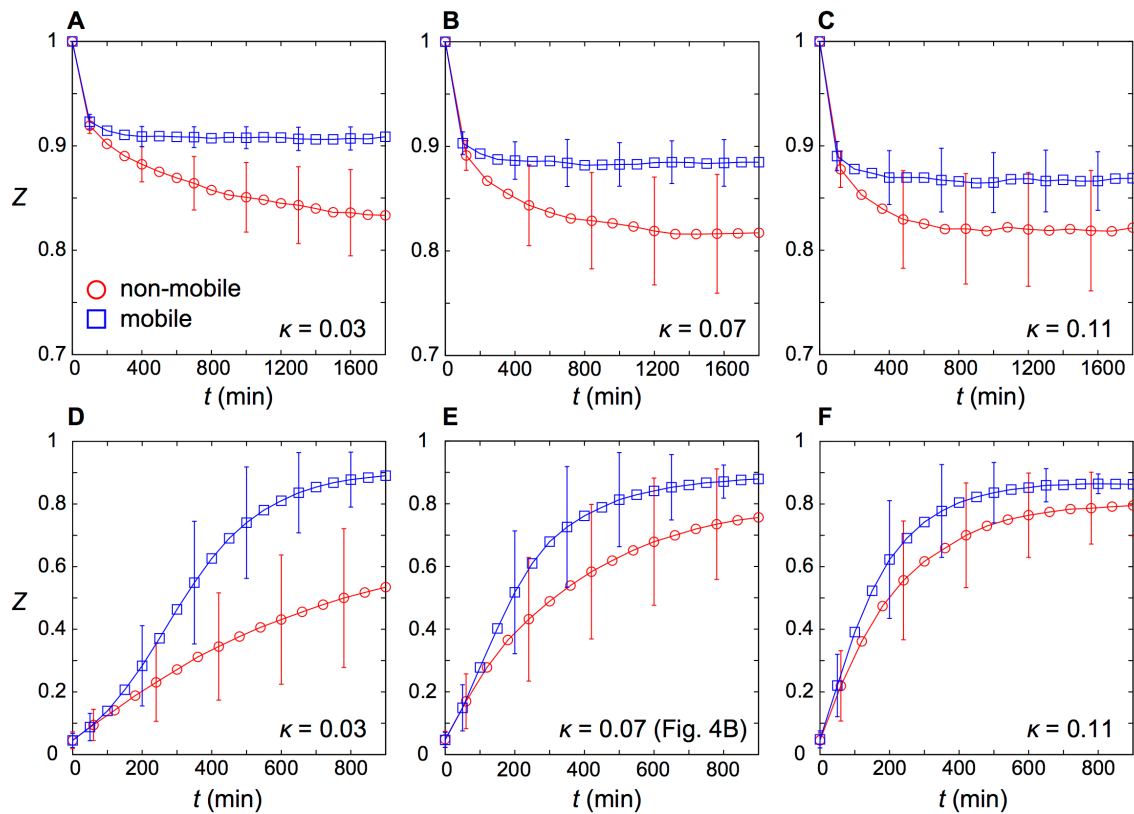


Figure S10 The influence of reproduced cell mixing on synchronization depends on the coupling strength κ . (A)-(C) Time evolution of the phase order parameter Z when simulations were started from a completely synchronized state ($Z(0) = 1$). (A) $\kappa = 0.03$, (B) 0.07 and (C) 0.11 min^{-1} . (D)-(F) Time evolution of the phase order parameter Z with (D) $\kappa = 0.03$, (E) 0.07 and (F) 0.11 min^{-1} . In (D)-(F), simulations were started from random phases. In all panels, blue squares are the results in the presence of reproduced mixing. Red circles are results for non-mobile cells for comparison. The standard deviation of frequency distribution σ_ω was scaled as $\kappa = \sigma_\omega/\omega_0$. Also, the phase noise intensity was scaled as $D_\theta/\kappa = 1/10$. Averages over 200 different realizations are plotted. The error bars represent the standard deviations of phase order parameter Z . Values of parameters are listed in Tables S1-S3.

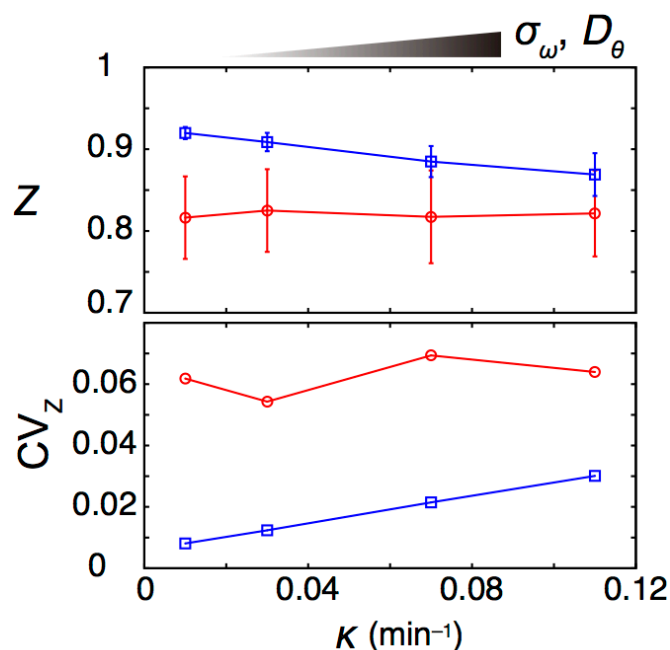


Figure S11 Reproduced cell mixing improves robustness of the synchronized state against phase noise. Top: steady state values of Z as a function of the coupling strength κ for the reproduced mixing (blue squares, $v_0 = 1.39$) and no movement (red circles, $v_0 = 0.14$). Bottom: Coefficient of variation of Z as a function of κ . Simulations were started from an initial condition where all the cells were completely synchronized ($Z(0) = 1$; Fig. S10A-C). Due to frequency noise, the phase order parameter Z decreased and reached a steady state value below 1 (Fig. S10A-C). The non-mobile oscillators' phase dispersion at steady state was fixed by adjusting κ and σ_ω , keeping the relation $\kappa = \sigma_\omega/\omega_0$ and $D_\theta/\kappa = 1/10$. Because of this scaling, the average phase order parameter Z for non-mobile oscillators at the steady state is almost constant even for different values of κ . Remarkably, Z for mobile oscillators was larger than that for non-mobile oscillators. Moreover, the coefficient of variation (CV) of the order parameter for mobile oscillators was smaller, indicating lower fluctuations in phase order. The difference between mobile and non-mobile oscillators was larger both in the average value of Z and CV when κ was small. Error bars indicate the standard deviations of Z over 200 realizations of simulations. The values of all other parameters are listed in Tables S1-S3.

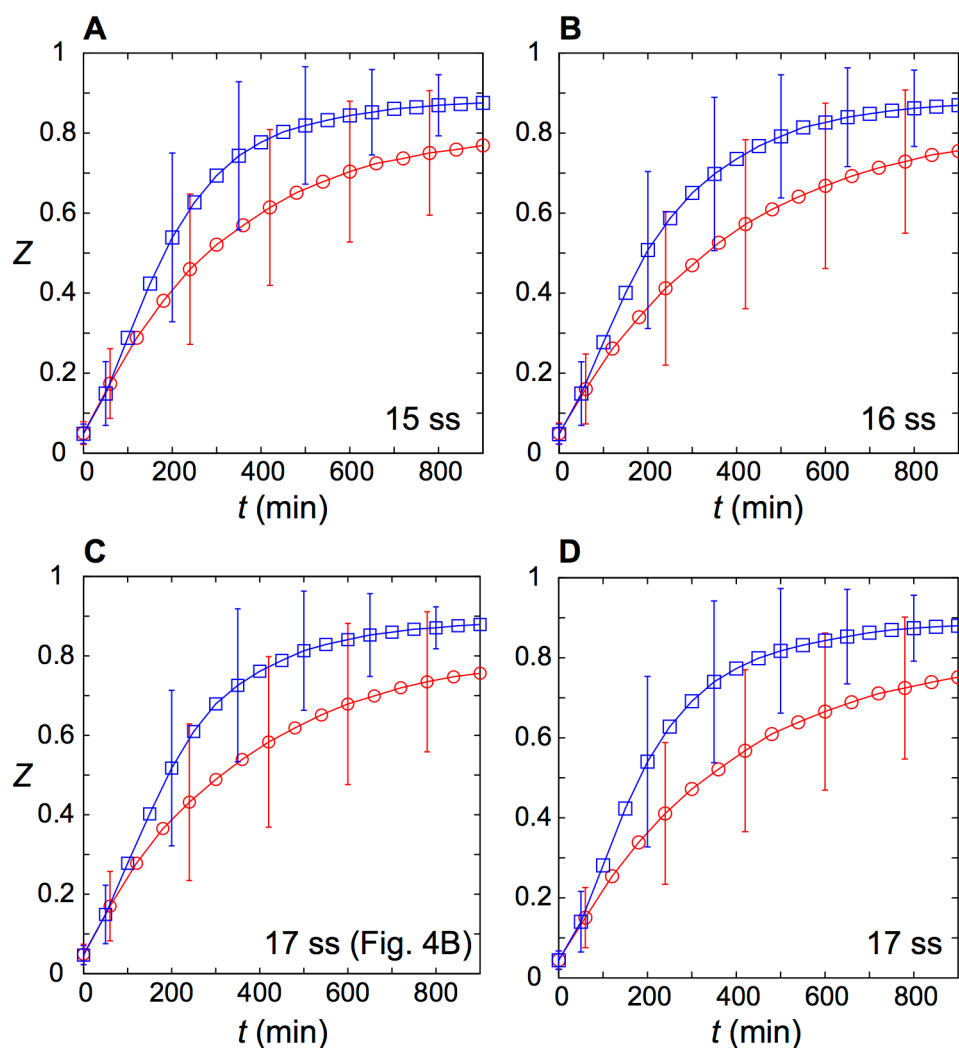


Figure S12 Reproduced cell mixing in the four embryos enhance synchronization of coupled phase oscillators. (A-D) Time evolution of the phase order parameter Z for the four embryos. These embryos correspond to those in Fig. S6. Cell mixing in the tailbud of each embryo was reproduced. Blue squares are the results in the presence of reproduced mixing. Red circles are results in the absence of cell mixing for comparison. Averages over 200 different realizations are plotted. The error bars represent the standard deviations. Values of parameters are listed in Tables S1-S3.

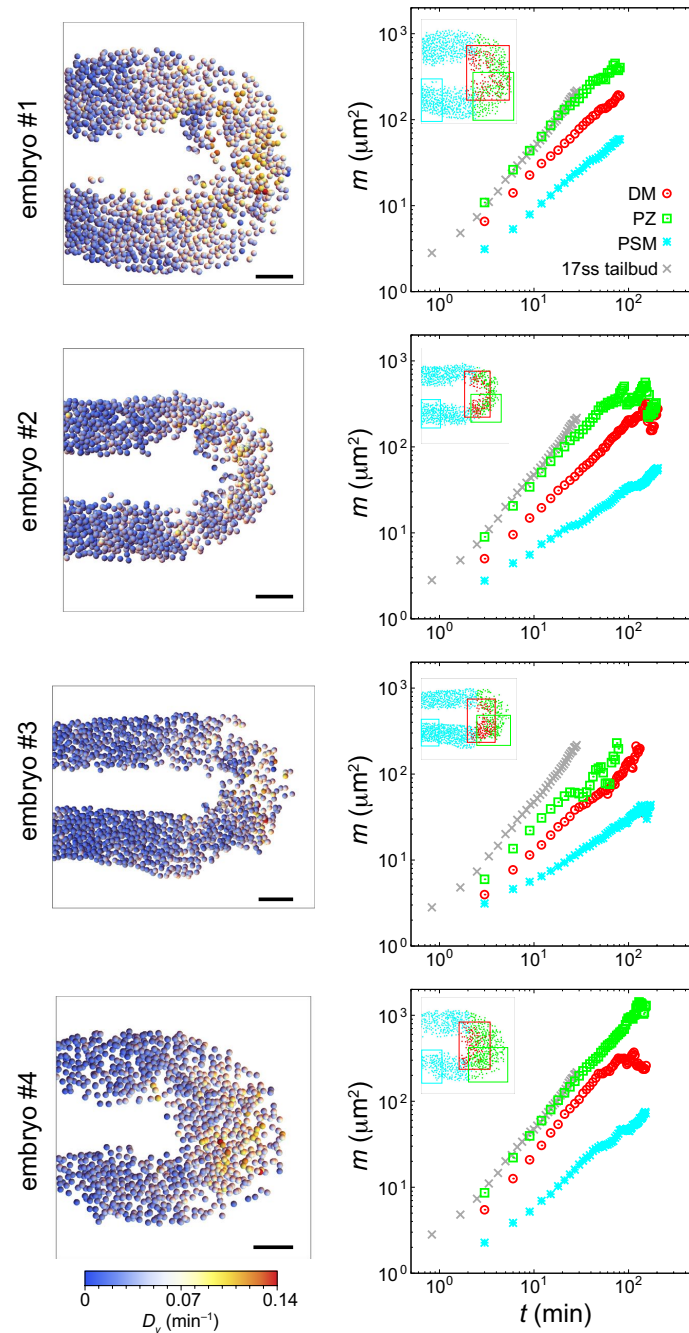


Figure S13 Cell mixing in the PSM and tailbud in 10 somite stage wild type zebrafish embryos growing at 18°C (Lawton data set). Left column: spatial profile of directional derivative modulus defined by Eqn 2 in the main text for four embryos. Cell trajectory data used for calculations is from Lawton et al., 2013 and was kindly provided by Scott Holley (Yale University). Dorsal view is shown. Anterior is left. Right column: time evolution of the mean squared difference of displacement vectors

(MSDD) for the dorsal medial (DM, the tailbud dorsal to the axial and paraxial mesoderm; red), progenitor zone (PZ, ventral to the dorsal medial zone and posterior to the notochord; green) and a PSM region (PSM; cyan). PZ corresponds to the region we refer to as tailbud in 15-17 somite stage (ss) embryos. For comparison, MSDD for cells in the tailbud in a 17 ss embryo is plotted (grey; Fig. 2). Inset figures indicate the tissue regions for which MSDD was calculated. Left halves of the PZ and PSM were used for the MSDD calculations to correspond to the lateral images analyzed in this study. The previous study (Lawton et al., 2013) reported that cells in the DM move more coherently (i.e. less relative movement) than those in the PZ. Consistent with this observation, the MSDD for the PZ increases faster than that for the DM. Scale bars = 50 μm in the left column.

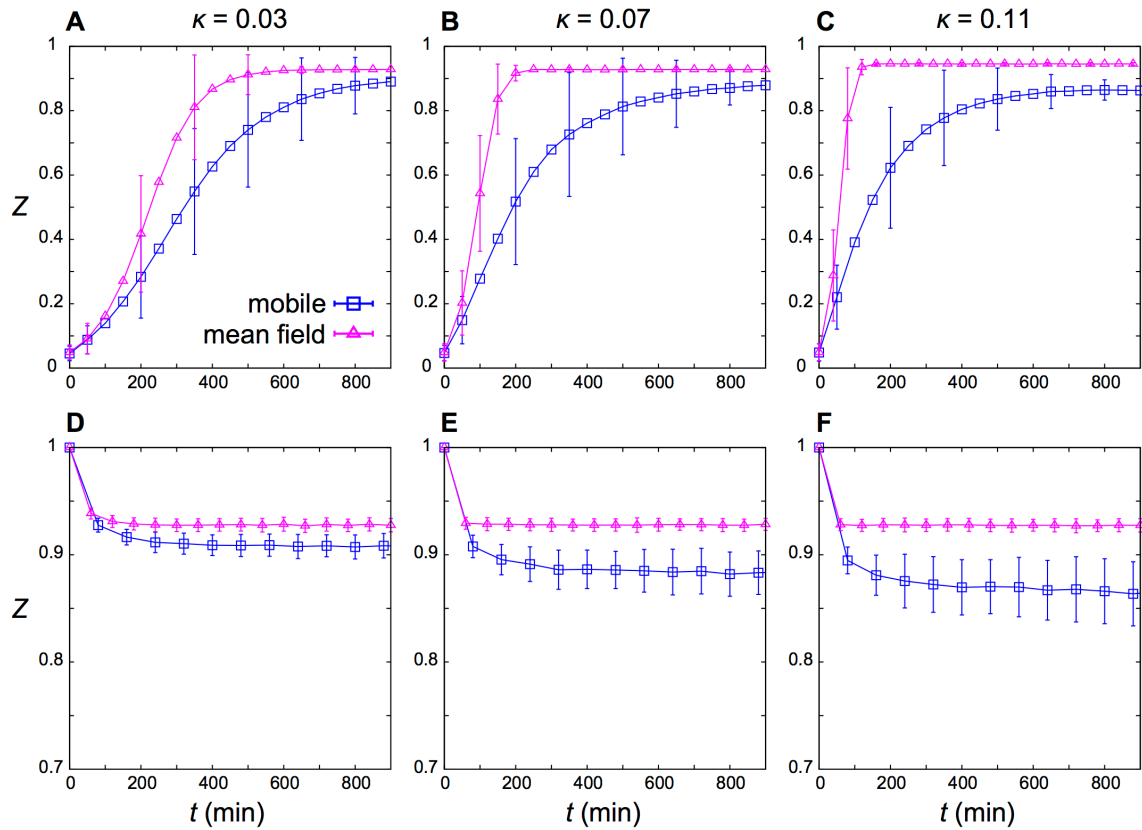


Figure S14 Comparison of synchronization dynamics between the mobile oscillator model Eqn 5 and a mean-field model Eqn S8.1. Time evolution of the phase order parameter Z from (A)-(C) random initial conditions and (D)-(F) the initial condition where all oscillators were completely synchronized ($Z(0) = 1$). (A),(D) $\kappa = 0.03$, (B),(E) 0.07 and (C),(F) 0.11 min^{-1} . For mobile oscillators, the parameter set for the tailbad in Fig. 2 in the main text was used. The number of oscillators in the simulations was same in the mobile oscillator and the mean-field models ($N = 346$). The standard deviation σ_ω for the frequency distribution was scaled as $\kappa = \sigma_\omega / \omega_0$ where ω_0 is the mean of the distribution. The noise intensity D_θ was also scaled as $D_\theta / \kappa = 1/10$. Average over 200 different realizations are plotted. The error bars indicate the standard deviations.

Table S1 Parameter values in the physical model of cell movement for the tailbuds.

	v_0	μ	D_ϕ	D_n	μ_b	γ	N
15ss (Figs. S6A and S12A)	1.27	4.91	0.06	0.303	25.7	0.09	330
16ss (Figs. S6B and S12B)	1.26	5.07	0.081	0.245	116.3	0.097	346
17ss (Figs. 2-4, and Figs. S9-S12, S14)	1.39	8.71	0.026	0.274	14	0.075	346
Fig. S8C	0.99	3.41	0.039	0.252	48	0.09	346
Fig. S8D	1.1	5.24	0.022	0.273	50.32	0.094	346
Fig. S8E	1.19	5.41	0.052	0.29	52	0.086	346
17ss (Figs. S6D and S12D)	1.35	5.68	0.052	0.33	73.1	0.115	389

See the supporting text for the definition of these parameters. The above values of v_0 are for simulations with mobile cells. For simulations with non-mobile cells in Figs. 4, S10, S11, and S12, the values of v_0 were reduced to 10% whereas all the other parameters were fixed as listed above. ss: somite-stage.

Table S2 Fixed parameter values in the physical model of cell movement.

Parameter	Definition (unit)	Value
L_x, L_y, L_z	domain length (μm)	60, 60, 60
d_c	cell diameter (μm)	11
ν	coefficient of boundary force ($\mu\text{m min}^{-1}$)	20
γ_b	lengthscale of boundary force (μm)	1
r_n	nuclear radius (μm)	3.8

These values are used in simulations throughout the article.

Table S3 Parameter values in the phase oscillator model.

	ω_0 (min^{-1})	σ_ω (min^{-1})	D_θ (min^{-1})	κ (min^{-1})	d_c (μm)
Fig. 4A-C	0.157	0.011	0.007	0.07	11
Figs. S8F and S12	0.157	0.011	0.007	0.07	11
Figs. S10, S11, S14	0.157	$\kappa \omega_0$	$\kappa/10$	0.01-0.11	11

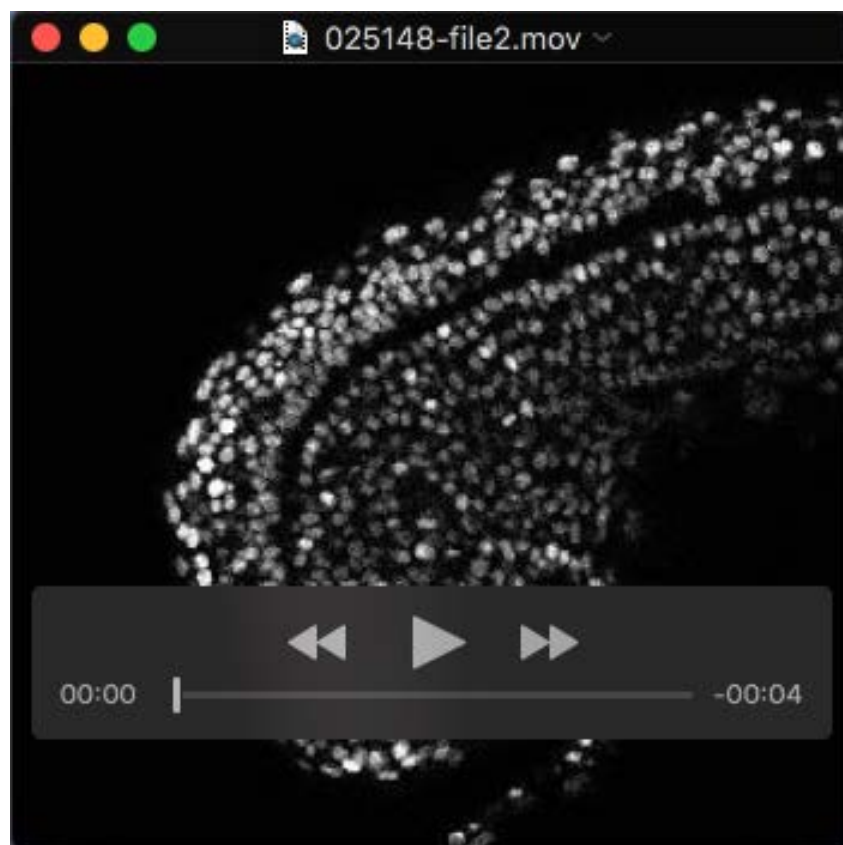
Table S4 Parameter values in the gradient vector diffusion algorithm.

Parameter	Value
α	0.01
β	0.03
F_T	18
R_s	6
q_0	0.01
σ	3

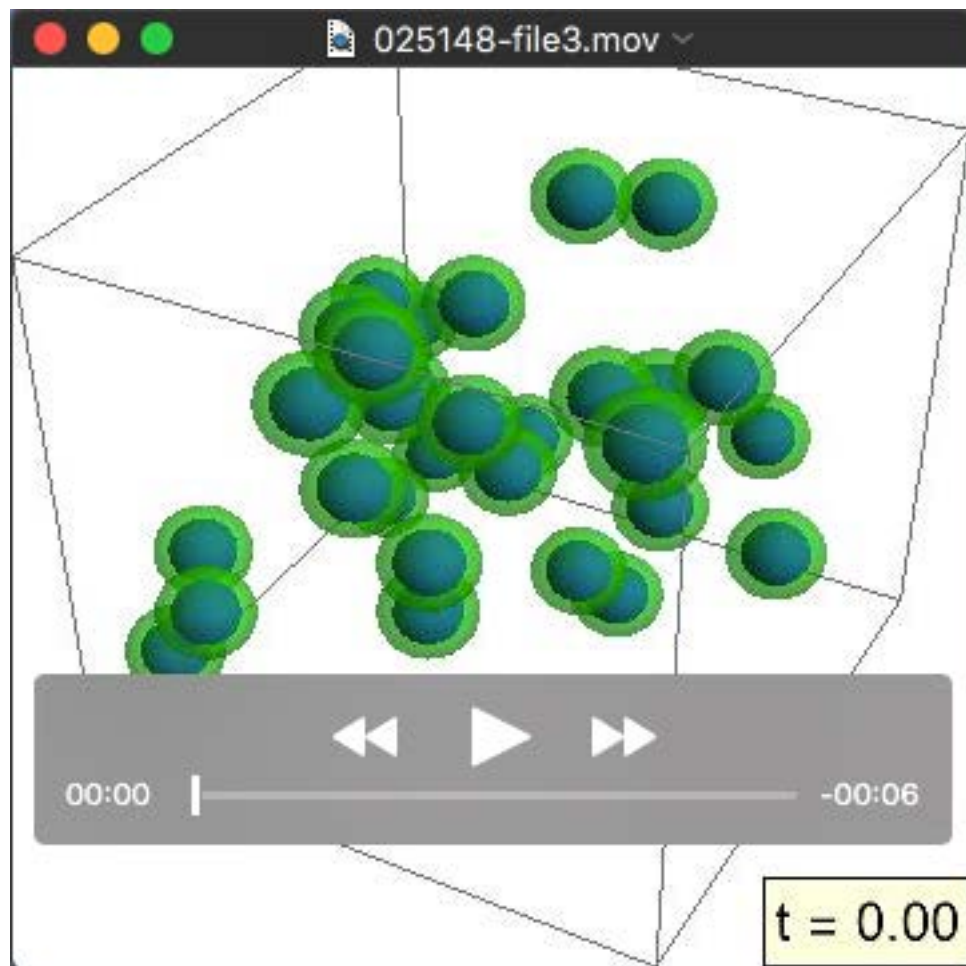
Table S5 Ranges of uniform distributions for each parameter in the prior distribution and the standard deviations of the Gaussians in the proposal distribution of parameters in ABC MCMC.

Parameter (unit)	min	max	σ_z
self-propulsion speed v_0 ($\mu\text{m}/\text{min}$)	0.1	1.5	0.07
coefficient of repulsive force μ ($\mu\text{m}/\text{min}$)	1	15	0.7
polarity noise strength D_ϕ (1/min)	0.01	0.1	0.0045
diffusion constant of the nucleus D_n ($\mu\text{m}^2/\text{min}$)	0.1	0.4	0.015
confinement force for the nucleus μ_b ($\mu\text{m}/\text{min}$)	10	120	5.5
lengthscale of the confinement force γ (μm)	0.06	0.5	0.0225

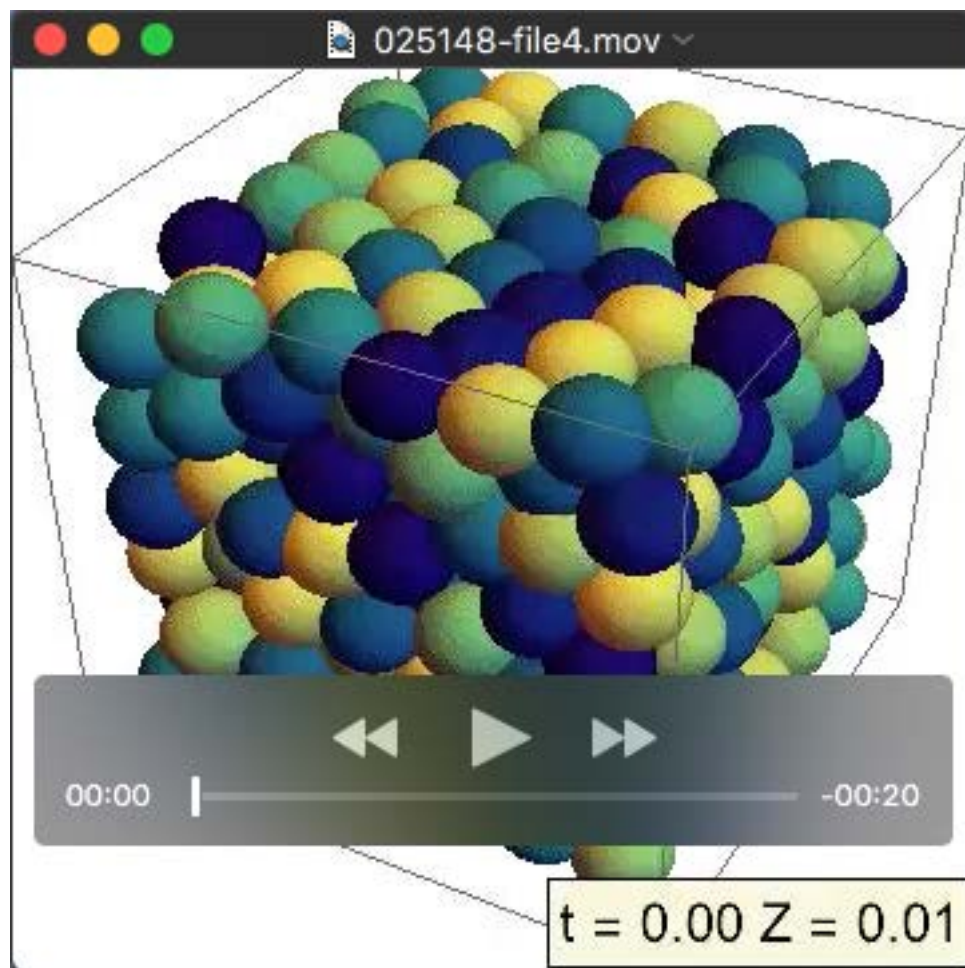
Movies



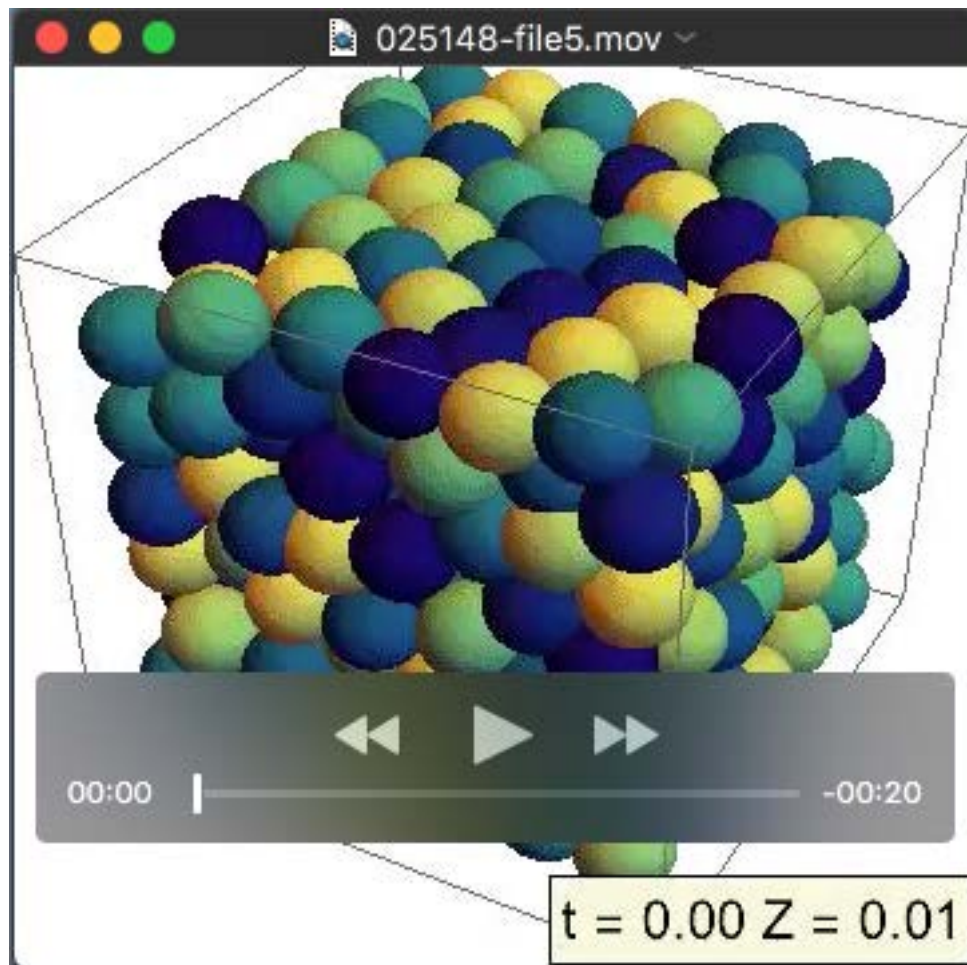
Movie 1 Time-lapse movie of the PSM and tailbud of the 17 somite stage embryo shown in Figs. 1 and 2. Slices of the stacks ($z = 18/24$) were used to make the Quick time movie file. The actual image size is $512 \times 512 \times 24$ voxels. The spatial resolution (voxel size) of the image is $0.692 \times 0.692 \times 1.75$ (μm^3). The frame interval is 0.83 min.



Movie 2 Simulation of the physical model of cell movement. Green color represents cell boundary and blue spheres represent cell nuclei. 30 cells out of 346 are plotted for visualization. A snapshot of this movie is shown in Fig. 3B. The unit of time (t) in the right bottom box is minutes.



Movie 3 Simulation of the coupled phase oscillator model in the absence of cell mixing $v_0 = 0.14$ ($\mu\text{m min}^{-1}$). The spheres represent cells and color code indicates the phase value for each cell. The unit of time (t) in the right bottom box is minutes. The variable Z indicates the phase order parameter defined by Eqn 6. In Movies 3 and 4, we started simulations from the same initial conditions for illustration.



Movie 4 Simulation of the coupled phase oscillator model in the presence of reproduced cell mixing $\nu_0 = 1.39 \text{ (}\mu\text{m min}^{-1}\text{)}$. The spheres represent cells and color code indicates the phase value for each cell. The unit of time (t) in the right bottom box is minutes. The variable Z indicates the phase order parameter defined by Eqn 6. The simulation was started from the same initial condition used in Movie 3.

Supporting Text

S1. Nucleus detection and cell tracking algorithm

To determine the positions of cell nuclei in an embryonic image, we used the gradient vector diffusion algorithm proposed by Li et al. (Li et al., 2007). The algorithm determines the positions of the center of each nucleus using the spatial intensity gradient in the image.

The basic idea of the gradient vector diffusion method is as follows. Since we stain cellular nuclei, there are spatial intensity gradient vectors pointing toward the center of each nucleus in an embryonic image. Sink points of the vector flows should, therefore, indicate the center of nuclei. However, due to noise in the image, original intensity gradient vectors often point in different directions from the centers of nuclei. The gradient vector diffusion method uses a partial differential equation to smooth and correct the direction of the intensity gradient vectors.

We briefly describe the algorithm. Let $I(\mathbf{x})$ be the intensity of an embryonic image at voxel position \mathbf{x} . We convolved a two-dimensional Gaussian $G_\sigma(\mathbf{x})$ with a standard deviation σ to each slice of a three-dimensional image stack $I(\mathbf{x})$ and obtained:

$$I_G(\mathbf{x}) \equiv G_\sigma(\mathbf{x}) * I(\mathbf{x}), \quad (\text{S1.1})$$

where the symbol $*$ indicates convolution. We computed the spatial gradient vector of the signal intensity $\nabla I_G(\mathbf{x})$ and defined a vector field:

$$\mathbf{u}(\mathbf{x}, 0) = \nabla I_G(\mathbf{x}), \quad (\text{S1.2})$$

where $\mathbf{u}(\mathbf{x}, 0)$ is the intensity gradient vector at integration time $\tau = 0$, that is the intensity gradient vector in the original embryonic image. Then we evolved the intensity gradient vector according to the following partial differential equation:

$$\frac{\partial \mathbf{u}(\mathbf{x}, \tau)}{\partial \tau} = \alpha \nabla^2 \mathbf{u} + (\alpha + \beta) \nabla \text{div}(\mathbf{u}) + q_v(\mathbf{x}) \{ \nabla I_G - \mathbf{u} \}, \quad (\text{S1.3})$$

where α and β are parameters. The function $q_v(\mathbf{x})$ was defined as in (Li et al., 2007):

$$q_v(\mathbf{x}) = \begin{cases} q_0, & |\nabla I_G(\mathbf{x})| > 0 \\ 0, & \text{otherwise.} \end{cases} \quad (\text{S1.4})$$

We used a reflecting boundary condition in numerical integrations of Eqn S1.3. The

partial differential equation Eqn S1.3 was discretized in space and time, and integrated with an explicit scheme as in (Li et al., 2007). We integrated the equation for 50 steps. The values of each parameter in the equation are listed in Table S4. Our embryonic images had anisotropic voxels where z resolution ($1.75 \mu\text{m}$) was lower than x and y resolution ($0.692 \mu\text{m}$). Since anisotropic voxels were not appropriate for the algorithm, we applied the third-order spline interpolation in z direction to obtain isotropic voxels as proposed in (Li et al., 2007) before solving Eqn S1.3.

To determine nuclear positions from the vector field $\mathbf{u}(\mathbf{x})$ after integration, we detected sink points of the vector flows by extending the algorithm in (Li et al., 2007) into three-dimensional space. We first normalized $\mathbf{u}(\mathbf{x})$ at each spatial point to obtain a unit vector field:

$$\tilde{\mathbf{u}}(\mathbf{x}) \equiv \mathbf{u}(\mathbf{x}) / \|\mathbf{u}(\mathbf{x})\|. \quad (\text{S1.5})$$

Then, we measured an outward flux from the position \mathbf{x} by:

$$Flux(\mathbf{x}) = \sum_{i=1}^{26} \mathbf{N}_i \cdot \tilde{\mathbf{u}}(\mathbf{x}_i), \quad (\text{S1.6})$$

where \mathbf{x}_i is the position of the neighboring voxels of \mathbf{x} and \mathbf{N}_i is the outward normal vector at position \mathbf{x}_i on a sphere centered at \mathbf{x} . The number of neighboring voxels in the bulk is 26. Note that $Flux(\mathbf{x}) < 0$ at the sink points. Then, we introduced a threshold F_T and if

$$-Flux(\mathbf{x}) \geq F_T > 0, \quad (\text{S1.7})$$

we considered \mathbf{x} as a sink point. If we found two spatial points that satisfied Eqn S1.7 and whose spatial distance was less than a threshold R_s , we chose the one that had the larger value of $|Flux(\mathbf{x})|$ as a sink point.

Cell tracking. For cell tracking we applied a trajectory linking algorithm (Sbalzarini and Koumoutsakos, 2005). Briefly, let \mathbf{p}_i be the position of a detected nucleus at time frame t ($i = 1, 2, \dots, N_t$). Let \mathbf{q}_j be the position of a detected nucleus at time frame $t+1$ ($j = 1, 2, \dots, N_{t+1}$). The algorithm defines an association matrix of the size $(N_t + 1) \times (N_{t+1} + 1)$:

$$G^t(i, j) = g_{ij} \equiv \begin{cases} 1 & \text{if } \mathbf{p}_i \text{ at } t \text{ and } \mathbf{q}_j \text{ at } t+1 \text{ are the same nucleus,} \\ 0 & \text{otherwise.} \end{cases} \quad (\text{S1.8})$$

g_{i0} are for nuclei that are present at the frame t and disappear at the frame $t+1$. g_{0j} are for nuclei that newly appear at the frame $t+1$.

To determine the values of elements g_{ij} , the algorithm defines the cost functional:

$$\Phi = \sum_{i=0}^{N_t} \sum_{j=0}^{N_{t+1}} \psi_{ij} g_{ij}, \quad (\text{S1.9})$$

where we set

$$\psi_{ij} = \left(x_{p_i} - x_{q_j}\right)^2 + \left(y_{p_i} - y_{q_j}\right)^2 + \left(z_{p_i} - z_{q_j}\right)^2, \quad (\text{S1.10})$$

which is the squared distance between the nuclear positions \mathbf{p}_i and \mathbf{q}_j for $i, j > 0$. Hence, minimizing Φ with respect to g_{ij} means nearest neighbor linking between a point at t and a point at the next frame $t+1$. If we could not find any nuclei at time frame $t+1$ within a sphere with radius $4 \mu\text{m}$ centered at \mathbf{p}_i , we considered that we lost the nucleus at $t+1$ and set $g_{i0} = 1$ and $\psi_{i0} = 4^2$. Similarly, if we could not find any nuclei at time t within a sphere with radius $4 \mu\text{m}$ centered at \mathbf{q}_j , we considered that the nucleus newly appears at $t+1$ and set $g_{0j} = 1$ and $\psi_{0j} = 4^2$. By minimizing Φ with respect to g_{ij} we linked the nuclei at time frame t to those at $t+1$. For minimization we used the optimization algorithm proposed in (Sbalzarini and Koumoutsakos, 2005).

S2. Validation of nucleus detection and cell tracking

In this section we first calibrate the parameters in the gradient vector diffusion algorithm with synthetic images and then verify tracking accuracy using transplanted embryos (Bhavna et al., 2016).

Calibration with synthetic images. The gradient vector diffusion algorithm Eqn S1.3 includes three key parameters, α , β and q_0 . We calibrated these parameters using synthetic images that have similar properties to the embryonic images such as the average size of nucleus, its density and intensity fluctuations within a nucleus. See the reference (Bhavna et al., 2016) for generation of synthetic images. In the following analysis we fixed $q_0 = 0.01$ in Eqn S1.4 and changed the values of α and β . Values of the other parameters were also fixed and they are listed in Table S4.

For parameter calibration, we defined sensitivity and precision (Bhavna et al., 2016). Sensitivity was defined as the ratio of the number of correctly detected objects by the algorithm to the true number of objects in a synthetic image. Precision was defined as the ratio of the number of correctly detected objects to the total number of detected objects. For matching the positions of detected objects and those of ground truth data set, we applied the particle matching algorithm used in cell tracking as described in the previous section.

Fig. S1A shows the dependence of sensitivity and precision on the parameters α and β in Eqn S1.3. For each object density shown in Fig. S1A, we generated five different synthetic images ($100 \times 100 \times 25$ voxels; $69.2 \times 69.2 \times 43.75 \mu\text{m}^3$) where the spatial configuration of objects was different. The signal-to-noise ratio (SNR) in the synthetic images was fixed as $\text{SNR} = 5$. We computed average sensitivity and precision over these five images in Fig. S1A. Sensitivity was higher when values of both α and β were smaller (Fig. S1A). As the values of these two parameters increased, sensitivity decreased. In contrast, when both α and β were small, the precision became small especially in the low object density (Fig. S1A). Precision was high when α was small while β was large. A higher precision would be more important than a higher sensitivity to avoid artifacts in cell tracking. Therefore, we concluded that combination of a smaller α and a larger β gave a good combination of sensitivity and precision. In the main text and the following analysis, we fixed $\alpha = 0.01$ and $\beta = 0.03$ (filled circles in Fig. S1A). With this parameter set, sensitivity was about 0.9 and precision was 0.98 over the relevant object density (from 1×10^{-3} to $3 \times 10^{-3} \mu\text{m}^{-3}$; Fig. S1A) in the synthetic images.

Validation with transplanted embryos. To validate the algorithm in living tissues we used transplanted chimeric embryos as previously proposed in (Bhavna et al., 2016). A few cells carrying both mCherry-tagged and GFP-tagged Histones as nuclear labels were transplanted at blastula stage to host embryos carrying only GFP-tagged Histones. Detecting these transplanted cells is easier in the mCherry channel (sparse channel) because the density of these transplanted cells was low, while detecting them in the GFP channel (dense channel) was more difficult. Thus, the results for the sparse channel can be considered as a ground truth data set. By comparing the detected positions of the

transplanted cells in the two channels, we evaluate the sensitivity of the algorithm in living embryos. See (Bhavna et al., 2016) for more details.

We had four chimeric embryos (one embryo at 15 somite stage (ss), one embryo at 16 ss and two embryos at 17 ss). In the 15 ss embryo, the transplanted cells in the PSM were almost absent, so we used the other three embryos for the validation of gradient vector diffusion and tracking algorithms. We set a three-dimensional box of the size $70 \times 70 \times z$ μm^3 ($z = 61$ for the 16 ss embryo and $z = 42$ for the two 17 ss embryos) in the posterior PSM and validated the algorithms using the nuclei in the box. For the nuclear detection in the sparse channel we used $\alpha = 0.01$ and $\beta = 0.04$ to attain better precision at a lower nuclear density (Fig. S1A).

If the algorithm detected a nucleus in the dense channel within a distance of $2 \mu\text{m}$ from a nucleus in the sparse channel, we considered that the algorithm could detect the transplanted cell in the dense channel correctly. We defined sensitivity as the ratio of the number of detected transplanted nuclei in the dense channel to the total number of transplanted nuclei in the sparse channel within the box. The algorithm could detect transplanted cells in the dense channel with sensitivity of 0.97 on average (Fig. S1B). We also confirmed that the dependence of sensitivity on the parameters α and β in Eqn S1.3 for the transplanted embryos was similar to that observed for the synthetic images shown in Fig. S1A.

Subsequently, we tested the accuracy of trajectory linking using the transplanted embryos (Fig. S1C-E). We first obtained full-length trajectories of transplanted cells in the sparse channel and considered them as the ground truth data set (the red trajectories in Fig. S1C). Then, we compared the corresponding trajectories in the dense channel (the green trajectories in Fig. S1C). A similar validation was used in a previous study (Lawton et al., 2013).

We classified trajectories into three categories: 1) the distance between the trajectories in the dense and sparse channels is less than $2 \mu\text{m}$ at all time frames, 2) the distance is larger than $2 \mu\text{m}$ but less than $4 \mu\text{m}$, and 3) the distance is larger than $4 \mu\text{m}$ (Fig. S1C). Trajectories in the third category were obviously caused by incorrect linking (Fig. S1C).

However, the fraction of this third category was very small (Fig. S1D). Occasionally, the tracking algorithm lost cells in the middle of the movie in the dense channel, perhaps due to under-segmentation. However, these shorter trajectories would not cause any artifacts in movement statistics in later analysis. Hence, we included these shorter trajectories into one of above three categories depending on the distances from sparse ones. When we obtained full-length trajectories in the sparse channel, about 80% of them were obtained as full-length trajectories in the dense channel as well (Fig. S1E).

S3. Quantification of tissue parameters

To constrain the values of parameters in the physical model for cell movement in the main text we measured key tissue parameters. We first measured the nuclear density across the PSM using the nuclear position data. We set boxes of the size $42 \times 42 \times 20 \mu\text{m}^3$ in different regions across the PSM (white boxes in the left panels of Fig. S7) and counted the number of nuclei within each box. To fill the entire region of each box with cells the boxes were located $20 \mu\text{m}$ inside the PSM, away from the epidermal tissue. The nuclear density was defined as the number of nuclei in a unit volume $1 \mu\text{m}^3$. Fig. S7 shows the spatial distribution of the nuclear density across the PSM of the four embryos. The nuclear density changed nonmonotonically along the anterior-posterior axis of the PSM. The density was slightly lower at the most anterior region where the next somite would be formed. The density increased toward the posterior PSM but it decreased again near the boundary between the PSM and tailbud. The tailbud had a higher nuclear density. These tendencies could consistently be observed in all four embryos examined at the similar developmental stage (Fig. S7). The average nuclear density over the four embryos in the tailbud in Figs. 2 and S6 was $1.61 \times 10^{-3} \pm 8.63 \times 10^{-5} \mu\text{m}^{-3}$.

To check the statistical significance of the observed variation of nuclear density, we applied the one-tailed t-test between the most anterior region (box 1) and the tailbud region (box 5 of the 15 ss embryo in A and box 6 of the other three embryos) in Fig. S7. We pooled data for the four embryos by assuming that these data are samples from the same population. We observed statistical significance of nuclear density difference between these two regions at $p < 0.01$. However, a more careful experimental setting would be required to further investigate distribution of nuclear density at a higher spatial resolution, which is out of the scope of the current study.

Next we estimated the size of cells in the tailbud (Fig. S2A). We interpreted the distance between two neighboring nuclei as a characteristic size of cells. To define a neighboring relation for cells from nuclear positions, we applied the three dimensional Voronoi tessellation to the nuclear position data. We measured the distance between a pair of nuclei that are neighbors in a 3D Voronoi diagram. The histogram of the distances had a clear peak (Fig. S2A). Its median was about 11.2 μm for cells in the tailbud, which we considered as a typical diameter of cells. We obtained similar median values for all four embryos. We also applied this method to the cells in anterior regions of the PSM. The average value of the median of distance distribution over the four embryos was slightly larger ($\sim 11.8 \mu\text{m}$) in anterior region, but we could not detect significant difference by t-test between the anterior and posterior PSM.

We also measured the length of the long axis of nuclei (Fig. S2B). We determined the long axis of a nucleus in the sparse channel within an x - y plane after visually scanning through the z direction (Fig. S2B). The average half-length of the long axis of 78 nuclei in the posterior PSM was $3.83 \pm 0.51 \mu\text{m}$.

S4. Quantification of relative cell movement by the strain rate tensor

In the main text we used directional derivative of velocity vectors to quantify relative cell movement. Another approach would be to use the strain rate tensor after constructing a cell flow field. We computed the strain rate tensor to quantify relative cell movement in the PSM and tailbud. Here we first note the reason why we chose to use the strain rate tensor. Then, we describe results of the strain rate tensor for the embryonic tissues.

From cell tracking we obtained cellular velocities in the PSM and tailbud. Using the velocity data we constructed a continuum velocity vector field with the smoothed particle hydrodynamics (SPH) (Liu et al., 2003) described in the next section. Then, we examined the resulting flow field using methods from fluid mechanics.

In this section we denote $\mathbf{x} = (x, y, z) = (x_1, x_2, x_3)$ for notational simplicity. Let us

consider two tracer points at position \mathbf{x} and $\mathbf{x} + \Delta\mathbf{x}$ ($|\Delta\mathbf{x}| \ll 1$) in a velocity vector field. Their velocities are denoted as $\mathbf{v}(\mathbf{x})$ and $\mathbf{v}(\mathbf{x} + \Delta\mathbf{x})$, respectively. The relative positional vector between them is $\Delta\mathbf{x}$. After short time Δt , their positions change as $\mathbf{x} + \mathbf{v}(\mathbf{x})\Delta t$ and $\mathbf{x} + \Delta\mathbf{x} + \mathbf{v}(\mathbf{x} + \Delta\mathbf{x})\Delta t$. Then, a relative positional vector $\Delta\mathbf{x}'$ between these two points is:

$$\begin{aligned}\Delta\mathbf{x}' &= \mathbf{x} + \Delta\mathbf{x} + \mathbf{v}(\mathbf{x} + \Delta\mathbf{x})\Delta t - \{\mathbf{x} + \mathbf{v}(\mathbf{x})\Delta t\} \\ &= \Delta\mathbf{x} + \{\mathbf{v}(\mathbf{x} + \Delta\mathbf{x}) - \mathbf{v}(\mathbf{x})\}\Delta t \\ &\approx \Delta\mathbf{x} + (\partial\mathbf{v}(\mathbf{x})/\partial\mathbf{x})\Delta\mathbf{x}\Delta t,\end{aligned}\tag{S4.1}$$

where we expanded $\mathbf{v}(\mathbf{x} + \Delta\mathbf{x})$ and neglected the higher order terms in the second line as:

$$\mathbf{v}(\mathbf{x} + \Delta\mathbf{x}) \approx \mathbf{v}(\mathbf{x}) + (\partial\mathbf{v}(\mathbf{x})/\partial\mathbf{x})\Delta\mathbf{x}.\tag{S4.2}$$

The matrix $(\partial\mathbf{v}(\mathbf{x})/\partial\mathbf{x})_{ij} = \partial v_i(\mathbf{x})/\partial x_j$ is called the velocity gradient tensor. Then, we

separate the velocity gradient tensor into the symmetric and anti-symmetric parts:

$$\partial\mathbf{v}(\mathbf{x})/\partial\mathbf{x} = \mathbf{S}(\mathbf{x}) + \mathbf{A}(\mathbf{x}),\tag{S4.3}$$

where $S_{ij} = \frac{1}{2}\left(\frac{\partial v_i}{\partial x_j} + \frac{\partial v_j}{\partial x_i}\right)$ and $A_{ij} = \frac{1}{2}\left(\frac{\partial v_i}{\partial x_j} - \frac{\partial v_j}{\partial x_i}\right)$. The symmetric tensor \mathbf{S} is called

strain rate tensor and the anti-symmetric tensor \mathbf{A} is called spin tensor. By substituting Eqn S4.3 into Eqn S4.1 we obtain:

$$\Delta\mathbf{x}' \approx \Delta\mathbf{x} + \mathbf{S}\Delta\mathbf{x}\Delta t + \mathbf{A}\Delta\mathbf{x}\Delta t.\tag{S4.4}$$

Now we consider the change in the squared length after Δt :

$$\Delta l^2 \equiv |\Delta\mathbf{x}'|^2 - |\Delta\mathbf{x}|^2.\tag{S4.5}$$

By substituting Eqn S4.4 into Eqn S4.5:

$$\begin{aligned}\Delta l^2 &= |\Delta\mathbf{x}'|^2 - |\Delta\mathbf{x}|^2 \\ &= |\Delta\mathbf{x} + \mathbf{S}\Delta\mathbf{x}\Delta t + \mathbf{A}\Delta\mathbf{x}\Delta t|^2 - |\Delta\mathbf{x}|^2 \\ &= 2\sum_{i,j} S_{ij}\Delta x_i\Delta x_j\Delta t + O(\Delta x_i\Delta x_j\Delta t^2) \\ &\approx 2\Delta\mathbf{x}^T\mathbf{S}\Delta\mathbf{x}\Delta t.\end{aligned}\tag{S4.6}$$

In the last line of Eqn S4.6 we neglected the higher order terms. Thus, the change in the

distance between the two tracer points is a function of the strain tensor S . Note that the spin tensor A is related to the rotation of the relative positional vector $\Delta \mathbf{x}$ without changing its length. Since we are interested in relative cell movement that causes neighbor exchanges, we consider the strain rate tensor \dot{S} as the relevant quantity.

To compute spatial derivatives of cell velocity vectors, a continuum vector field is required. We obtained it from discrete velocity vector fields obtained from cell tracking data by using SPH (Liu et al., 2003) introduced in the next section.

Because the matrix representation of the strain rate tensor depends on a spatial coordinate system we chose arbitrarily, we computed the eigenvalues λ_i ($i = 1, 2, 3$; $|\lambda_1| \geq |\lambda_2| \geq |\lambda_3|$) that are rotationally invariant. We then defined the norm $|\lambda| \equiv \sqrt{\lambda_1^2 + \lambda_2^2 + \lambda_3^2}$ and considered it as a quantity for the magnitude of cell mixing. If the norm $|\lambda|$ was large, the magnitude of cell mixing was considered to be higher.

Fig. S4 shows spatial profiles of the norm $|\lambda|$ along the anterior-posterior axis of the PSMs for the four embryos. We computed $|\lambda|$ in the three-dimensional tissue and for visualization we projected values of $|\lambda|$ in the z direction into the two-dimensional x - y plane by maximum projection. We confirmed the same overall tendency of the spatial profiles in different projection methods. There is a spatial gradient of $|\lambda|$ in the PSM higher in the posterior region than in the anterior region (Fig. S4). The magnitude was highest in the tailbud region, suggesting the presence of cell mixing in that region. This observation is consistent with the results of the directional derivative modulus of velocity vectors in the main text (Fig. 1C). The norm $|\lambda|$ was also higher in the connecting tissue between the embryo and the yolk where a large tissue deformation could be observed. Thus, using the strain rate tensor, we determined the region in the PSM where cell mixing occurred.

Note that we might under-estimate the magnitude of local velocity variations with the strain rate tensor. Because of the presence of spontaneous cell movement, the velocity vector field in the tailbud would tend to be more random than in other parts of tissues. The random vector field may suffer stronger spatial smoothing in the SPH, resulting in

smaller modulus of velocity vectors. Perhaps this is why we observe larger values of the norm $|\lambda|$ in the connecting tissue than in the tailbud in Fig. S4, while we observe larger values of directional derivative modulus of velocity vectors in the tailbud than in the connecting tissue in Fig. 1C in the main text and Fig. S3.

S5. Smoothed particle hydrodynamics

We used the smoothed particle hydrodynamics (SPH) approach to construct a continuum velocity vector field from cell tracking data. A previous study applied this method to cell velocity data obtained in the zebrafish PSM (Lawton et al., 2013). Here we describe the SPH and our parameter settings, the interested reader is referred to (Liu et al., 2003) for a more detailed explanation of SPH.

The SPH spatially interpolates velocity vectors using a smoothing kernel by the following equation:

$$\mathbf{v}(t, \mathbf{x}) = \int W(\mathbf{x} - \mathbf{x}'; h) \mathbf{v}(t, \mathbf{x}') d\mathbf{x}', \quad (\text{S5.1})$$

where $W(\mathbf{x} - \mathbf{x}'; h)$ is the smoothing kernel with the length scale h for smoothing. The smoothing kernel has the properties $\int W(\mathbf{x} - \mathbf{x}'; h) d\mathbf{x}' = 1$ and $W(\mathbf{x} - \mathbf{x}'; h) \rightarrow \delta(\mathbf{x} - \mathbf{x}')$ as $h \rightarrow 0$. In our case, we have the data for velocity vectors $\mathbf{v}(t, \mathbf{x}_i)$ for cell i at position \mathbf{x}_i ($i = 1, 2, \dots, N$). Eqn S5.1 can be discretized by replacing the volume element in the integral with the volume of cells $d\mathbf{x}' \approx M_j / \hat{\rho}_j$ as:

$$\mathbf{v}(t, \mathbf{x}) \approx \sum_{j=1}^N \mathbf{v}(t, \mathbf{x}_j) \frac{M_j}{\hat{\rho}_j} W(\mathbf{x} - \mathbf{x}_j; h), \quad (\text{S5.2})$$

where M_j is the mass of cell j and $\hat{\rho}_j$ is the density of cell mass $\hat{\rho}_j = M_j / V_j$ with the volume V_j . We assumed $M = M_1 = \dots = M_N$ and applied the SPH for the density of cell mass:

$$\begin{aligned} \hat{\rho}(\mathbf{x}_j) &\approx \sum_{k=1}^N \hat{\rho}(\mathbf{x}_k) \frac{M_k}{\hat{\rho}(\mathbf{x}_k)} W(\mathbf{x}_j - \mathbf{x}_k; h) \\ &= M \sum_{k=1}^N W(\mathbf{x}_j - \mathbf{x}_k; h). \end{aligned} \quad (\text{S5.3})$$

Substituting $\hat{\rho}(\mathbf{x}_j)$ in Eqn S5.3, Eqn S5.2 reads:

$$\mathbf{v}(t, \mathbf{x}) \approx \sum_{j=1}^N \mathbf{v}(t, \mathbf{x}_j) \frac{W(\mathbf{x} - \mathbf{x}_j; h)}{\sum_{k=1}^N W(\mathbf{x}_k - \mathbf{x}_j; h)}. \quad (\text{S5.4})$$

The spatial derivative of $\mathbf{v}(t, \mathbf{x})$ can be computed as:

$$\partial \mathbf{v}(t, \mathbf{x}) / \partial x_i \approx \sum_{j=1}^N \mathbf{v}(t, \mathbf{x}_j) \frac{\partial W(\mathbf{x} - \mathbf{x}_j; h) / \partial x_i}{\sum_{k=1}^N W(\mathbf{x}_k - \mathbf{x}_j; h)}. \quad (\text{S5.5})$$

We chose the smoothing kernel by following the previous study (Lawton et al., 2013):

$$W(\mathbf{x} - \mathbf{x}_j; h) = C_d \begin{cases} \frac{2}{3} - \frac{9}{8} \left(\frac{|\mathbf{x} - \mathbf{x}_j|}{h} \right)^2 + \frac{19}{24} \left(\frac{|\mathbf{x} - \mathbf{x}_j|}{h} \right)^3 - \frac{5}{32} \left(\frac{|\mathbf{x} - \mathbf{x}_j|}{h} \right)^4, & 0 \leq \frac{|\mathbf{x} - \mathbf{x}_j|}{h} \leq 2 \\ 0, & 2 < \frac{|\mathbf{x} - \mathbf{x}_j|}{h} \end{cases} \quad (\text{S5.6})$$

with the normalization constant $C_d = 315\pi h^3 / 208$. The parameter h sets the length scale of the smoothing kernel. We examined the dependence of eigenvalues of the strain rate tensor on the parameter h . The overall qualitative tendencies of the spatial profile of $|\lambda|$ did not strongly depend on the values of h and similar profiles to those shown in Fig. S4 could be obtained. When the value of h was smaller, local variations of velocity vectors were preserved and the norm $|\lambda|$ of the eigenvalues of the strain rate tensor was larger. However, its spatial profile was noisier due to less smoothing. Hence, we chose to focus on the relative changes in velocity vectors that remained even under the smoothing with a relatively larger h . In Fig. S4, we used $h = 15 \mu\text{m}$. A previous study used a similar value of h (Lawton et al., 2013).

S6. Physical model of cell movement

In this section, we describe the physical model of cell movement that we use to fit the data. The model includes the movement of both cells and nuclei. The model was tailored to allow a straightforward comparison of relative cell movement and phase dynamics timescales.

Cell movement. Cells were represented as spheres of diameter d_c in a three-dimensional space $L_x \times L_y \times L_z$ (Fig. 3A). The three dimensional domain $L_x \times L_y \times L_z$ represents a local region somewhere in the PSM or in the tailbud. The number of cells N in the

model was constant and set so that the cell density $\rho = N/(L_x L_y L_z)$ was the same as observed in embryos (Fig. S7 and section S3 of the supporting text). For simplicity, we did not consider cell proliferation and apoptosis in the model. In embryonic tissue cells divide, flow into the tailbud from adjacent tissues, rearrange by convergent extension, and flow out from the tailbud into the PSM. Inclusion of these more complex tissue processes will set other timescales in the physical model. Modeling the influx and outflux of cells in the tailbud, as well as cell divisions would be an interesting avenue for future work.

Let $\mathbf{x}_i(t)$ be the position of the center of cell i ($i = 1, 2, \dots, N$) at time t . The over-damped equation of motion for the cell center in the main text is:

$$\frac{d\mathbf{x}_i(t)}{dt} = v_0 \mathbf{n}_i(t) + \mu \sum_{\substack{j=1 \\ j \neq i}}^N \mathbf{F}(\mathbf{x}_i, \mathbf{x}_j) + \mathbf{F}_b(\mathbf{x}_i), \quad (\text{Eqn 4 in the main text}) \quad (\text{S6.1})$$

where v_0 is the self-propulsion speed, $\mathbf{n}_i = (\sin\phi_i \cos\varphi_i, \sin\phi_i \sin\varphi_i, \cos\phi_i)$ is a unit vector representing the polarity of spontaneous cell movement in spherical coordinates (Fig. 3A), μ is a coefficient giving the relative strength of intercellular forces, $\mathbf{F}(\mathbf{x}_i, \mathbf{x}_j)$ is a physical force between cells i and j , and \mathbf{F}_b is the confinement force exerted by the boundary of the domain.

In the absence of forces, cell i moves spontaneously in the direction of cell polarity \mathbf{n}_i at speed v_0 . For simplicity, we model the dynamics of the polarity angles ϕ_i and φ_i of the unit vector \mathbf{n}_i as a diffusion processes:

$$\frac{d\phi_i(t)}{dt} = \frac{D_\phi}{\tan\phi_i} + \sqrt{2D_\phi} \xi_i(t), \quad (\text{S6.2a})$$

$$\frac{d\varphi_i(t)}{dt} = \frac{\sqrt{2D_\phi}}{\sin\phi_i} \zeta_i(t), \quad (\text{S6.2b})$$

where D_ϕ is the polarity noise strength and $\xi_i(t)$ and $\zeta_i(t)$ are white Gaussian noises satisfying $\langle \xi_i(t) \rangle = 0$, $\langle \zeta_i(t) \rangle = 0$, $\langle \xi_i(t) \xi_j(t') \rangle = \delta_{ij} \delta(t - t')$, $\langle \zeta_i(t) \zeta_j(t') \rangle = \delta_{ij} \delta(t - t')$ and $\langle \xi_i(t) \zeta_j(t') \rangle = 0$. Under these two stochastic equations, the polarity vector \mathbf{n}_i performs random walk on a unit sphere with diffusion constant D_ϕ . Accordingly, in the absence of forces, cells move at instantaneous speed $d\mathbf{x}_i/dt = v_0 \mathbf{n}_i(t)$ with a characteristic auto-correlation time $\sim 1/(2D_\phi)$. The deterministic term $D_\phi/\tan\phi_i$ in Eqn S6.2a is required

for the isotropic diffusion of \mathbf{n}_i on a unit sphere, as described in spherical coordinates.

For the physical force $\mathbf{F}(\mathbf{x}_i, \mathbf{x}_j)$ between two cells we considered a volume exclusion effect (Fig. 3A). Two cells at a distance closer than the cell diameter d_c repel each other. This is modeled as a linear repulsive force $\mathbf{F}(\mathbf{x}_i, \mathbf{x}_j) = F(\mathbf{x}_i, \mathbf{x}_j)\mathbf{e}_{ij}$, with $\mathbf{e}_{ij} = (\mathbf{x}_j - \mathbf{x}_i) / |\mathbf{x}_j - \mathbf{x}_i|$ and magnitude

$$F(\mathbf{x}_i, \mathbf{x}_j) = \begin{cases} r_{ij}/d_c - 1 & r_{ij} \leq d_c \\ 0 & r_{ij} > d_c, \end{cases} \quad (\text{S6.3})$$

where $r_{ij} = |\mathbf{x}_j - \mathbf{x}_i|$.

Cells were confined within the domain $L_x \times L_y \times L_z$ by boundary forces

$$\mathbf{F}_b(\mathbf{x}_i) = (F_{bx}(\mathbf{x}_i), F_{by}(\mathbf{x}_i), F_{bz}(\mathbf{x}_i)). \quad (\text{S6.4})$$

We described this confinement force as:

$$F_{bw}(\mathbf{x}_i) = \begin{cases} \nu e^{-w/\gamma_b} & w \leq L_w/2, \\ -\nu e^{-(L_w-w)/\gamma_b} & w > L_w/2, \end{cases} \quad (\text{S6.5})$$

where $w \in \{x, y, z\}$, ν is the coefficient of boundary force and γ_b is its length scale ($\gamma_b/L_w \ll 1$).

Nuclear movement. Since we tracked cell nuclei in embryonic imaging data, we explicitly model nuclear movement inside a cell to account for its contribution to the MSDD (Fig. 3A). Each nucleus is represented as a sphere with the radius r_n , ($0 \leq r_n < d_c/2$). Let $\mathbf{q}_i(t)$ be the position of the nucleus for cell i at time t and $\Delta\mathbf{q}_i(t)$ be the relative nuclear position from the cell center $\mathbf{x}_i(t)$. A nucleus stays inside a cell as described by $0 \leq |\Delta\mathbf{q}_i| < d_c/2 - r_n$. $\mathbf{q}_i(t)$ can then be written as $\mathbf{q}_i(t) = \mathbf{x}_i(t) + \Delta\mathbf{q}_i(t)$. We assumed that the movement of the cell nucleus was random in the cytoplasmic region:

$$\frac{d\Delta\mathbf{q}_i}{dt} = \mathbf{f}(\Delta\mathbf{q}_i) + \sqrt{2D_n}\boldsymbol{\eta}_i(t), \quad (\text{S6.6})$$

where \mathbf{f} represents the confinement force on the nucleus exerted by the cell boundary, D_n is the diffusion constant of the nucleus and $\boldsymbol{\eta}_i = (\eta_{ix}, \eta_{iy}, \eta_{iz})$ is a three dimensional vector of white Gaussian noise with $\langle \eta_{ia}(t) \rangle = 0$ and $\langle \eta_{ia}(t) \eta_{jb}(t') \rangle = \delta_{ij} \delta_{ab} \delta(t - t')$ ($a, b \in \{x, y, z\}$).

$y, z\}$). We describe the magnitude of the nuclear confinement force by an exponential function of $\Delta\mathbf{q}_i(t)$:

$$\mathbf{f}(\Delta\mathbf{q}_i) = -\mu_b \exp\left[\frac{-(d_c - 2|\Delta\mathbf{q}_i| - 2r_n)}{2\gamma}\right] \frac{\Delta\mathbf{q}_i}{|\Delta\mathbf{q}_i|}, \quad (\text{S6.7})$$

where μ_b is the coefficient of the confinement force, γ is the length scale of the force and $-\Delta\mathbf{q}_i/|\Delta\mathbf{q}_i|$ is the vector pointing towards the cell center. By setting this confinement force strong enough ($\sqrt{2D_n}/\mu_b \ll 1$), the nucleus stayed inside of the cell $0 \leq |\Delta\mathbf{q}_i| < d_c/2 - r_n$.

S7. Approximate Bayesian Computation

To fit the physical model of cell movement to experimentally obtained mean squared difference of displacement vectors (MSDD), we used the Approximate Bayesian Computation based on Markov Chain Monte Carlo (ABC MCMC; (Marjoram et al., 2003)). The physical model described in the section S6 has six free parameters, the self-propulsion speed v_0 , repulsive force coefficient μ , polarity noise strength D_ϕ , diffusion constant of the nucleus D_n , nucleus confinement force μ_b and confinement force length scale γ . A set of these parameters is represented as a vector

$\vartheta = (v_0, \mu, D_\phi, D_n, \mu_b, \gamma)$ below.

Given quantitative experimental data D_a , the MCMC can in general numerically construct the posterior distribution of parameters $p(\vartheta | D_a)$ from a prior distribution $p(\vartheta)$ with Bayes theory. To do this, the likelihood $p(D_a | \vartheta)$ is required but is often difficult to derive. ABC MCMC replaces the likelihood by a distance d_s between the summary statistics of the data and simulation, and approximates the posterior distribution as $p(\vartheta | D_a) \approx p(\vartheta | d_s \leq \varepsilon)$ where ε is a tolerance.

We used the MSDD as the summary statics in the ABC MCMC because the MSDD is likely to be a function of all the parameters in the physical model. Let $m(t_i)$ be the MSDD measured in an embryo at time t_i ($i = 1, \dots, T$) and $m_s(t_i)$ be the MSDD obtained by a numerical simulation of the physical model. We defined the distance

between these MSDD $d_s(m, m_s)$ as:

$$d_s(m, m_s) = \sum_{i=1}^T \frac{\{m(t_i) - m_s(t_i)\}^2}{m(t_i)^2}. \quad (\text{S7.1})$$

Although both $m(t_i)$ and $m_s(t_i)$ are time series data and should have correlations between successive time points, we neglected these temporal correlations and treated these data as independent data points in Eqn S7.1.

The ABC MCMC algorithm proceeds as follows:

A1. Draw the values of parameters ϑ_j ($j = 0$) from the prior distribution $p(\vartheta)$ for initialization.

A2. Propose a set of values of parameters ϑ' from the proposal distribution $g(\vartheta_j \rightarrow \vartheta')$.

A3. Carry out a numerical simulation of the physical model with the parameter set ϑ' and compute $m_s(t_i)$.

A4. If $d_s(m, m_s) \leq \varepsilon$, go to A5, otherwise set $\vartheta_{j+1} = \vartheta_j$ and go to A6.

A5. Set $\vartheta_{j+1} = \vartheta'$ with probability $p_a = \min\left(1, \frac{p(\vartheta')}{p(\vartheta)}\right)$ and $\vartheta_{j+1} = \vartheta_j$ with probability $1 - p_a$.

A6. Set $j = j + 1$ and go to A2.

To define the prior distribution $p(\vartheta)$, we set a uniform distribution for each parameter:

$$p(\chi) = \begin{cases} \frac{1}{\chi^{(\max)} - \chi^{(\min)}}, & \chi^{(\min)} \leq \chi \leq \chi^{(\max)} \\ 0, & \text{otherwise} \end{cases} \quad (\text{S7.2})$$

where $\chi \in \{v_0, \mu, D_\phi, D_n, \mu_b, \gamma\}$. The intervals for uniform distributions were chosen to be biologically plausible and are listed in Table S5. Then, the prior distribution $p(\vartheta)$ was defined as:

$$p(\vartheta) = p(v_0)p(\mu)p(D_\phi)p(D_n)p(\mu_b)p(\gamma). \quad (\text{S7.3})$$

To propose a set of parameter values from ϑ_j , we used

$$\vartheta' = \vartheta_j + \Delta\vartheta, \quad (\text{S7.4})$$

where $\Delta\vartheta = (\Delta\vartheta_{v_0}, \Delta\vartheta_{\mu}, \Delta\vartheta_{D_\phi}, \Delta\vartheta_{D_n}, \Delta\vartheta_{\mu_b}, \Delta\vartheta_{\gamma})$ is the vector of which each element is drawn from the normal distribution $N(0, \sigma_\chi)$, ($\chi \in \{v_0, \mu, D_\phi, D_n, \mu_b, \gamma\}$). Note the symmetry $g(\vartheta \rightarrow \vartheta') = g(\vartheta' \rightarrow \vartheta)$ in this setting. The values of σ_χ are listed in Table S5.

We set the tolerance as $\varepsilon = 2$. We collected more than 4000 samples and discarded the initial 1000 as transients. To check the convergence of the distribution, we compared 5 independent realizations of ABC MCMC sampling. Similar distributions were observed in all these 5 realizations, one of them is shown in Fig. S8A and B.

We found a few necessary conditions for explaining the MSDD data in the tailbud. There was a clear correlation between the self-propulsion velocity v_0 and the intercellular force coefficient μ (Fig. S8A). These two parameters largely determined the cell velocity \mathbf{v}_i in simulations. To reproduce the experimental MSDD, the cell velocity had to be strictly constrained. The length scale of the nuclear confinement force γ must be small (Fig. S8B), indicating that nuclei should move freely within cells.

Using the fitted model we estimated single-cell velocities and velocity auto-correlation in the tailbud (Fig. S9). It would be difficult to obtain these quantities directly from embryonic images due to the influence of global tissue motion and deformation. A velocity modulus distribution (Fig. S9A) was obtained from the fit to tailbud data of the 17 ss embryo in Fig. 2. In the simulation, the mean of velocity modulus was $\langle |\mathbf{v}| \rangle = 0.58 \pm 0.31 \mu\text{m min}^{-1}$. This is an estimate of the cellular velocity modulus *in vivo*. The values of the average velocity modulus for the other three embryos estimated from simulations were similar to this value (Fig. S9B). We also estimated the timescale of velocity auto-correlation for a single cell in the tailbud from the fitted model (Fig. S9C, D). This timescale represents the persistence time for a cell to keep moving in one direction. The velocity auto-correlation C_a was defined using the velocity vector for cell i in a

simulation \mathbf{v}_i as

$$C_a(\tau) = \frac{1}{N} \sum_{i=1}^N \frac{\mathbf{v}_i(\tau) \cdot \mathbf{v}_i(0)}{|\mathbf{v}_i(\tau)| |\mathbf{v}_i(0)|}, \quad (\text{S7.5})$$

where N is the total number of cells in the physical model.

The auto-correlation decays as a double-exponential curve in simulations (Fig. S9C). We fitted separate exponential functions $c_0 \exp(-t/\tau_a)$ at short and long timescales to the data and obtained their characteristic time τ_a . For the 17 ss embryo in Fig. 2A, $\tau_a \approx 4.3$ min for short timescales and $\tau_a \approx 13.3$ min for long timescales (Fig. S9C). The timescale of the second decay is set by the polarity noise strength D_ϕ in the model. In addition, the values of auto-correlation were quite small (less than 0.2) in this regime. So, we argue that the timescale of the first decay is more relevant for cell movement in the tissue. We obtained similar values of the persistence time for the other three embryos in simulations (Fig. S9D).

S8. Mean-field system

Our previous study (Uriu et al., 2013) demonstrated that when relative movement of oscillators is sufficiently fast, a population of the mobile oscillators behaves as a mean-field system, where each oscillator interacts with all the other oscillators in the system. To examine whether the observed cell mixing in the tailbud is fast enough for the genetic oscillators to be in the mean-field regime, we compare their dynamics with the following mean field system (Kuramoto, 1984):

$$\frac{d\theta_i(t)}{dt} = \omega_i + \frac{\kappa}{N} \sum_{j=1}^N \sin(\theta_j(t) - \theta_i(t)) + \sqrt{2D_\theta} \xi_{\theta_i}, \quad (\text{S8.1})$$

where N is the total number of oscillators in the system. We used the same frequency distribution and the values of parameters in Eqn S8.1 as those in Eqn 5 in the main text. Fig. S14 shows the difference of synchronization dynamics between the mean-field system Eqn S8.1 and the oscillators with reproduced cell mixing. When the value of the coupling strength κ is smaller, their behaviors are closer. As the coupling strength increases, the difference becomes larger. The results shown in Fig. S14 suggest that the observed cell mixing in the tailbud is not fast enough for the cells to behave as a mean-field system.

Supplementary References

- Bhavna, R., Uriu, K., Valentin, G., Tinevez, J. Y. and Oates, A. C.** (2016). Object Segmentation and Ground Truth in 3D Embryonic Imaging. *PLoS One* **11**, e0150853.
- Kuramoto, Y.** (1984). *Chemical oscillations, waves, and turbulence*. Berlin: Springer-Verlag.
- Lawton, A. K., Nandi, A., Stulberg, M. J., Dray, N., Sneddon, M. W., Pontius, W., Emonet, T. and Holley, S. A.** (2013). Regulated tissue fluidity steers zebrafish body elongation. *Development* **140**, 573-582.
- Li, G., Liu, T., Nie, J., Guo, L., Malicki, J., Mara, A., Holley, S. A., Xia, W. and Wong, S. T.** (2007). Detection of blob objects in microscopic zebrafish images based on gradient vector diffusion. *Cytometry. Part A : the journal of the International Society for Analytical Cytology* **71**, 835-845.
- Liu, M. B., Liu, G. R. and Lam, K. Y.** (2003). Constructing smoothing functions in smoothed particle hydrodynamics with applications. *Journal of Computational and Applied Mathematics* **155**, 263-284.
- Marjoram, P., Molitor, J., Plagnol, V. and Tavaré, S.** (2003). Markov chain Monte Carlo without likelihoods. *Proc Natl Acad Sci U S A* **100**, 15324-15328.
- Sbalzarini, I. F. and Koumoutsakos, P.** (2005). Feature point tracking and trajectory analysis for video imaging in cell biology. *Journal of structural biology* **151**, 182-195.
- Uriu, K., Ares, S., Oates, A. C. and Morelli, L. G.** (2013). Dynamics of mobile coupled phase oscillators. *Physical Review E* **87**, 032911.

Supplementary Information

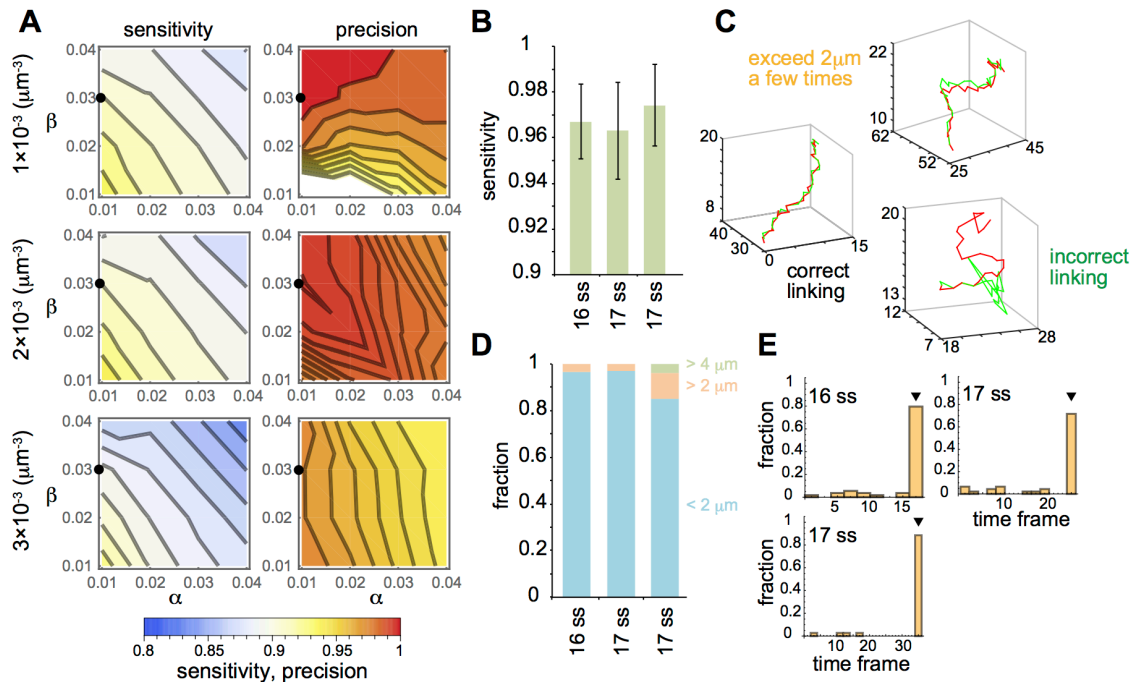


Figure S1 Validation of the tracking algorithm with synthetic images and three chimeric embryos. (A) Dependence of sensitivity and precision on the parameters α and β in the gradient vector diffusion algorithm for three different object densities. The filled circles represent the set of α and β used in the main text. (B) Sensitivity of the gradient vector diffusion algorithm in the three transplanted embryos. Averages and standard deviations over 10 time frames are shown. ss: somite stage. (C) Examples of cell trajectories. Each trajectory obtained in the dense (GFP) channel is classified into three categories depending on the distance from the corresponding trajectory in the sparse (mCherry) channel. The red lines represent cell trajectories in the sparse channel and the green lines represent the corresponding trajectories in the dense channel. (D) Fraction of three categories shown in (C). (E) Histograms of the trajectory length. Correctly linked trajectories ($< 2 \mu\text{m}$) were used in the histograms. Arrowheads indicate the last time frame of the time lapse movie. Values of parameters in the gradient vector diffusion algorithm are listed in Table S4.

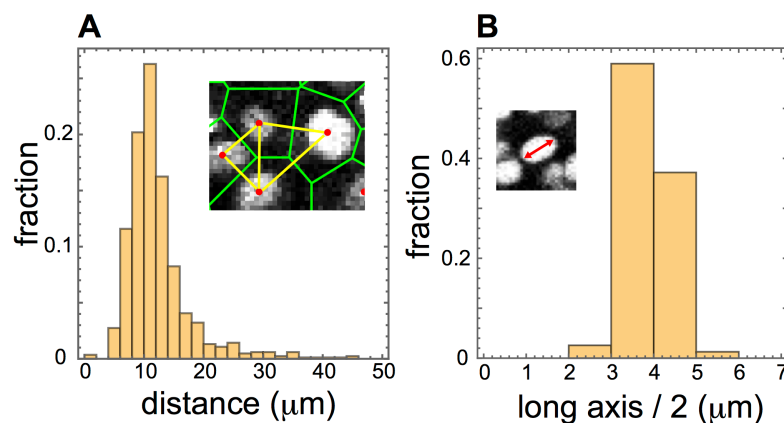


Figure S2 Estimation of cell size and quantification of nucleus size. (A) Histogram of the distances between two neighboring cells (yellow lines) for a 17 somite stage embryo. To determine neighboring relations the three-dimensional Voronoi tessellation (green lines) was used for the nuclear positions. Assuming that cells are close-packed, this procedure gives a good estimate for cell size. See supporting text for details. (B) Histogram of the half of the long axis of nucleus in the posterior PSM. Data from the four embryos was gathered to make the histogram.

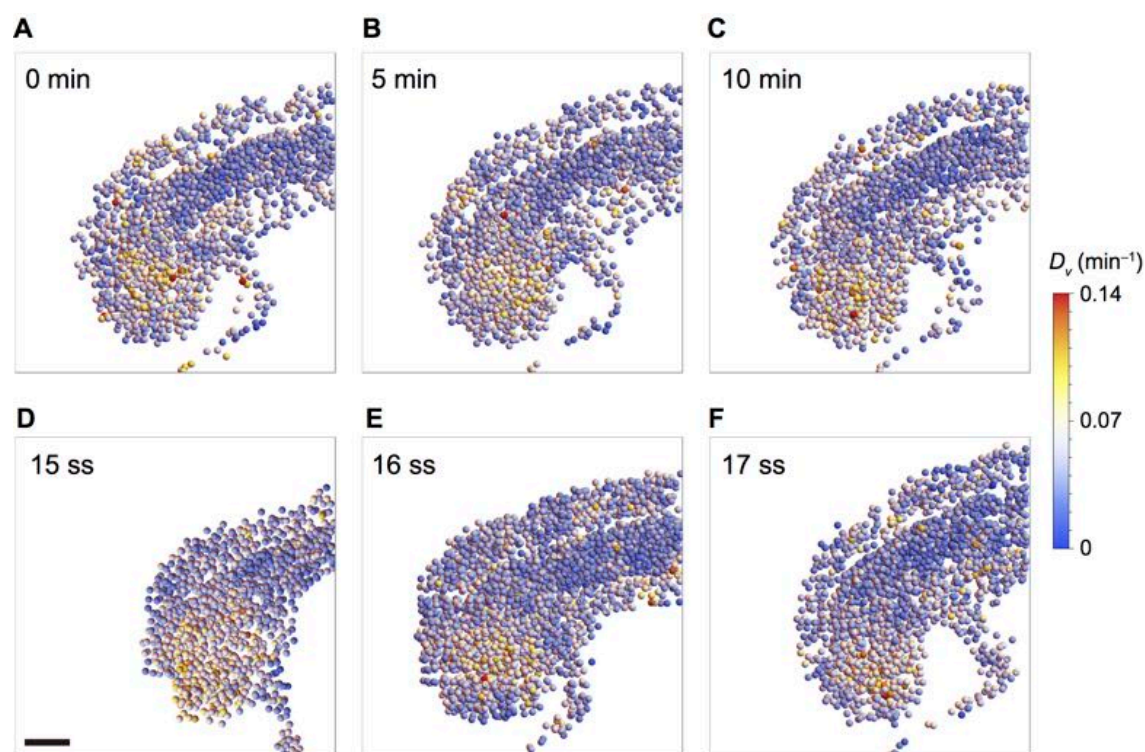


Figure S3 Average directional derivative modulus D_v for the 15-17 somite stage embryos. (A)-(C) Time series of D_v for the 17 somite stage (ss) embryo shown in Fig. 1 in the main text. (D)-(F) Spatial profiles of D_v for (D) 15 ss, (E) 16 ss and (F) 17 ss embryos. Scale bar = 50 μm.

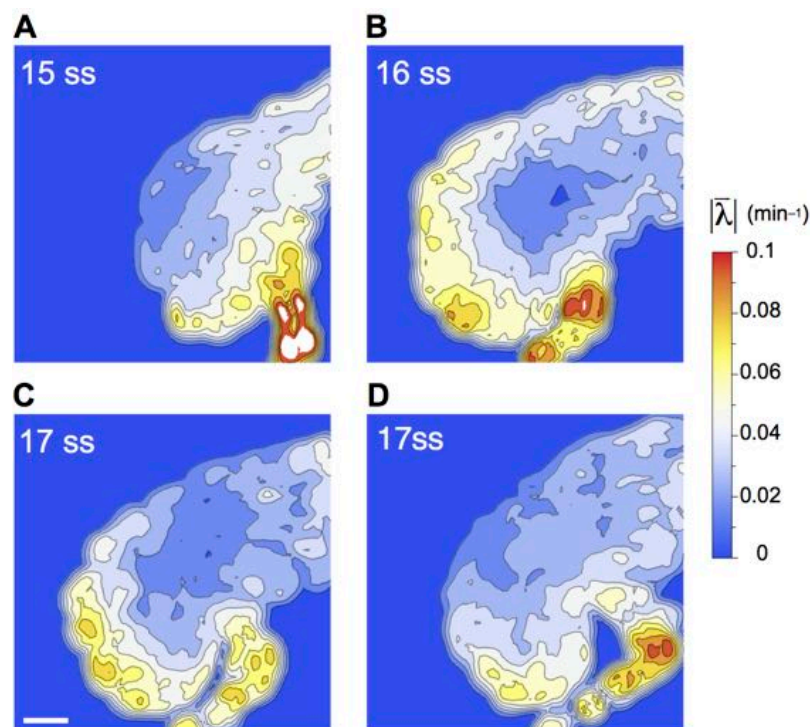


Figure S4 Quantification of cell mixing by the strain rate tensor. (A)-(D) Spatial profiles of the norm of eigenvalues $|\lambda|$ for (A) a 15 somite stage (ss), (B) a 16 ss, and (C), (D) 17 ss embryos. The maximum z -projection for the norm was applied. Eigenvalues of the strain rate tensor at each spatial position were computed after interpolating velocity vectors with the smoothed particle hydrodynamics (SPH). $h = 15 \mu\text{m}$ in the SPH. See supporting text for details. Scale bar = 50 μm .

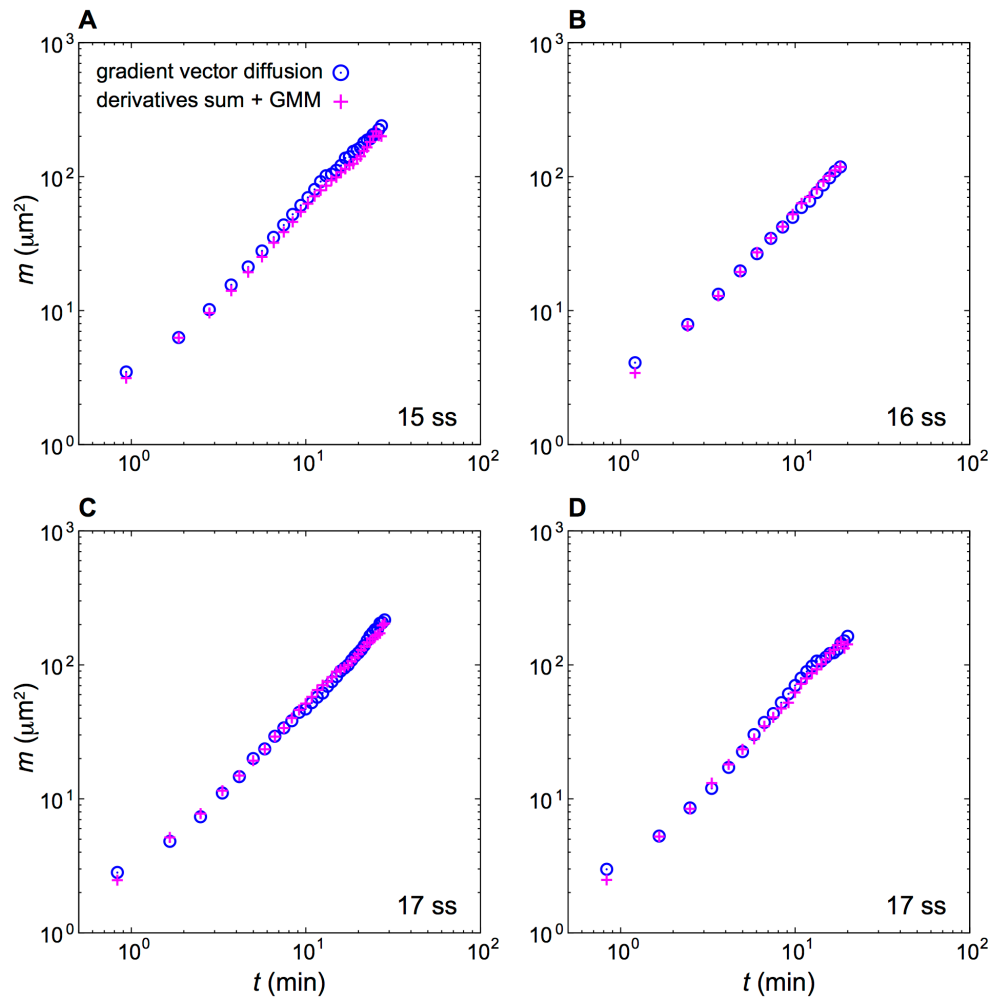


Figure S5 Comparison of the mean squared difference of displacement vectors (MSDD) obtained by two different nuclear detection algorithms. (A)-(D) MSDD for the tailbuds of (A) the 15 somite stage (ss), (B) 16 ss, and (C), (D) 17 ss embryos. Results obtained by the gradient vector diffusion algorithm (circles; main text) and by the derivatives sum (DS) nuclear segmentation algorithm (crosses; Bhavna et al., 2016) are shown for comparison. The DS algorithm is based on (Bhavna et al., 2016). Before applying the DS algorithm, the Gaussian noise filter and the isotropic nonlinear diffusion filter were used for noise reduction. Values of parameters in the DS algorithm were $\alpha = \beta = \gamma = \delta = 1$ and $\varepsilon = 2$. Gaussian Mixture Model was used as a post-processing method. The nearest neighbor linking algorithm was used after detecting the nuclear positions by these two nuclear detection algorithms.

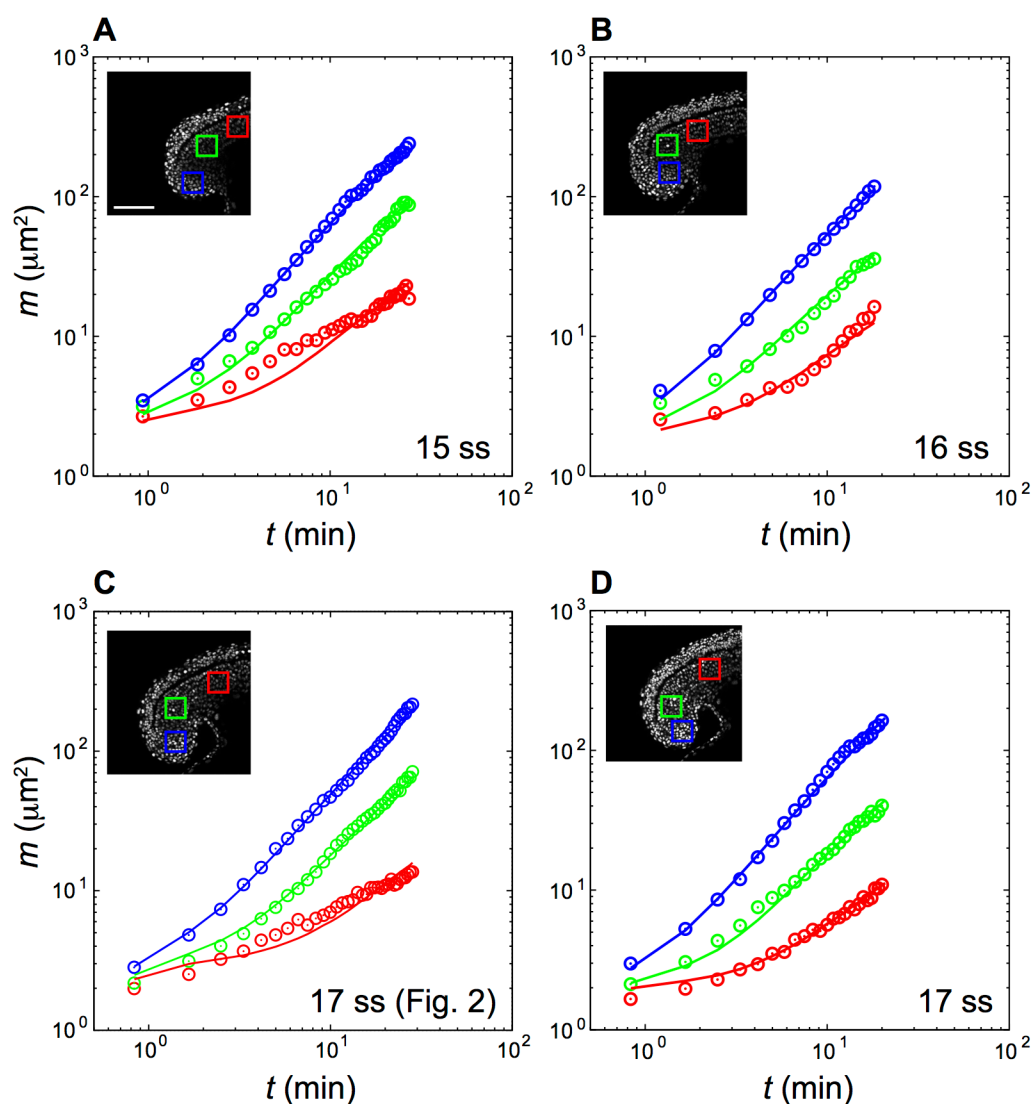


Figure S6 Quantification of cell mixing in the 15-17 somite stage zebrafish embryos by the mean squared difference of displacement vectors (MSDD). (A)-(D) Time evolution of the MSDDs for (A) 15 somite stage (ss), (B) 16 ss and (C),(D) 17 ss embryos. Circles represent experimental data. Lines are fitting by the physical model of cell movement to the experimental data. The colored boxes in the inset images indicate the regions for which the MSDD was calculated. The color code of the MSDD matches that of the boxes. The values of parameters in the model are listed in Tables S1 and S2. Scale bar = 100 μm in (A).

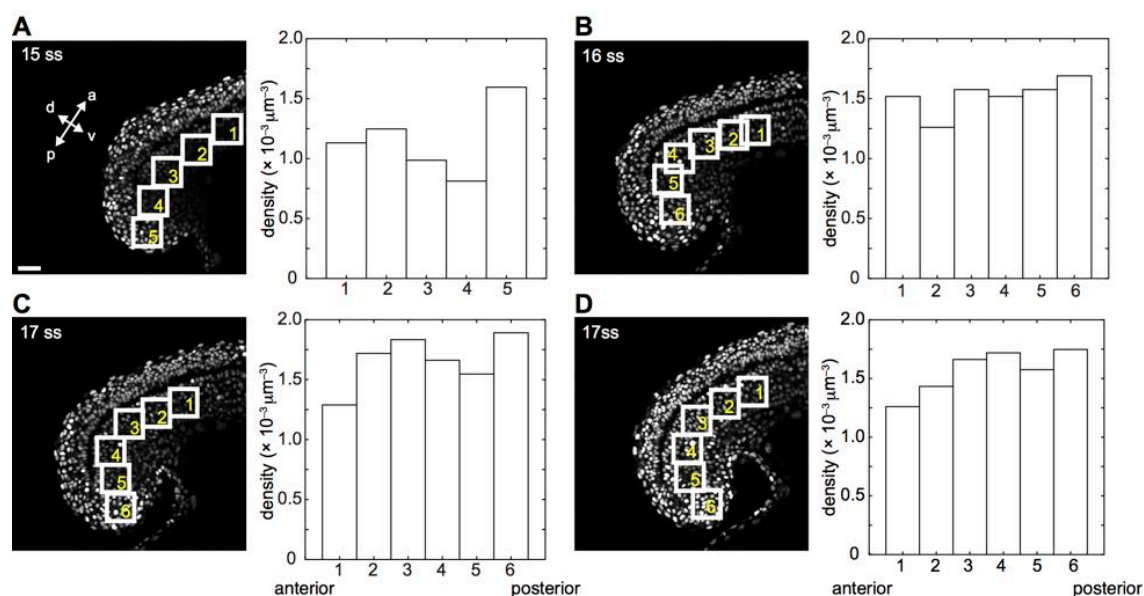


Figure S7 Nuclear density across the tailbud and PSM for the four embryos. (A)-(D) Snapshot image (left) and nuclear density (right) for (A) 15 somite stage (ss), (B) 16 ss and (C), (D) 17 ss embryos. Numbers in the six (five in (A)) white boxes correspond to those in the right bar charts. 1 (anterior most) to 6 (tailbud). Scale bar = 50 μm in (A).

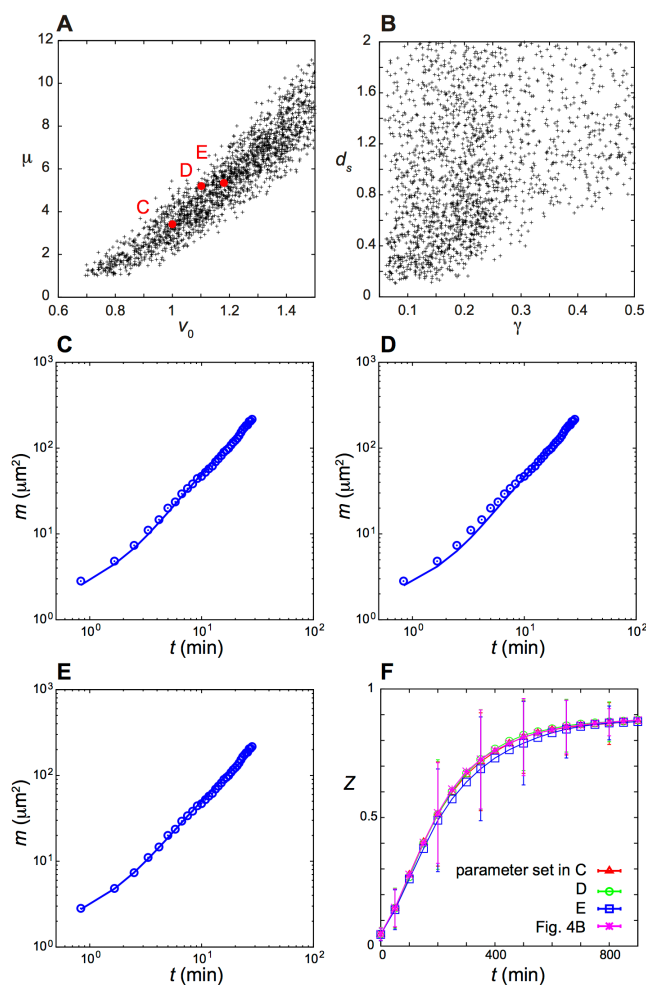


Figure S8 Different parameter sets that reproduced observed cell mixing in the tailbud. (A) Scatter plot of the values of the self-propulsion speed v_0 and the coefficient of repulsive force μ obtained by ABC MCMC sampling. The MSDD data for the tailbud of the 17 somite stage (ss) embryo shown in Fig. 2 were used in the ABC MCMC sampling. Three red points indicate the values used in (C)-(E). (B) Distance d_s in the ABC MCMC as a function of the length scale of nuclear confinement force γ in the physical model. A smaller value of d_s means a better fitting to the data. (C)-(E) Time evolution of the MSDD for the tailbud of the 17 ss embryo. Circles represent experimental data and the same data are plotted in (C)-(E). Lines are fitting by the physical model with three different parameter sets. These parameter sets are listed in Table S1 and the values of their v_0 and μ are plotted in (A) as the red circles. (F) Time evolution of the phase order parameter Z in the presence of reproduced cell mixing shown in the panels (C)-(E) and in Fig. 2 of the main text.

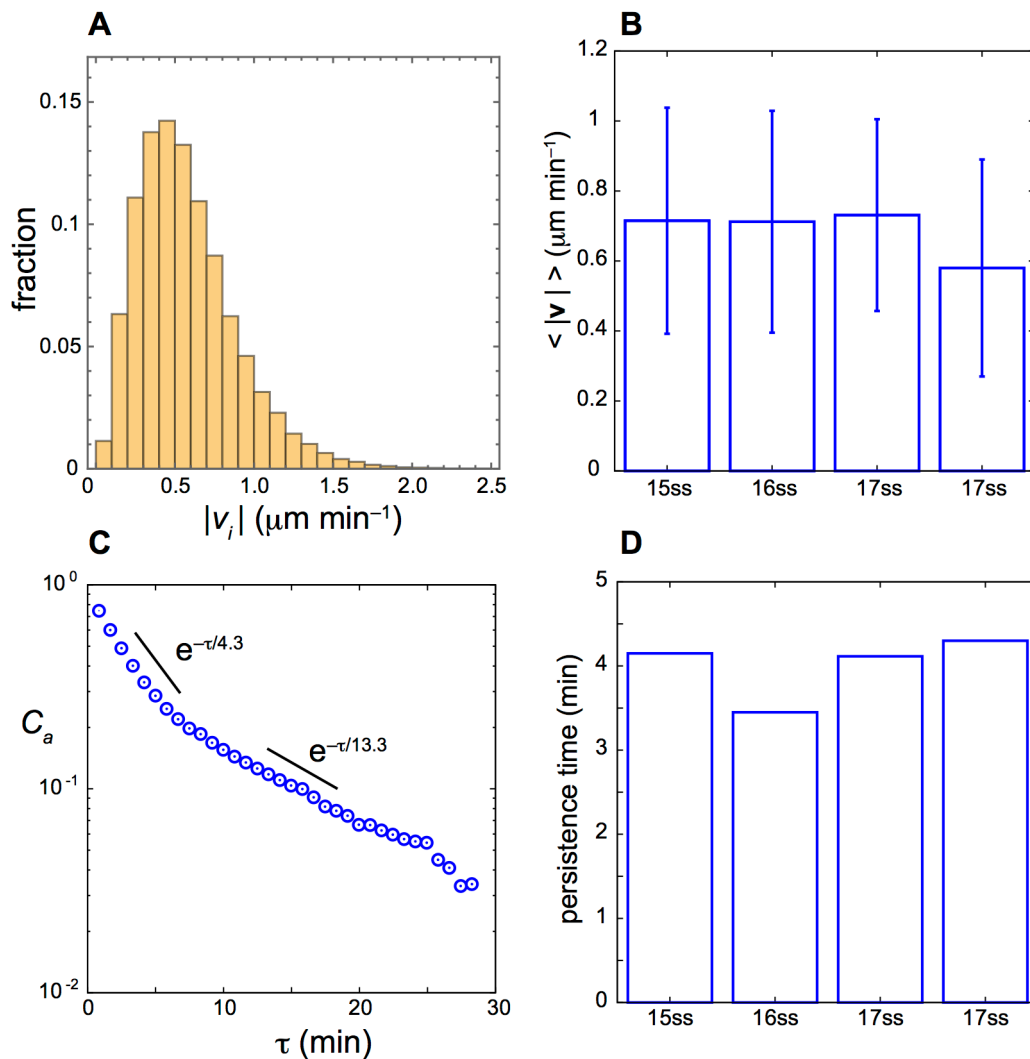


Figure S9 Estimation of cell velocity modulus and velocity auto-correlation in the embryonic tailbud from the fitted physical model. (A) Histogram of velocity modulus in a simulation of the physical model. (B) Average velocity modulus obtained by simulations of the fitted models for the tailbud of the four embryos. Error bars represent the standard deviations of the velocity modulus distribution in simulations. ss: somite stage. (C) Velocity auto-correlation for a single cell in the fitted model as a function of time τ . (D) Persistence time of velocity auto-correlation at a short timescale obtained by the fitted models for the tailbud of the four embryos. The values of parameters in the model are the ones that reproduced the mean squared difference of displacement vectors in the tailbuds of these embryos.

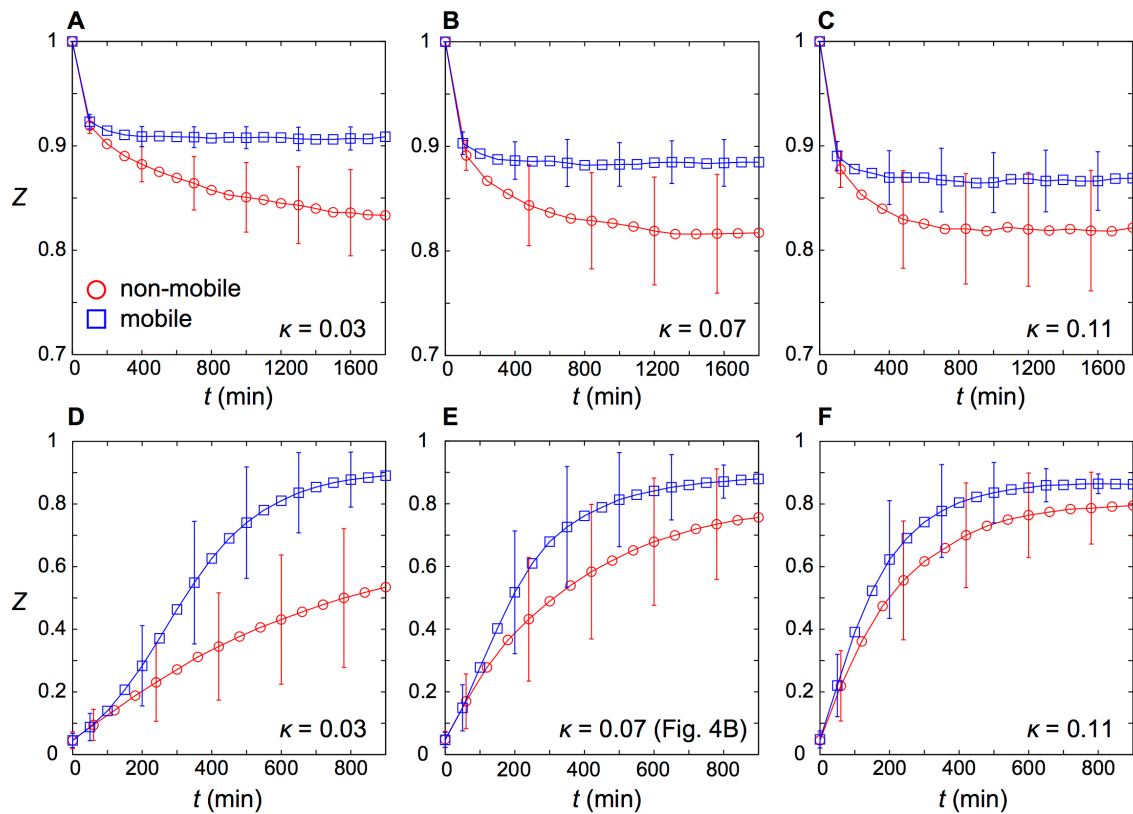


Figure S10 The influence of reproduced cell mixing on synchronization depends on the coupling strength κ . (A)-(C) Time evolution of the phase order parameter Z when simulations were started from a completely synchronized state ($Z(0) = 1$). (A) $\kappa = 0.03$, (B) 0.07 and (C) 0.11 min^{-1} . (D)-(F) Time evolution of the phase order parameter Z with (D) $\kappa = 0.03$, (E) 0.07 and (F) 0.11 min^{-1} . In (D)-(F), simulations were started from random phases. In all panels, blue squares are the results in the presence of reproduced mixing. Red circles are results for non-mobile cells for comparison. The standard deviation of frequency distribution σ_ω was scaled as $\kappa = \sigma_\omega/\omega_0$. Also, the phase noise intensity was scaled as $D_\theta/\kappa = 1/10$. Averages over 200 different realizations are plotted. The error bars represent the standard deviations of phase order parameter Z . Values of parameters are listed in Tables S1-S3.

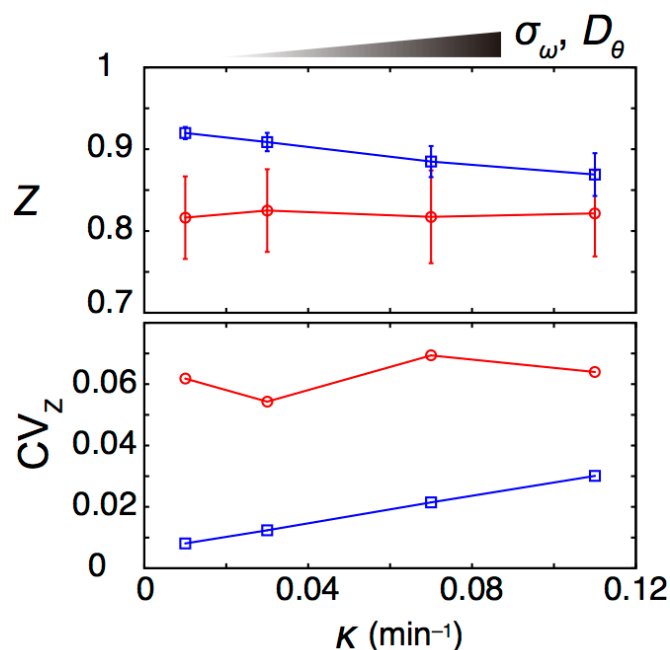


Figure S11 Reproduced cell mixing improves robustness of the synchronized state against phase noise. Top: steady state values of Z as a function of the coupling strength κ for the reproduced mixing (blue squares, $v_0 = 1.39$) and no movement (red circles, $v_0 = 0.14$). Bottom: Coefficient of variation of Z as a function of κ . Simulations were started from an initial condition where all the cells were completely synchronized ($Z(0) = 1$; Fig. S10A-C). Due to frequency noise, the phase order parameter Z decreased and reached a steady state value below 1 (Fig. S10A-C). The non-mobile oscillators' phase dispersion at steady state was fixed by adjusting κ and σ_ω , keeping the relation $\kappa = \sigma_\omega/\omega_0$ and $D_\theta/\kappa = 1/10$. Because of this scaling, the average phase order parameter Z for non-mobile oscillators at the steady state is almost constant even for different values of κ . Remarkably, Z for mobile oscillators was larger than that for non-mobile oscillators. Moreover, the coefficient of variation (CV) of the order parameter for mobile oscillators was smaller, indicating lower fluctuations in phase order. The difference between mobile and non-mobile oscillators was larger both in the average value of Z and CV when κ was small. Error bars indicate the standard deviations of Z over 200 realizations of simulations. The values of all other parameters are listed in Tables S1-S3.

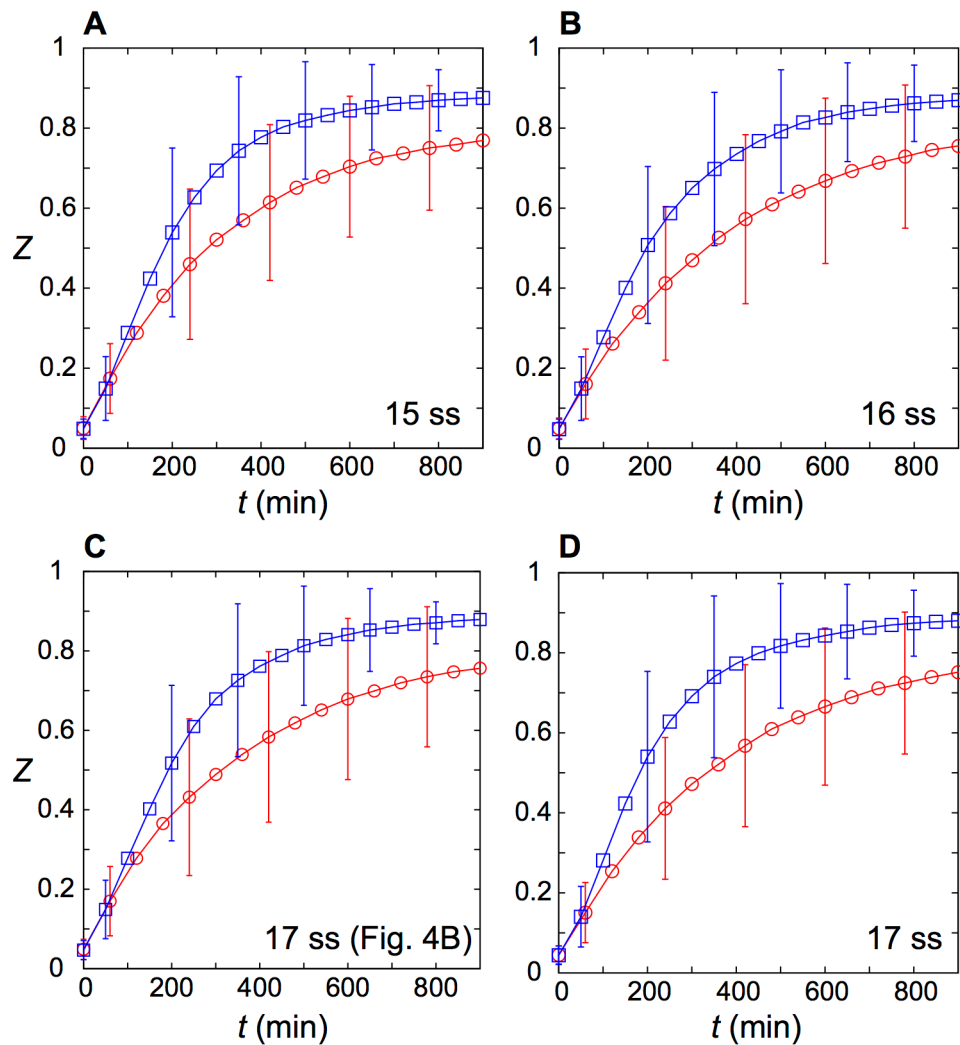


Figure S12 Reproduced cell mixing in the four embryos enhance synchronization of coupled phase oscillators. (A-D) Time evolution of the phase order parameter Z for the four embryos. These embryos correspond to those in Fig. S6. Cell mixing in the tailbud of each embryo was reproduced. Blue squares are the results in the presence of reproduced mixing. Red circles are results in the absence of cell mixing for comparison. Averages over 200 different realizations are plotted. The error bars represent the standard deviations. Values of parameters are listed in Tables S1-S3.

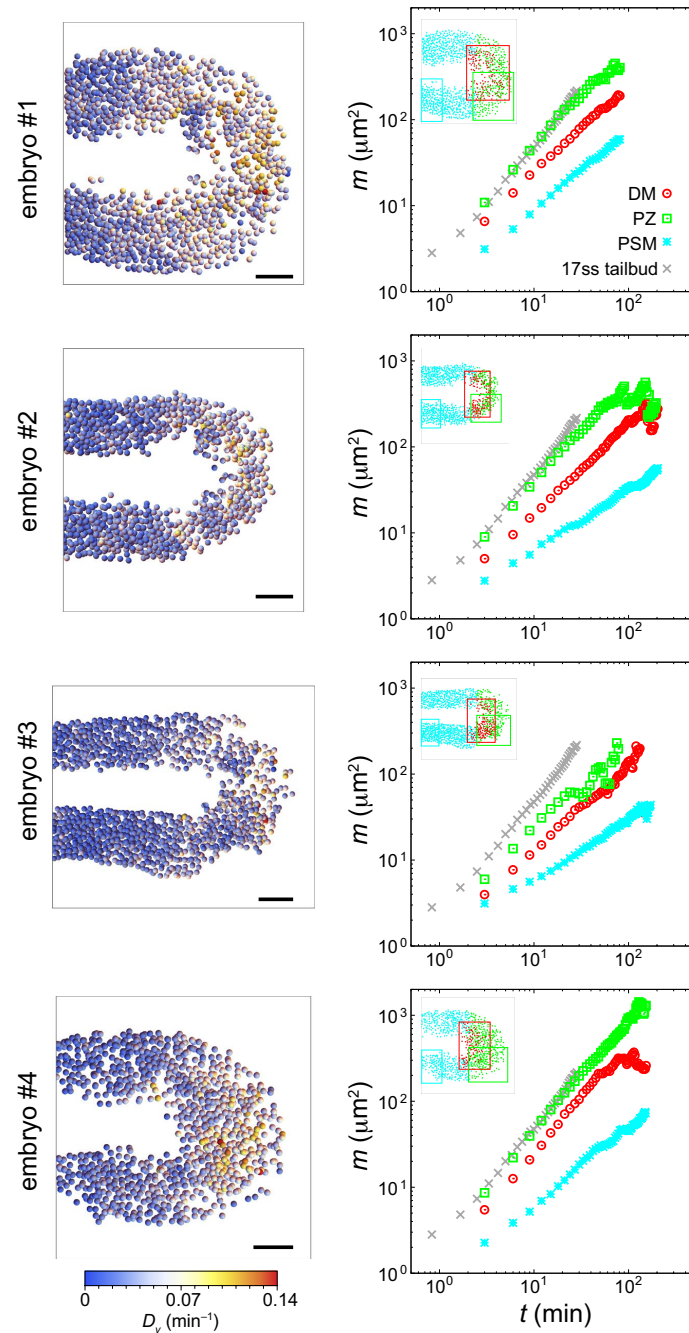


Figure S13 Cell mixing in the PSM and tailbud in 10 somite stage wild type zebrafish embryos growing at 18°C (Lawton data set). Left column: spatial profile of directional derivative modulus defined by Eqn 2 in the main text for four embryos. Cell trajectory data used for calculations is from Lawton et al., 2013 and was kindly provided by Scott Holley (Yale University). Dorsal view is shown. Anterior is left. Right column: time evolution of the mean squared difference of displacement vectors

(MSDD) for the dorsal medial (DM, the tailbud dorsal to the axial and paraxial mesoderm; red), progenitor zone (PZ, ventral to the dorsal medial zone and posterior to the notochord; green) and a PSM region (PSM; cyan). PZ corresponds to the region we refer to as tailbud in 15-17 somite stage (ss) embryos. For comparison, MSDD for cells in the tailbud in a 17 ss embryo is plotted (grey; Fig. 2). Inset figures indicate the tissue regions for which MSDD was calculated. Left halves of the PZ and PSM were used for the MSDD calculations to correspond to the lateral images analyzed in this study. The previous study (Lawton et al., 2013) reported that cells in the DM move more coherently (i.e. less relative movement) than those in the PZ. Consistent with this observation, the MSDD for the PZ increases faster than that for the DM. Scale bars = 50 μm in the left column.

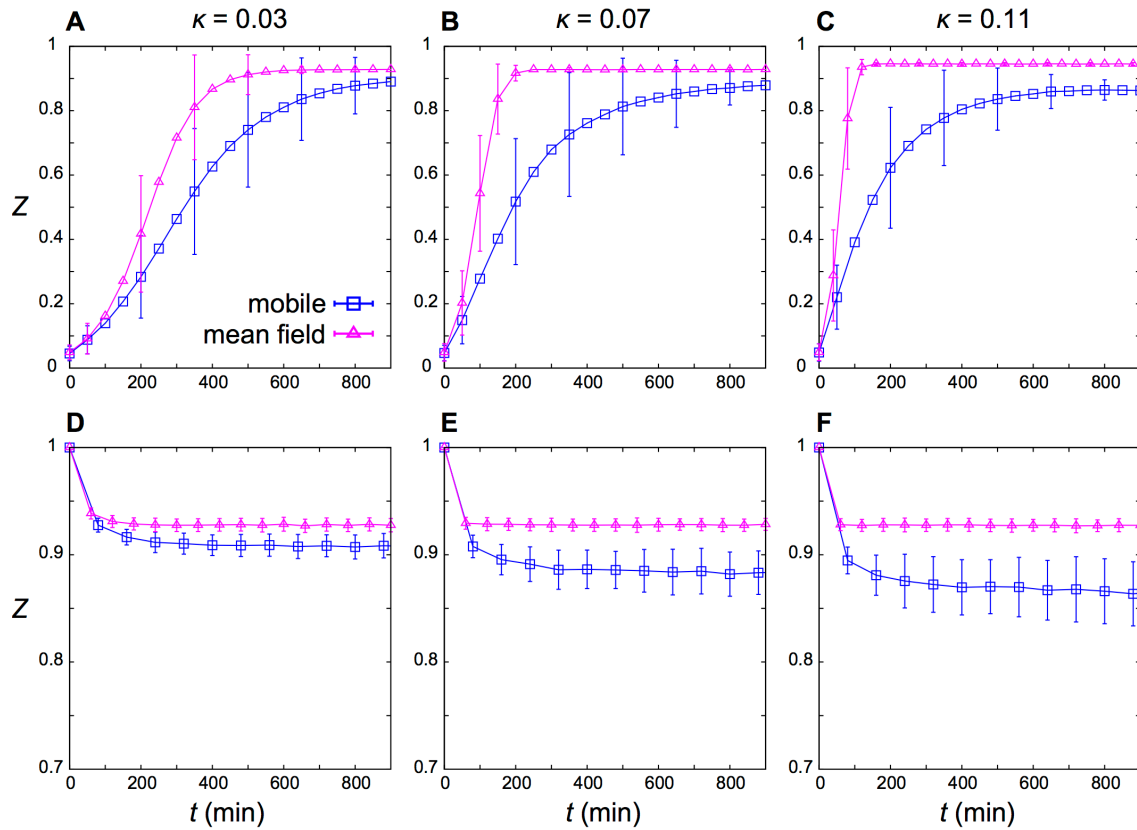


Figure S14 Comparison of synchronization dynamics between the mobile oscillator model Eqn 5 and a mean-field model Eqn S8.1. Time evolution of the phase order parameter Z from (A)-(C) random initial conditions and (D)-(F) the initial condition where all oscillators were completely synchronized ($Z(0) = 1$). (A),(D) $\kappa = 0.03$, (B),(E) 0.07 and (C),(F) 0.11 min^{-1} . For mobile oscillators, the parameter set for the tailbad in Fig. 2 in the main text was used. The number of oscillators in the simulations was same in the mobile oscillator and the mean-field models ($N = 346$). The standard deviation σ_ω for the frequency distribution was scaled as $\kappa = \sigma_\omega / \omega_0$ where ω_0 is the mean of the distribution. The noise intensity D_θ was also scaled as $D_\theta / \kappa = 1/10$. Average over 200 different realizations are plotted. The error bars indicate the standard deviations.

Table S1 Parameter values in the physical model of cell movement for the tailbuds.

	v_0	μ	D_ϕ	D_n	μ_b	γ	N
15ss (Figs. S6A and S12A)	1.27	4.91	0.06	0.303	25.7	0.09	330
16ss (Figs. S6B and S12B)	1.26	5.07	0.081	0.245	116.3	0.097	346
17ss (Figs. 2-4, and Figs. S9-S12, S14)	1.39	8.71	0.026	0.274	14	0.075	346
Fig. S8C	0.99	3.41	0.039	0.252	48	0.09	346
Fig. S8D	1.1	5.24	0.022	0.273	50.32	0.094	346
Fig. S8E	1.19	5.41	0.052	0.29	52	0.086	346
17ss (Figs. S6D and S12D)	1.35	5.68	0.052	0.33	73.1	0.115	389

See the supporting text for the definition of these parameters. The above values of v_0 are for simulations with mobile cells. For simulations with non-mobile cells in Figs. 4, S10, S11, and S12, the values of v_0 were reduced to 10% whereas all the other parameters were fixed as listed above. ss: somite-stage.

Table S2 Fixed parameter values in the physical model of cell movement.

Parameter	Definition (unit)	Value
L_x, L_y, L_z	domain length (μm)	60, 60, 60
d_c	cell diameter (μm)	11
ν	coefficient of boundary force ($\mu\text{m min}^{-1}$)	20
γ_b	lengthscale of boundary force (μm)	1
r_n	nuclear radius (μm)	3.8

These values are used in simulations throughout the article.

Table S3 Parameter values in the phase oscillator model.

	ω_0 (min^{-1})	σ_ω (min^{-1})	D_θ (min^{-1})	κ (min^{-1})	d_c (μm)
Fig. 4A-C	0.157	0.011	0.007	0.07	11
Figs. S8F and S12	0.157	0.011	0.007	0.07	11
Figs. S10, S11, S14	0.157	$\kappa \omega_0$	$\kappa/10$	0.01-0.11	11

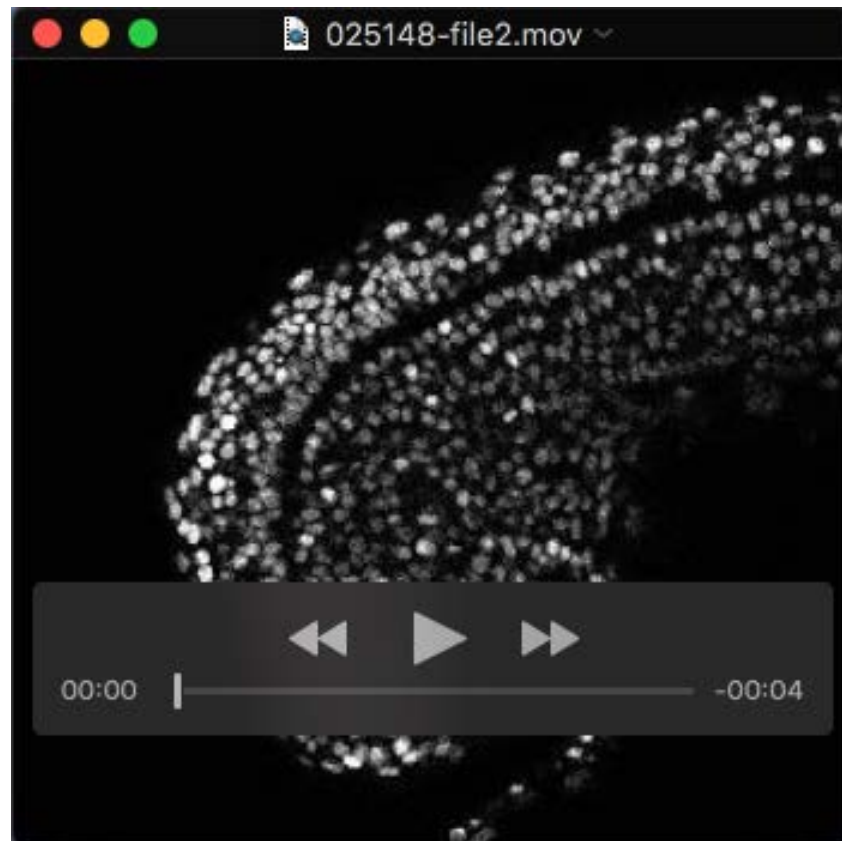
Table S4 Parameter values in the gradient vector diffusion algorithm.

Parameter	Value
α	0.01
β	0.03
F_T	18
R_s	6
q_0	0.01
σ	3

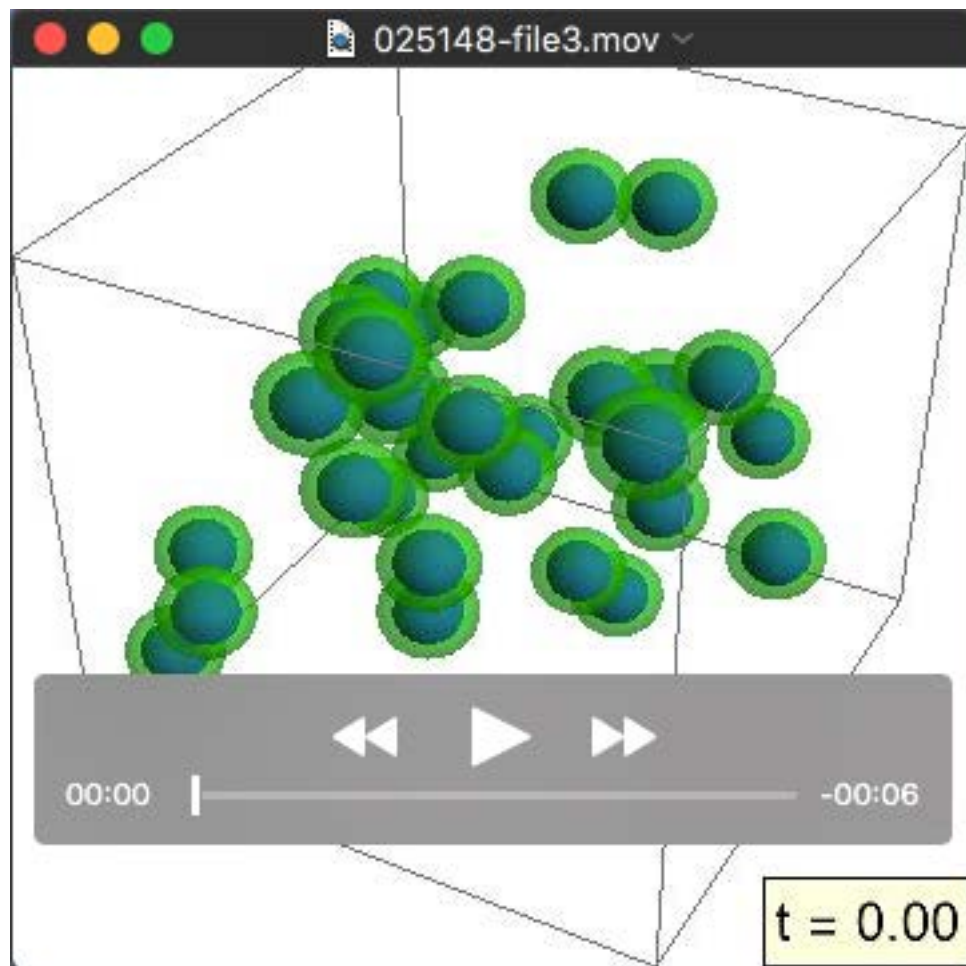
Table S5 Ranges of uniform distributions for each parameter in the prior distribution and the standard deviations of the Gaussians in the proposal distribution of parameters in ABC MCMC.

Parameter (unit)	min	max	σ_z
self-propulsion speed v_0 ($\mu\text{m}/\text{min}$)	0.1	1.5	0.07
coefficient of repulsive force μ ($\mu\text{m}/\text{min}$)	1	15	0.7
polarity noise strength D_ϕ (1/min)	0.01	0.1	0.0045
diffusion constant of the nucleus D_n ($\mu\text{m}^2/\text{min}$)	0.1	0.4	0.015
confinement force for the nucleus μ_b ($\mu\text{m}/\text{min}$)	10	120	5.5
lengthscale of the confinement force γ (μm)	0.06	0.5	0.0225

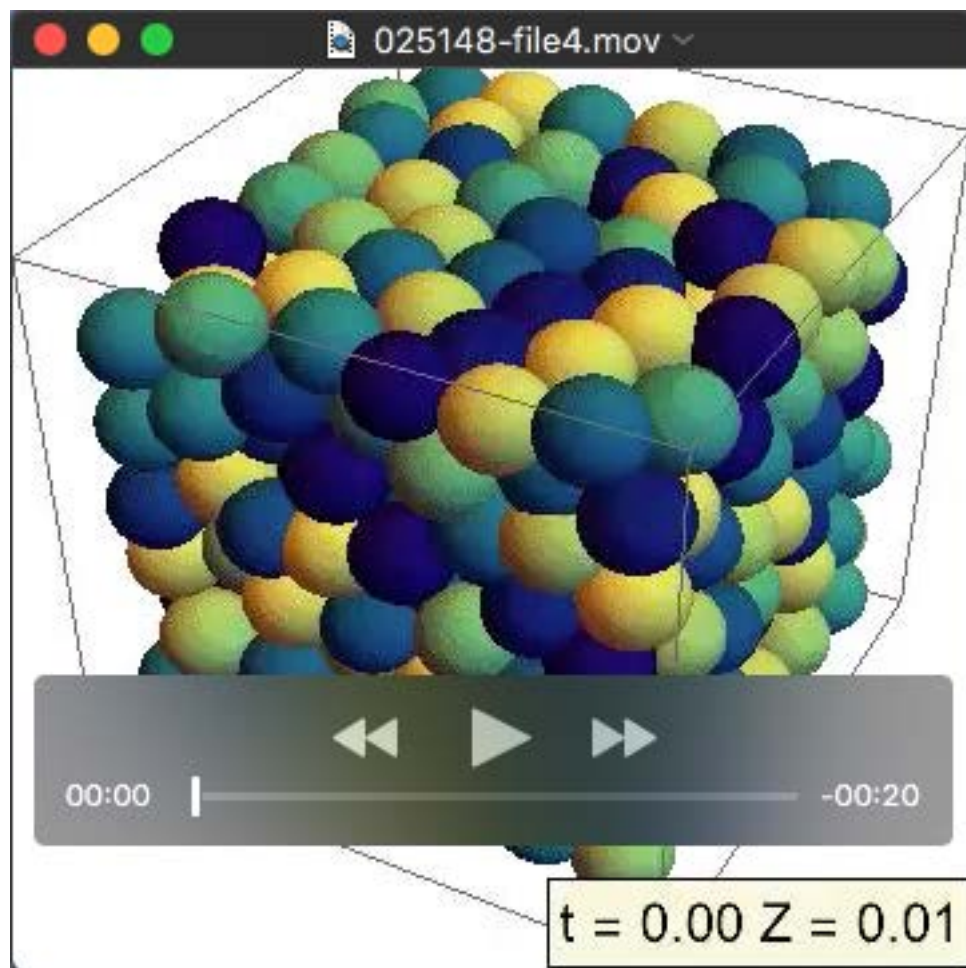
Movies



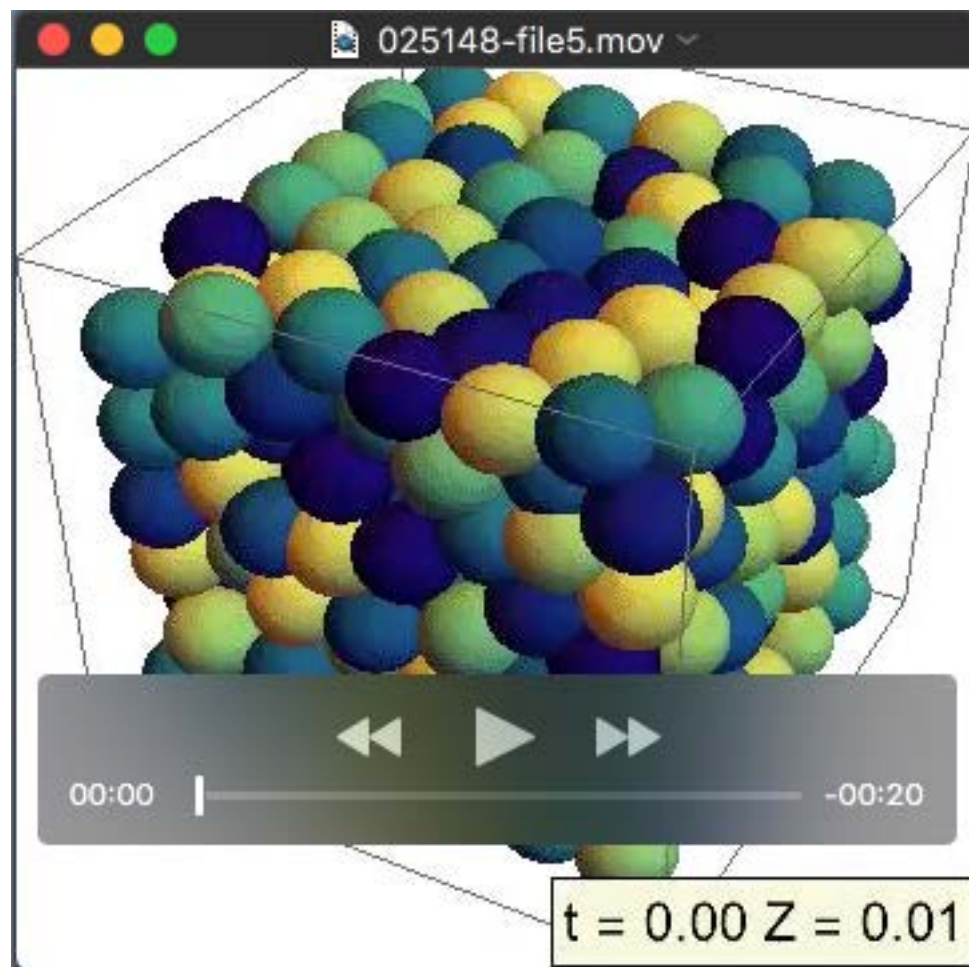
Movie 1 Time-lapse movie of the PSM and tailbud of the 17 somite stage embryo shown in Figs. 1 and 2. Slices of the stacks ($z = 18/24$) were used to make the Quick time movie file. The actual image size is $512 \times 512 \times 24$ voxels. The spatial resolution (voxel size) of the image is $0.692 \times 0.692 \times 1.75$ (μm^3). The frame interval is 0.83 min.



Movie 2 Simulation of the physical model of cell movement. Green color represents cell boundary and blue spheres represent cell nuclei. 30 cells out of 346 are plotted for visualization. A snapshot of this movie is shown in Fig. 3B. The unit of time (t) in the right bottom box is minutes.



Movie 3 Simulation of the coupled phase oscillator model in the absence of cell mixing $v_0 = 0.14$ ($\mu\text{m min}^{-1}$). The spheres represent cells and color code indicates the phase value for each cell. The unit of time (t) in the right bottom box is minutes. The variable Z indicates the phase order parameter defined by Eqn 6. In Movies 3 and 4, we started simulations from the same initial conditions for illustration.



Movie 4 Simulation of the coupled phase oscillator model in the presence of reproduced cell mixing $v_0 = 1.39 \text{ (}\mu\text{m min}^{-1}\text{)}$. The spheres represent cells and color code indicates the phase value for each cell. The unit of time (t) in the right bottom box is minutes. The variable Z indicates the phase order parameter defined by Eqn 6. The simulation was started from the same initial condition used in Movie 3.

Supporting Text

S1. Nucleus detection and cell tracking algorithm

To determine the positions of cell nuclei in an embryonic image, we used the gradient vector diffusion algorithm proposed by Li et al. (Li et al., 2007). The algorithm determines the positions of the center of each nucleus using the spatial intensity gradient in the image.

The basic idea of the gradient vector diffusion method is as follows. Since we stain cellular nuclei, there are spatial intensity gradient vectors pointing toward the center of each nucleus in an embryonic image. Sink points of the vector flows should, therefore, indicate the center of nuclei. However, due to noise in the image, original intensity gradient vectors often point in different directions from the centers of nuclei. The gradient vector diffusion method uses a partial differential equation to smooth and correct the direction of the intensity gradient vectors.

We briefly describe the algorithm. Let $I(\mathbf{x})$ be the intensity of an embryonic image at voxel position \mathbf{x} . We convolved a two-dimensional Gaussian $G_\sigma(\mathbf{x})$ with a standard deviation σ to each slice of a three-dimensional image stack $I(\mathbf{x})$ and obtained:

$$I_G(\mathbf{x}) \equiv G_\sigma(\mathbf{x}) * I(\mathbf{x}), \quad (\text{S1.1})$$

where the symbol $*$ indicates convolution. We computed the spatial gradient vector of the signal intensity $\nabla I_G(\mathbf{x})$ and defined a vector field:

$$\mathbf{u}(\mathbf{x}, 0) = \nabla I_G(\mathbf{x}), \quad (\text{S1.2})$$

where $\mathbf{u}(\mathbf{x}, 0)$ is the intensity gradient vector at integration time $\tau = 0$, that is the intensity gradient vector in the original embryonic image. Then we evolved the intensity gradient vector according to the following partial differential equation:

$$\frac{\partial \mathbf{u}(\mathbf{x}, \tau)}{\partial \tau} = \alpha \nabla^2 \mathbf{u} + (\alpha + \beta) \nabla \text{div}(\mathbf{u}) + q_v(\mathbf{x}) \{ \nabla I_G - \mathbf{u} \}, \quad (\text{S1.3})$$

where α and β are parameters. The function $q_v(\mathbf{x})$ was defined as in (Li et al., 2007):

$$q_v(\mathbf{x}) = \begin{cases} q_0, & |\nabla I_G(\mathbf{x})| > 0 \\ 0, & \text{otherwise.} \end{cases} \quad (\text{S1.4})$$

We used a reflecting boundary condition in numerical integrations of Eqn S1.3. The

partial differential equation Eqn S1.3 was discretized in space and time, and integrated with an explicit scheme as in (Li et al., 2007). We integrated the equation for 50 steps. The values of each parameter in the equation are listed in Table S4. Our embryonic images had anisotropic voxels where z resolution ($1.75 \mu\text{m}$) was lower than x and y resolution ($0.692 \mu\text{m}$). Since anisotropic voxels were not appropriate for the algorithm, we applied the third-order spline interpolation in z direction to obtain isotropic voxels as proposed in (Li et al., 2007) before solving Eqn S1.3.

To determine nuclear positions from the vector field $\mathbf{u}(\mathbf{x})$ after integration, we detected sink points of the vector flows by extending the algorithm in (Li et al., 2007) into three-dimensional space. We first normalized $\mathbf{u}(\mathbf{x})$ at each spatial point to obtain a unit vector field:

$$\tilde{\mathbf{u}}(\mathbf{x}) \equiv \mathbf{u}(\mathbf{x}) / \|\mathbf{u}(\mathbf{x})\|. \quad (\text{S1.5})$$

Then, we measured an outward flux from the position \mathbf{x} by:

$$Flux(\mathbf{x}) = \sum_{i=1}^{26} \mathbf{N}_i \cdot \tilde{\mathbf{u}}(\mathbf{x}_i), \quad (\text{S1.6})$$

where \mathbf{x}_i is the position of the neighboring voxels of \mathbf{x} and \mathbf{N}_i is the outward normal vector at position \mathbf{x}_i on a sphere centered at \mathbf{x} . The number of neighboring voxels in the bulk is 26. Note that $Flux(\mathbf{x}) < 0$ at the sink points. Then, we introduced a threshold F_T and if

$$-Flux(\mathbf{x}) \geq F_T > 0, \quad (\text{S1.7})$$

we considered \mathbf{x} as a sink point. If we found two spatial points that satisfied Eqn S1.7 and whose spatial distance was less than a threshold R_s , we chose the one that had the larger value of $|Flux(\mathbf{x})|$ as a sink point.

Cell tracking. For cell tracking we applied a trajectory linking algorithm (Sbalzarini and Koumoutsakos, 2005). Briefly, let \mathbf{p}_i be the position of a detected nucleus at time frame t ($i = 1, 2, \dots, N_t$). Let \mathbf{q}_j be the position of a detected nucleus at time frame $t+1$ ($j = 1, 2, \dots, N_{t+1}$). The algorithm defines an association matrix of the size $(N_t + 1) \times (N_{t+1} + 1)$:

$$G^t(i, j) = g_{ij} \equiv \begin{cases} 1 & \text{if } \mathbf{p}_i \text{ at } t \text{ and } \mathbf{q}_j \text{ at } t+1 \text{ are the same nucleus,} \\ 0 & \text{otherwise.} \end{cases} \quad (\text{S1.8})$$

g_{i0} are for nuclei that are present at the frame t and disappear at the frame $t+1$. g_{0j} are for nuclei that newly appear at the frame $t+1$.

To determine the values of elements g_{ij} , the algorithm defines the cost functional:

$$\Phi = \sum_{i=0}^{N_t} \sum_{j=0}^{N_{t+1}} \psi_{ij} g_{ij}, \quad (\text{S1.9})$$

where we set

$$\psi_{ij} = \left(x_{p_i} - x_{q_j}\right)^2 + \left(y_{p_i} - y_{q_j}\right)^2 + \left(z_{p_i} - z_{q_j}\right)^2, \quad (\text{S1.10})$$

which is the squared distance between the nuclear positions \mathbf{p}_i and \mathbf{q}_j for $i, j > 0$. Hence, minimizing Φ with respect to g_{ij} means nearest neighbor linking between a point at t and a point at the next frame $t+1$. If we could not find any nuclei at time frame $t+1$ within a sphere with radius $4 \mu\text{m}$ centered at \mathbf{p}_i , we considered that we lost the nucleus at $t+1$ and set $g_{i0} = 1$ and $\psi_{i0} = 4^2$. Similarly, if we could not find any nuclei at time t within a sphere with radius $4 \mu\text{m}$ centered at \mathbf{q}_j , we considered that the nucleus newly appears at $t+1$ and set $g_{0j} = 1$ and $\psi_{0j} = 4^2$. By minimizing Φ with respect to g_{ij} we linked the nuclei at time frame t to those at $t+1$. For minimization we used the optimization algorithm proposed in (Sbalzarini and Koumoutsakos, 2005).

S2. Validation of nucleus detection and cell tracking

In this section we first calibrate the parameters in the gradient vector diffusion algorithm with synthetic images and then verify tracking accuracy using transplanted embryos (Bhavna et al., 2016).

Calibration with synthetic images. The gradient vector diffusion algorithm Eqn S1.3 includes three key parameters, α , β and q_0 . We calibrated these parameters using synthetic images that have similar properties to the embryonic images such as the average size of nucleus, its density and intensity fluctuations within a nucleus. See the reference (Bhavna et al., 2016) for generation of synthetic images. In the following analysis we fixed $q_0 = 0.01$ in Eqn S1.4 and changed the values of α and β . Values of the other parameters were also fixed and they are listed in Table S4.

For parameter calibration, we defined sensitivity and precision (Bhavna et al., 2016). Sensitivity was defined as the ratio of the number of correctly detected objects by the algorithm to the true number of objects in a synthetic image. Precision was defined as the ratio of the number of correctly detected objects to the total number of detected objects. For matching the positions of detected objects and those of ground truth data set, we applied the particle matching algorithm used in cell tracking as described in the previous section.

Fig. S1A shows the dependence of sensitivity and precision on the parameters α and β in Eqn S1.3. For each object density shown in Fig. S1A, we generated five different synthetic images ($100 \times 100 \times 25$ voxels; $69.2 \times 69.2 \times 43.75 \mu\text{m}^3$) where the spatial configuration of objects was different. The signal-to-noise ratio (SNR) in the synthetic images was fixed as $\text{SNR} = 5$. We computed average sensitivity and precision over these five images in Fig. S1A. Sensitivity was higher when values of both α and β were smaller (Fig. S1A). As the values of these two parameters increased, sensitivity decreased. In contrast, when both α and β were small, the precision became small especially in the low object density (Fig. S1A). Precision was high when α was small while β was large. A higher precision would be more important than a higher sensitivity to avoid artifacts in cell tracking. Therefore, we concluded that combination of a smaller α and a larger β gave a good combination of sensitivity and precision. In the main text and the following analysis, we fixed $\alpha = 0.01$ and $\beta = 0.03$ (filled circles in Fig. S1A). With this parameter set, sensitivity was about 0.9 and precision was 0.98 over the relevant object density (from 1×10^{-3} to $3 \times 10^{-3} \mu\text{m}^{-3}$; Fig. S1A) in the synthetic images.

Validation with transplanted embryos. To validate the algorithm in living tissues we used transplanted chimeric embryos as previously proposed in (Bhavna et al., 2016). A few cells carrying both mCherry-tagged and GFP-tagged Histones as nuclear labels were transplanted at blastula stage to host embryos carrying only GFP-tagged Histones. Detecting these transplanted cells is easier in the mCherry channel (sparse channel) because the density of these transplanted cells was low, while detecting them in the GFP channel (dense channel) was more difficult. Thus, the results for the sparse channel can be considered as a ground truth data set. By comparing the detected positions of the

transplanted cells in the two channels, we evaluate the sensitivity of the algorithm in living embryos. See (Bhavna et al., 2016) for more details.

We had four chimeric embryos (one embryo at 15 somite stage (ss), one embryo at 16 ss and two embryos at 17 ss). In the 15 ss embryo, the transplanted cells in the PSM were almost absent, so we used the other three embryos for the validation of gradient vector diffusion and tracking algorithms. We set a three-dimensional box of the size $70 \times 70 \times z$ μm^3 ($z = 61$ for the 16 ss embryo and $z = 42$ for the two 17 ss embryos) in the posterior PSM and validated the algorithms using the nuclei in the box. For the nuclear detection in the sparse channel we used $\alpha = 0.01$ and $\beta = 0.04$ to attain better precision at a lower nuclear density (Fig. S1A).

If the algorithm detected a nucleus in the dense channel within a distance of $2 \mu\text{m}$ from a nucleus in the sparse channel, we considered that the algorithm could detect the transplanted cell in the dense channel correctly. We defined sensitivity as the ratio of the number of detected transplanted nuclei in the dense channel to the total number of transplanted nuclei in the sparse channel within the box. The algorithm could detect transplanted cells in the dense channel with sensitivity of 0.97 on average (Fig. S1B). We also confirmed that the dependence of sensitivity on the parameters α and β in Eqn S1.3 for the transplanted embryos was similar to that observed for the synthetic images shown in Fig. S1A.

Subsequently, we tested the accuracy of trajectory linking using the transplanted embryos (Fig. S1C-E). We first obtained full-length trajectories of transplanted cells in the sparse channel and considered them as the ground truth data set (the red trajectories in Fig. S1C). Then, we compared the corresponding trajectories in the dense channel (the green trajectories in Fig. S1C). A similar validation was used in a previous study (Lawton et al., 2013).

We classified trajectories into three categories: 1) the distance between the trajectories in the dense and sparse channels is less than $2 \mu\text{m}$ at all time frames, 2) the distance is larger than $2 \mu\text{m}$ but less than $4 \mu\text{m}$, and 3) the distance is larger than $4 \mu\text{m}$ (Fig. S1C). Trajectories in the third category were obviously caused by incorrect linking (Fig. S1C).

However, the fraction of this third category was very small (Fig. S1D). Occasionally, the tracking algorithm lost cells in the middle of the movie in the dense channel, perhaps due to under-segmentation. However, these shorter trajectories would not cause any artifacts in movement statistics in later analysis. Hence, we included these shorter trajectories into one of above three categories depending on the distances from sparse ones. When we obtained full-length trajectories in the sparse channel, about 80% of them were obtained as full-length trajectories in the dense channel as well (Fig. S1E).

S3. Quantification of tissue parameters

To constrain the values of parameters in the physical model for cell movement in the main text we measured key tissue parameters. We first measured the nuclear density across the PSM using the nuclear position data. We set boxes of the size $42 \times 42 \times 20 \mu\text{m}^3$ in different regions across the PSM (white boxes in the left panels of Fig. S7) and counted the number of nuclei within each box. To fill the entire region of each box with cells the boxes were located $20 \mu\text{m}$ inside the PSM, away from the epidermal tissue. The nuclear density was defined as the number of nuclei in a unit volume $1 \mu\text{m}^3$. Fig. S7 shows the spatial distribution of the nuclear density across the PSM of the four embryos. The nuclear density changed nonmonotonically along the anterior-posterior axis of the PSM. The density was slightly lower at the most anterior region where the next somite would be formed. The density increased toward the posterior PSM but it decreased again near the boundary between the PSM and tailbud. The tailbud had a higher nuclear density. These tendencies could consistently be observed in all four embryos examined at the similar developmental stage (Fig. S7). The average nuclear density over the four embryos in the tailbud in Figs. 2 and S6 was $1.61 \times 10^{-3} \pm 8.63 \times 10^{-5} \mu\text{m}^{-3}$.

To check the statistical significance of the observed variation of nuclear density, we applied the one-tailed t-test between the most anterior region (box 1) and the tailbud region (box 5 of the 15 ss embryo in A and box 6 of the other three embryos) in Fig. S7. We pooled data for the four embryos by assuming that these data are samples from the same population. We observed statistical significance of nuclear density difference between these two regions at $p < 0.01$. However, a more careful experimental setting would be required to further investigate distribution of nuclear density at a higher spatial resolution, which is out of the scope of the current study.

Next we estimated the size of cells in the tailbud (Fig. S2A). We interpreted the distance between two neighboring nuclei as a characteristic size of cells. To define a neighboring relation for cells from nuclear positions, we applied the three dimensional Voronoi tessellation to the nuclear position data. We measured the distance between a pair of nuclei that are neighbors in a 3D Voronoi diagram. The histogram of the distances had a clear peak (Fig. S2A). Its median was about 11.2 μm for cells in the tailbud, which we considered as a typical diameter of cells. We obtained similar median values for all four embryos. We also applied this method to the cells in anterior regions of the PSM. The average value of the median of distance distribution over the four embryos was slightly larger ($\sim 11.8 \mu\text{m}$) in anterior region, but we could not detect significant difference by t-test between the anterior and posterior PSM.

We also measured the length of the long axis of nuclei (Fig. S2B). We determined the long axis of a nucleus in the sparse channel within an x - y plane after visually scanning through the z direction (Fig. S2B). The average half-length of the long axis of 78 nuclei in the posterior PSM was $3.83 \pm 0.51 \mu\text{m}$.

S4. Quantification of relative cell movement by the strain rate tensor

In the main text we used directional derivative of velocity vectors to quantify relative cell movement. Another approach would be to use the strain rate tensor after constructing a cell flow field. We computed the strain rate tensor to quantify relative cell movement in the PSM and tailbud. Here we first note the reason why we chose to use the strain rate tensor. Then, we describe results of the strain rate tensor for the embryonic tissues.

From cell tracking we obtained cellular velocities in the PSM and tailbud. Using the velocity data we constructed a continuum velocity vector field with the smoothed particle hydrodynamics (SPH) (Liu et al., 2003) described in the next section. Then, we examined the resulting flow field using methods from fluid mechanics.

In this section we denote $\mathbf{x} = (x, y, z) = (x_1, x_2, x_3)$ for notational simplicity. Let us

consider two tracer points at position \mathbf{x} and $\mathbf{x} + \Delta\mathbf{x}$ ($|\Delta\mathbf{x}| \ll 1$) in a velocity vector field. Their velocities are denoted as $\mathbf{v}(\mathbf{x})$ and $\mathbf{v}(\mathbf{x} + \Delta\mathbf{x})$, respectively. The relative positional vector between them is $\Delta\mathbf{x}$. After short time Δt , their positions change as $\mathbf{x} + \mathbf{v}(\mathbf{x})\Delta t$ and $\mathbf{x} + \Delta\mathbf{x} + \mathbf{v}(\mathbf{x} + \Delta\mathbf{x})\Delta t$. Then, a relative positional vector $\Delta\mathbf{x}'$ between these two points is:

$$\begin{aligned}\Delta\mathbf{x}' &= \mathbf{x} + \Delta\mathbf{x} + \mathbf{v}(\mathbf{x} + \Delta\mathbf{x})\Delta t - \{\mathbf{x} + \mathbf{v}(\mathbf{x})\Delta t\} \\ &= \Delta\mathbf{x} + \{\mathbf{v}(\mathbf{x} + \Delta\mathbf{x}) - \mathbf{v}(\mathbf{x})\}\Delta t \\ &\approx \Delta\mathbf{x} + (\partial\mathbf{v}(\mathbf{x})/\partial\mathbf{x})\Delta\mathbf{x}\Delta t,\end{aligned}\quad (\text{S4.1})$$

where we expanded $\mathbf{v}(\mathbf{x} + \Delta\mathbf{x})$ and neglected the higher order terms in the second line as:

$$\mathbf{v}(\mathbf{x} + \Delta\mathbf{x}) \approx \mathbf{v}(\mathbf{x}) + (\partial\mathbf{v}(\mathbf{x})/\partial\mathbf{x})\Delta\mathbf{x}. \quad (\text{S4.2})$$

The matrix $(\partial\mathbf{v}(\mathbf{x})/\partial\mathbf{x})_{ij} = \partial v_i(\mathbf{x})/\partial x_j$ is called the velocity gradient tensor. Then, we

separate the velocity gradient tensor into the symmetric and anti-symmetric parts:

$$\partial\mathbf{v}(\mathbf{x})/\partial\mathbf{x} = \mathbf{S}(\mathbf{x}) + \mathbf{A}(\mathbf{x}), \quad (\text{S4.3})$$

where $S_{ij} = \frac{1}{2}\left(\frac{\partial v_i}{\partial x_j} + \frac{\partial v_j}{\partial x_i}\right)$ and $A_{ij} = \frac{1}{2}\left(\frac{\partial v_i}{\partial x_j} - \frac{\partial v_j}{\partial x_i}\right)$. The symmetric tensor \mathbf{S} is called

strain rate tensor and the anti-symmetric tensor \mathbf{A} is called spin tensor. By substituting Eqn S4.3 into Eqn S4.1 we obtain:

$$\Delta\mathbf{x}' \approx \Delta\mathbf{x} + \mathbf{S}\Delta\mathbf{x}\Delta t + \mathbf{A}\Delta\mathbf{x}\Delta t. \quad (\text{S4.4})$$

Now we consider the change in the squared length after Δt :

$$\Delta l^2 \equiv |\Delta\mathbf{x}'|^2 - |\Delta\mathbf{x}|^2. \quad (\text{S4.5})$$

By substituting Eqn S4.4 into Eqn S4.5:

$$\begin{aligned}\Delta l^2 &= |\Delta\mathbf{x}'|^2 - |\Delta\mathbf{x}|^2 \\ &= |\Delta\mathbf{x} + \mathbf{S}\Delta\mathbf{x}\Delta t + \mathbf{A}\Delta\mathbf{x}\Delta t|^2 - |\Delta\mathbf{x}|^2 \\ &= 2 \sum_{i,j} S_{ij} \Delta x_i \Delta x_j \Delta t + O(\Delta x_i \Delta x_j \Delta t^2) \\ &\approx 2\Delta\mathbf{x}^T \mathbf{S} \Delta\mathbf{x} \Delta t.\end{aligned}\quad (\text{S4.6})$$

In the last line of Eqn S4.6 we neglected the higher order terms. Thus, the change in the

distance between the two tracer points is a function of the strain tensor S . Note that the spin tensor A is related to the rotation of the relative positional vector $\Delta \mathbf{x}$ without changing its length. Since we are interested in relative cell movement that causes neighbor exchanges, we consider the strain rate tensor \dot{S} as the relevant quantity.

To compute spatial derivatives of cell velocity vectors, a continuum vector field is required. We obtained it from discrete velocity vector fields obtained from cell tracking data by using SPH (Liu et al., 2003) introduced in the next section.

Because the matrix representation of the strain rate tensor depends on a spatial coordinate system we chose arbitrarily, we computed the eigenvalues λ_i ($i = 1, 2, 3$; $|\lambda_1| \geq |\lambda_2| \geq |\lambda_3|$) that are rotationally invariant. We then defined the norm $|\lambda| \equiv \sqrt{\lambda_1^2 + \lambda_2^2 + \lambda_3^2}$ and considered it as a quantity for the magnitude of cell mixing. If the norm $|\lambda|$ was large, the magnitude of cell mixing was considered to be higher.

Fig. S4 shows spatial profiles of the norm $|\lambda|$ along the anterior-posterior axis of the PSMs for the four embryos. We computed $|\lambda|$ in the three-dimensional tissue and for visualization we projected values of $|\lambda|$ in the z direction into the two-dimensional x - y plane by maximum projection. We confirmed the same overall tendency of the spatial profiles in different projection methods. There is a spatial gradient of $|\lambda|$ in the PSM higher in the posterior region than in the anterior region (Fig. S4). The magnitude was highest in the tailbud region, suggesting the presence of cell mixing in that region. This observation is consistent with the results of the directional derivative modulus of velocity vectors in the main text (Fig. 1C). The norm $|\lambda|$ was also higher in the connecting tissue between the embryo and the yolk where a large tissue deformation could be observed. Thus, using the strain rate tensor, we determined the region in the PSM where cell mixing occurred.

Note that we might under-estimate the magnitude of local velocity variations with the strain rate tensor. Because of the presence of spontaneous cell movement, the velocity vector field in the tailbud would tend to be more random than in other parts of tissues. The random vector field may suffer stronger spatial smoothing in the SPH, resulting in

smaller modulus of velocity vectors. Perhaps this is why we observe larger values of the norm $|\lambda|$ in the connecting tissue than in the tailbud in Fig. S4, while we observe larger values of directional derivative modulus of velocity vectors in the tailbud than in the connecting tissue in Fig. 1C in the main text and Fig. S3.

S5. Smoothed particle hydrodynamics

We used the smoothed particle hydrodynamics (SPH) approach to construct a continuum velocity vector field from cell tracking data. A previous study applied this method to cell velocity data obtained in the zebrafish PSM (Lawton et al., 2013). Here we describe the SPH and our parameter settings, the interested reader is referred to (Liu et al., 2003) for a more detailed explanation of SPH.

The SPH spatially interpolates velocity vectors using a smoothing kernel by the following equation:

$$\mathbf{v}(t, \mathbf{x}) = \int W(\mathbf{x} - \mathbf{x}'; h) \mathbf{v}(t, \mathbf{x}') d\mathbf{x}', \quad (\text{S5.1})$$

where $W(\mathbf{x} - \mathbf{x}'; h)$ is the smoothing kernel with the length scale h for smoothing. The smoothing kernel has the properties $\int W(\mathbf{x} - \mathbf{x}'; h) d\mathbf{x}' = 1$ and $W(\mathbf{x} - \mathbf{x}'; h) \rightarrow \delta(\mathbf{x} - \mathbf{x}')$ as $h \rightarrow 0$. In our case, we have the data for velocity vectors $\mathbf{v}(t, \mathbf{x}_i)$ for cell i at position \mathbf{x}_i ($i = 1, 2, \dots, N$). Eqn S5.1 can be discretized by replacing the volume element in the integral with the volume of cells $d\mathbf{x}' \approx M_j / \hat{\rho}_j$ as:

$$\mathbf{v}(t, \mathbf{x}) \approx \sum_{j=1}^N \mathbf{v}(t, \mathbf{x}_j) \frac{M_j}{\hat{\rho}_j} W(\mathbf{x} - \mathbf{x}_j; h), \quad (\text{S5.2})$$

where M_j is the mass of cell j and $\hat{\rho}_j$ is the density of cell mass $\hat{\rho}_j = M_j / V_j$ with the volume V_j . We assumed $M = M_1 = \dots = M_N$ and applied the SPH for the density of cell mass:

$$\begin{aligned} \hat{\rho}(\mathbf{x}_j) &\approx \sum_{k=1}^N \hat{\rho}(\mathbf{x}_k) \frac{M_k}{\hat{\rho}(\mathbf{x}_k)} W(\mathbf{x}_j - \mathbf{x}_k; h) \\ &= M \sum_{k=1}^N W(\mathbf{x}_j - \mathbf{x}_k; h). \end{aligned} \quad (\text{S5.3})$$

Substituting $\hat{\rho}(\mathbf{x}_j)$ in Eqn S5.3, Eqn S5.2 reads:

$$\mathbf{v}(t, \mathbf{x}) \approx \sum_{j=1}^N \mathbf{v}(t, \mathbf{x}_j) \frac{W(\mathbf{x} - \mathbf{x}_j; h)}{\sum_{k=1}^N W(\mathbf{x}_k - \mathbf{x}_j; h)}. \quad (\text{S5.4})$$

The spatial derivative of $\mathbf{v}(t, \mathbf{x})$ can be computed as:

$$\partial \mathbf{v}(t, \mathbf{x}) / \partial x_i \approx \sum_{j=1}^N \mathbf{v}(t, \mathbf{x}_j) \frac{\partial W(\mathbf{x} - \mathbf{x}_j; h) / \partial x_i}{\sum_{k=1}^N W(\mathbf{x}_k - \mathbf{x}_j; h)}. \quad (\text{S5.5})$$

We chose the smoothing kernel by following the previous study (Lawton et al., 2013):

$$W(\mathbf{x} - \mathbf{x}_j; h) = C_d \begin{cases} \frac{2}{3} - \frac{9}{8} \left(\frac{|\mathbf{x} - \mathbf{x}_j|}{h} \right)^2 + \frac{19}{24} \left(\frac{|\mathbf{x} - \mathbf{x}_j|}{h} \right)^3 - \frac{5}{32} \left(\frac{|\mathbf{x} - \mathbf{x}_j|}{h} \right)^4, & 0 \leq \frac{|\mathbf{x} - \mathbf{x}_j|}{h} \leq 2 \\ 0, & 2 < \frac{|\mathbf{x} - \mathbf{x}_j|}{h} \end{cases} \quad (\text{S5.6})$$

with the normalization constant $C_d = 315\pi h^3/208$. The parameter h sets the length scale of the smoothing kernel. We examined the dependence of eigenvalues of the strain rate tensor on the parameter h . The overall qualitative tendencies of the spatial profile of $|\lambda|$ did not strongly depend on the values of h and similar profiles to those shown in Fig. S4 could be obtained. When the value of h was smaller, local variations of velocity vectors were preserved and the norm $|\lambda|$ of the eigenvalues of the strain rate tensor was larger. However, its spatial profile was noisier due to less smoothing. Hence, we chose to focus on the relative changes in velocity vectors that remained even under the smoothing with a relatively larger h . In Fig. S4, we used $h = 15 \mu\text{m}$. A previous study used a similar value of h (Lawton et al., 2013).

S6. Physical model of cell movement

In this section, we describe the physical model of cell movement that we use to fit the data. The model includes the movement of both cells and nuclei. The model was tailored to allow a straightforward comparison of relative cell movement and phase dynamics timescales.

Cell movement. Cells were represented as spheres of diameter d_c in a three-dimensional space $L_x \times L_y \times L_z$ (Fig. 3A). The three dimensional domain $L_x \times L_y \times L_z$ represents a local region somewhere in the PSM or in the tailbud. The number of cells N in the

model was constant and set so that the cell density $\rho = N/(L_x L_y L_z)$ was the same as observed in embryos (Fig. S7 and section S3 of the supporting text). For simplicity, we did not consider cell proliferation and apoptosis in the model. In embryonic tissue cells divide, flow into the tailbud from adjacent tissues, rearrange by convergent extension, and flow out from the tailbud into the PSM. Inclusion of these more complex tissue processes will set other timescales in the physical model. Modeling the influx and outflux of cells in the tailbud, as well as cell divisions would be an interesting avenue for future work.

Let $\mathbf{x}_i(t)$ be the position of the center of cell i ($i = 1, 2, \dots, N$) at time t . The over-damped equation of motion for the cell center in the main text is:

$$\frac{d\mathbf{x}_i(t)}{dt} = v_0 \mathbf{n}_i(t) + \mu \sum_{\substack{j=1 \\ j \neq i}}^N \mathbf{F}(\mathbf{x}_i, \mathbf{x}_j) + \mathbf{F}_b(\mathbf{x}_i), \quad (\text{Eqn 4 in the main text}) \quad (\text{S6.1})$$

where v_0 is the self-propulsion speed, $\mathbf{n}_i = (\sin\phi_i \cos\varphi_i, \sin\phi_i \sin\varphi_i, \cos\phi_i)$ is a unit vector representing the polarity of spontaneous cell movement in spherical coordinates (Fig. 3A), μ is a coefficient giving the relative strength of intercellular forces, $\mathbf{F}(\mathbf{x}_i, \mathbf{x}_j)$ is a physical force between cells i and j , and \mathbf{F}_b is the confinement force exerted by the boundary of the domain.

In the absence of forces, cell i moves spontaneously in the direction of cell polarity \mathbf{n}_i at speed v_0 . For simplicity, we model the dynamics of the polarity angles ϕ_i and φ_i of the unit vector \mathbf{n}_i as a diffusion processes:

$$\frac{d\phi_i(t)}{dt} = \frac{D_\phi}{\tan\phi_i} + \sqrt{2D_\phi} \xi_i(t), \quad (\text{S6.2a})$$

$$\frac{d\varphi_i(t)}{dt} = \frac{\sqrt{2D_\phi}}{\sin\phi_i} \zeta_i(t), \quad (\text{S6.2b})$$

where D_ϕ is the polarity noise strength and $\xi_i(t)$ and $\zeta_i(t)$ are white Gaussian noises satisfying $\langle \xi_i(t) \rangle = 0$, $\langle \zeta_i(t) \rangle = 0$, $\langle \xi_i(t) \xi_j(t') \rangle = \delta_{ij} \delta(t - t')$, $\langle \zeta_i(t) \zeta_j(t') \rangle = \delta_{ij} \delta(t - t')$ and $\langle \xi_i(t) \zeta_j(t') \rangle = 0$. Under these two stochastic equations, the polarity vector \mathbf{n}_i performs random walk on a unit sphere with diffusion constant D_ϕ . Accordingly, in the absence of forces, cells move at instantaneous speed $d\mathbf{x}_i/dt = v_0 \mathbf{n}_i(t)$ with a characteristic auto-correlation time $\sim 1/(2D_\phi)$. The deterministic term $D_\phi/\tan\phi_i$ in Eqn S6.2a is required

for the isotropic diffusion of \mathbf{n}_i on a unit sphere, as described in spherical coordinates.

For the physical force $\mathbf{F}(\mathbf{x}_i, \mathbf{x}_j)$ between two cells we considered a volume exclusion effect (Fig. 3A). Two cells at a distance closer than the cell diameter d_c repel each other. This is modeled as a linear repulsive force $\mathbf{F}(\mathbf{x}_i, \mathbf{x}_j) = F(\mathbf{x}_i, \mathbf{x}_j)\mathbf{e}_{ij}$, with $\mathbf{e}_{ij} = (\mathbf{x}_j - \mathbf{x}_i) / |\mathbf{x}_j - \mathbf{x}_i|$ and magnitude

$$F(\mathbf{x}_i, \mathbf{x}_j) = \begin{cases} r_{ij}/d_c - 1 & r_{ij} \leq d_c \\ 0 & r_{ij} > d_c, \end{cases} \quad (\text{S6.3})$$

where $r_{ij} = |\mathbf{x}_j - \mathbf{x}_i|$.

Cells were confined within the domain $L_x \times L_y \times L_z$ by boundary forces

$$\mathbf{F}_b(\mathbf{x}_i) = (F_{bx}(\mathbf{x}_i), F_{by}(\mathbf{x}_i), F_{bz}(\mathbf{x}_i)). \quad (\text{S6.4})$$

We described this confinement force as:

$$F_{bw}(\mathbf{x}_i) = \begin{cases} \nu e^{-w/\gamma_b} & w \leq L_w/2, \\ -\nu e^{-(L_w-w)/\gamma_b} & w > L_w/2, \end{cases} \quad (\text{S6.5})$$

where $w \in \{x, y, z\}$, ν is the coefficient of boundary force and γ_b is its length scale ($\gamma_b/L_w \ll 1$).

Nuclear movement. Since we tracked cell nuclei in embryonic imaging data, we explicitly model nuclear movement inside a cell to account for its contribution to the MSDD (Fig. 3A). Each nucleus is represented as a sphere with the radius r_n , ($0 \leq r_n < d_c/2$). Let $\mathbf{q}_i(t)$ be the position of the nucleus for cell i at time t and $\Delta\mathbf{q}_i(t)$ be the relative nuclear position from the cell center $\mathbf{x}_i(t)$. A nucleus stays inside a cell as described by $0 \leq |\Delta\mathbf{q}_i| < d_c/2 - r_n$. $\mathbf{q}_i(t)$ can then be written as $\mathbf{q}_i(t) = \mathbf{x}_i(t) + \Delta\mathbf{q}_i(t)$. We assumed that the movement of the cell nucleus was random in the cytoplasmic region:

$$\frac{d\Delta\mathbf{q}_i}{dt} = \mathbf{f}(\Delta\mathbf{q}_i) + \sqrt{2D_n}\boldsymbol{\eta}_i(t), \quad (\text{S6.6})$$

where \mathbf{f} represents the confinement force on the nucleus exerted by the cell boundary, D_n is the diffusion constant of the nucleus and $\boldsymbol{\eta}_i = (\eta_{ix}, \eta_{iy}, \eta_{iz})$ is a three dimensional vector of white Gaussian noise with $\langle \eta_{ia}(t) \rangle = 0$ and $\langle \eta_{ia}(t) \eta_{jb}(t') \rangle = \delta_{ij} \delta_{ab} \delta(t - t')$ ($a, b \in \{x, y, z\}$).

$y, z\}$). We describe the magnitude of the nuclear confinement force by an exponential function of $\Delta\mathbf{q}_i(t)$:

$$\mathbf{f}(\Delta\mathbf{q}_i) = -\mu_b \exp\left[\frac{-(d_c - 2|\Delta\mathbf{q}_i| - 2r_n)}{2\gamma}\right] \frac{\Delta\mathbf{q}_i}{|\Delta\mathbf{q}_i|}, \quad (\text{S6.7})$$

where μ_b is the coefficient of the confinement force, γ is the length scale of the force and $-\Delta\mathbf{q}_i/|\Delta\mathbf{q}_i|$ is the vector pointing towards the cell center. By setting this confinement force strong enough ($\sqrt{2D_n}/\mu_b \ll 1$), the nucleus stayed inside of the cell $0 \leq |\Delta\mathbf{q}_i| < d_c/2 - r_n$.

S7. Approximate Bayesian Computation

To fit the physical model of cell movement to experimentally obtained mean squared difference of displacement vectors (MSDD), we used the Approximate Bayesian Computation based on Markov Chain Monte Carlo (ABC MCMC; (Marjoram et al., 2003)). The physical model described in the section S6 has six free parameters, the self-propulsion speed v_0 , repulsive force coefficient μ , polarity noise strength D_ϕ , diffusion constant of the nucleus D_n , nucleus confinement force μ_b and confinement force length scale γ . A set of these parameters is represented as a vector

$\vartheta = (v_0, \mu, D_\phi, D_n, \mu_b, \gamma)$ below.

Given quantitative experimental data D_a , the MCMC can in general numerically construct the posterior distribution of parameters $p(\vartheta | D_a)$ from a prior distribution $p(\vartheta)$ with Bayes theory. To do this, the likelihood $p(D_a | \vartheta)$ is required but is often difficult to derive. ABC MCMC replaces the likelihood by a distance d_s between the summary statistics of the data and simulation, and approximates the posterior distribution as $p(\vartheta | D_a) \approx p(\vartheta | d_s \leq \varepsilon)$ where ε is a tolerance.

We used the MSDD as the summary statics in the ABC MCMC because the MSDD is likely to be a function of all the parameters in the physical model. Let $m(t_i)$ be the MSDD measured in an embryo at time t_i ($i = 1, \dots, T$) and $m_s(t_i)$ be the MSDD obtained by a numerical simulation of the physical model. We defined the distance

between these MSDD $d_s(m, m_s)$ as:

$$d_s(m, m_s) = \sum_{i=1}^T \frac{\{m(t_i) - m_s(t_i)\}^2}{m(t_i)^2}. \quad (\text{S7.1})$$

Although both $m(t_i)$ and $m_s(t_i)$ are time series data and should have correlations between successive time points, we neglected these temporal correlations and treated these data as independent data points in Eqn S7.1.

The ABC MCMC algorithm proceeds as follows:

A1. Draw the values of parameters ϑ_j ($j = 0$) from the prior distribution $p(\vartheta)$ for initialization.

A2. Propose a set of values of parameters ϑ' from the proposal distribution $g(\vartheta_j \rightarrow \vartheta')$.

A3. Carry out a numerical simulation of the physical model with the parameter set ϑ' and compute $m_s(t_i)$.

A4. If $d_s(m, m_s) \leq \varepsilon$, go to A5, otherwise set $\vartheta_{j+1} = \vartheta_j$ and go to A6.

A5. Set $\vartheta_{j+1} = \vartheta'$ with probability $p_a = \min\left(1, \frac{p(\vartheta')}{p(\vartheta)}\right)$ and $\vartheta_{j+1} = \vartheta_j$ with probability $1 - p_a$.

A6. Set $j = j + 1$ and go to A2.

To define the prior distribution $p(\vartheta)$, we set a uniform distribution for each parameter:

$$p(\chi) = \begin{cases} \frac{1}{\chi^{(\max)} - \chi^{(\min)}}, & \chi^{(\min)} \leq \chi \leq \chi^{(\max)} \\ 0, & \text{otherwise} \end{cases} \quad (\text{S7.2})$$

where $\chi \in \{v_0, \mu, D_\phi, D_n, \mu_b, \gamma\}$. The intervals for uniform distributions were chosen to be biologically plausible and are listed in Table S5. Then, the prior distribution $p(\vartheta)$ was defined as:

$$p(\vartheta) = p(v_0)p(\mu)p(D_\phi)p(D_n)p(\mu_b)p(\gamma). \quad (\text{S7.3})$$

To propose a set of parameter values from ϑ_j , we used

$$\vartheta' = \vartheta_j + \Delta\vartheta, \quad (\text{S7.4})$$

where $\Delta\vartheta = (\Delta\vartheta_{v_0}, \Delta\vartheta_{\mu}, \Delta\vartheta_{D_{\phi}}, \Delta\vartheta_{D_n}, \Delta\vartheta_{\mu_b}, \Delta\vartheta_{\gamma})$ is the vector of which each element is drawn from the normal distribution $N(0, \sigma_{\chi})$, ($\chi \in \{v_0, \mu, D_{\phi}, D_n, \mu_b, \gamma\}$). Note the symmetry $g(\vartheta \rightarrow \vartheta') = g(\vartheta' \rightarrow \vartheta)$ in this setting. The values of σ_{χ} are listed in Table S5.

We set the tolerance as $\varepsilon = 2$. We collected more than 4000 samples and discarded the initial 1000 as transients. To check the convergence of the distribution, we compared 5 independent realizations of ABC MCMC sampling. Similar distributions were observed in all these 5 realizations, one of them is shown in Fig. S8A and B.

We found a few necessary conditions for explaining the MSDD data in the tailbud. There was a clear correlation between the self-propulsion velocity v_0 and the intercellular force coefficient μ (Fig. S8A). These two parameters largely determined the cell velocity \mathbf{v}_i in simulations. To reproduce the experimental MSDD, the cell velocity had to be strictly constrained. The length scale of the nuclear confinement force γ must be small (Fig. S8B), indicating that nuclei should move freely within cells.

Using the fitted model we estimated single-cell velocities and velocity auto-correlation in the tailbud (Fig. S9). It would be difficult to obtain these quantities directly from embryonic images due to the influence of global tissue motion and deformation. A velocity modulus distribution (Fig. S9A) was obtained from the fit to tailbud data of the 17 ss embryo in Fig. 2. In the simulation, the mean of velocity modulus was $\langle |\mathbf{v}| \rangle = 0.58 \pm 0.31 \mu\text{m min}^{-1}$. This is an estimate of the cellular velocity modulus *in vivo*. The values of the average velocity modulus for the other three embryos estimated from simulations were similar to this value (Fig. S9B). We also estimated the timescale of velocity auto-correlation for a single cell in the tailbud from the fitted model (Fig. S9C, D). This timescale represents the persistence time for a cell to keep moving in one direction. The velocity auto-correlation C_a was defined using the velocity vector for cell i in a

simulation \mathbf{v}_i as

$$C_a(\tau) = \frac{1}{N} \sum_{i=1}^N \frac{\mathbf{v}_i(\tau) \cdot \mathbf{v}_i(0)}{|\mathbf{v}_i(\tau)| |\mathbf{v}_i(0)|}, \quad (\text{S7.5})$$

where N is the total number of cells in the physical model.

The auto-correlation decays as a double-exponential curve in simulations (Fig. S9C). We fitted separate exponential functions $c_0 \exp(-t/\tau_a)$ at short and long timescales to the data and obtained their characteristic time τ_a . For the 17 ss embryo in Fig. 2A, $\tau_a \approx 4.3$ min for short timescales and $\tau_a \approx 13.3$ min for long timescales (Fig. S9C). The timescale of the second decay is set by the polarity noise strength D_ϕ in the model. In addition, the values of auto-correlation were quite small (less than 0.2) in this regime. So, we argue that the timescale of the first decay is more relevant for cell movement in the tissue. We obtained similar values of the persistence time for the other three embryos in simulations (Fig. S9D).

S8. Mean-field system

Our previous study (Uriu et al., 2013) demonstrated that when relative movement of oscillators is sufficiently fast, a population of the mobile oscillators behaves as a mean-field system, where each oscillator interacts with all the other oscillators in the system. To examine whether the observed cell mixing in the tailbud is fast enough for the genetic oscillators to be in the mean-field regime, we compare their dynamics with the following mean field system (Kuramoto, 1984):

$$\frac{d\theta_i(t)}{dt} = \omega_i + \frac{\kappa}{N} \sum_{j=1}^N \sin(\theta_j(t) - \theta_i(t)) + \sqrt{2D_\theta} \xi_{\theta_i}, \quad (\text{S8.1})$$

where N is the total number of oscillators in the system. We used the same frequency distribution and the values of parameters in Eqn S8.1 as those in Eqn 5 in the main text. Fig. S14 shows the difference of synchronization dynamics between the mean-field system Eqn S8.1 and the oscillators with reproduced cell mixing. When the value of the coupling strength κ is smaller, their behaviors are closer. As the coupling strength increases, the difference becomes larger. The results shown in Fig. S14 suggest that the observed cell mixing in the tailbud is not fast enough for the cells to behave as a mean-field system.

Supplementary References

- Bhavna, R., Uriu, K., Valentin, G., Tinevez, J. Y. and Oates, A. C.** (2016). Object Segmentation and Ground Truth in 3D Embryonic Imaging. *PLoS One* **11**, e0150853.
- Kuramoto, Y.** (1984). *Chemical oscillations, waves, and turbulence*. Berlin: Springer-Verlag.
- Lawton, A. K., Nandi, A., Stulberg, M. J., Dray, N., Sneddon, M. W., Pontius, W., Emonet, T. and Holley, S. A.** (2013). Regulated tissue fluidity steers zebrafish body elongation. *Development* **140**, 573-582.
- Li, G., Liu, T., Nie, J., Guo, L., Malicki, J., Mara, A., Holley, S. A., Xia, W. and Wong, S. T.** (2007). Detection of blob objects in microscopic zebrafish images based on gradient vector diffusion. *Cytometry. Part A : the journal of the International Society for Analytical Cytology* **71**, 835-845.
- Liu, M. B., Liu, G. R. and Lam, K. Y.** (2003). Constructing smoothing functions in smoothed particle hydrodynamics with applications. *Journal of Computational and Applied Mathematics* **155**, 263-284.
- Marjoram, P., Molitor, J., Plagnol, V. and Tavaré, S.** (2003). Markov chain Monte Carlo without likelihoods. *Proc Natl Acad Sci U S A* **100**, 15324-15328.
- Sbalzarini, I. F. and Koumoutsakos, P.** (2005). Feature point tracking and trajectory analysis for video imaging in cell biology. *Journal of structural biology* **151**, 182-195.
- Uriu, K., Ares, S., Oates, A. C. and Morelli, L. G.** (2013). Dynamics of mobile coupled phase oscillators. *Physical Review E* **87**, 032911.